Graphene/Formamidinium Lead Iodide Quantum Dots for UV-visible Photodetectors

Graphene/Formamidinium Lead Iodide Quantum Dots for UV-Visible Photodetectors

By

Mahdi Hasanzadeh Azar

Master of Applied Science of Engineering

McMaster University, July 2024

A THESIS

SUBMITTED TO THE SCHOOL OF GRADUATE STUDIES IN PARTIAL FULFILLMENT OF THE REQUIREMENTS FOR THE DEGREE OF MASTER'S OF APPLIED SCIENCE

McMaster University

Hamilton, Ontario, Canada

MASTER OF APPLIED SCIENCE (2024) McMaster University

(Department of Engineering Physics) Hamilton, Ontario

TITLE: Graphene/Formamidinium Lead Iodide Quantum Dots for UV-Visible Photodetectors

AUTHOR: Mahdi Hasanzadeh Azar, M.A.Sc. (Sharif University of Technology)

SUPERVISOR: Prof. Adrian Kitai

NUMBER OF PAGES: xvi, 93

Abstract

Formamidinium lead iodide perovskite ($FAPbI_3$) has been introduced as the most promising candidate in solar cells and photodetectors due to its high moisture stability and favorable NIR absorption edge. However, the alpha phase of $FAPbI_3$ with impressive optical properties is stable at above 160 °C.

In this research, by taking advantage of a ligand-assisted reprecipitation method (LARP), the alpha phase of $FAPbI_3$ QDs colloidal solution was prepared at room temperature, confirmed by X-ray diffraction (XRD). Although high-coordinating DMF, as the solvent of precursors, failed to synthesize the QDs, the mixture of ACN/GBL, oleic acid, and octylamine was capable of crystallizing ~7.5 nm $FAPbI_3$ QDs. Based on the photoluminescence and UV-vis tests, the emission peak and absorption edge of QDs were measured at 751 nm and 682 nm, respectively.

To fabricate an efficient QD-based UV-visible (whole spectrum) photodetector, a monolayer graphene ($I_{2D}/I_G>2$) with high crystallinity ($I_D/I_G\sim0$) was transferred to a Si/SiO_2 substrate via the PMMA method. Based on optical microscopy and Raman Spectroscopy results, a remarkable concentration of PMMA contaminations was removed without considerable damage to the graphene crystal structure. After electrode deposition with an interdigitated design, the QDs were deposited on the device with a configuration of Au-Cr/Si/SiO_2/Graphene/Au-Cr via drop casting, spin coating, and centrifugation. Among all methods, QD-based photodetectors prepared by centrifugation method showed the highest responsivity at 72 A/W, 10^4 times higher than that of bare QD photodetector, under blue

LED illumination with light intensity of ~2 μW/cm^2 at V_{SD} of 0.01 V. This photodetector device responded to UV, green, yellow, and red LEDs, however, the best performance was achieved when photodetectors were exposed to the blue LED. In addition, it was revealed that the performance of devices was dependent on the gate voltage. Therefore, graphene/$FAPbI_3$ QD photodetectors can shed light on the next generation of UV-vis photodetectors.

Keywords: 1) Perovskite **2)** Formamidinium lead iodide **3)** Quantum dot **4)** Graphene **5)** Photodetector.

Acknowledgments

I would like to express my gratitude to all who supported me throughout the completion of this research. This dissertation would not have been possible without their invaluable contributions.

Firstly, I extend my appreciation to my supervisor, Prof. Adrian Kitai, for his economic, scientific, and psychological support over the past two years. I am also profoundly grateful to my supervisory committee members, Prof. Chang Qing Xu and Prof. Igor Zhitomirsky.

It is also a great honor for me to thank:

- All staff in Biointerfaces Institute, who allowed me to synthesize and characterize my QDs solution.
- Prof. Chang Qing Xu for allowing me to use his dicing machine, optical power meter, and power supply.
- Prof. Gu Xu and Prof. Ponnambalam Ravi Selvaganapathy for providing the perovskite precursors, solvents, and ligands.
- Prof. Rafael Kleiman for lending his source meter.
- Mrs. Doris V. Stevanovic for training me to use various equipment in CEDT.
- Dr. Ramis Imran Arbi for allowing me to use his source meter.
- Tingwei Zhang, Zhi Min Gao, Zimo Ji, and Bawa Salman for sharing valuable insights and useful discussions.
- And my wife for her great support and encouragement during the last two years.

Table of Contents

List of Figures

List of Tables

List of Acronyms

Quantum dots (QDs)

Photoluminescence quantum yield (PLQY)

Formamidinium lead iodide ($FAPbI_3$)

Ligand-assisted reprecipitation method (LARP)

X-ray diffraction (XRD)

High-resolution transmission electron microscopy (HRTEM)

Quantum confinement effect (QCE)

Hot injection (HI)

Oleic acid (OA)

Octylamine (OAm)

Oleylamine (OM)

1. Chapter 1: Introduction

In this chapter, firstly, the structural, morphological, and optical properties of perovskite nanocrystals are presented. Next, the various methods used to synthesize perovskite quantum dots (QDs) are described. Finally, a broad range of optoelectronic applications fabricated based on perovskite QDs, including light-emitting diodes, solar cells, lasers, and photodetectors, are discussed.

1.1. Perovskite

Perovskites have engaged considerable attention due to their fascinating optical properties. They are divided into two groups: inorganic and organic/inorganic. The chemical formula of perovskites is represented by AMX_3, where A is an inorganic (Cesium (Cs^+)) or organic (formamidinium ($CH_5N_2^+$) or methylammonium ($CH_3NH_3^+$)) cation, M is a metal (lead or tin), and X is an anion (iodine (I), bromine (Br), or chlorine (Cl)). Regarding the crystal structure, A is embedded at the center of eight connected octahedrons, and each octahedron is comprised of an M atom surrounded by six halogen atoms (Fig.1.1(a)) [1]. Perovskites benefit from a high optical absorption coefficient, high photoluminescence quantum yield (PLQY= 90%), defined as the ratio of emitted photons to absorbed photons, and long carrier diffusion length [2–6]. Moreover, since a wide range of elements can be inserted into the perovskite crystal structure, bandgap energy is widely tuned from UV to NIR (Fig.1.1(b, c)) [7,8].

Due to these impressive properties, perovskites have manifested great potential to be used in optoelectronic devices, including solar cells, light-emitting diodes, and solar cells. Lead-based perovskite solar cells were first fabricated in 2009 by Miyasaka et al.[9] with an

initial efficiency of 3.8%. By taking advantage of many modifications, the efficiency of perovskite-based solar cells approached 25% in 2023, showing the great capability of perovskites in enhancing the efficiency of solar cells [10]. Apart from their outstanding performance in solar cell efficiency improvement, they showed prominent potential in boosting the performance of LEDs and lasers [11].

Although perovskites benefit from various fascinating optical properties, they suffer from severe instability in harsh conditions. The tolerance factor determines the phase stability of perovskites using the radii of the organic, inorganic, and anionic parts (Fig.1.2(a)). When this factor is between 0.9 and 1, the perovskite structure is stable in a cubic form. When this factor is between 0.7 and 0.9, the octahedron is rotated, resulting in a distorted perovskite structure. However, when the tolerance factor is less than 0.7 or greater than 1, a non-perovskite structure is expected [12].

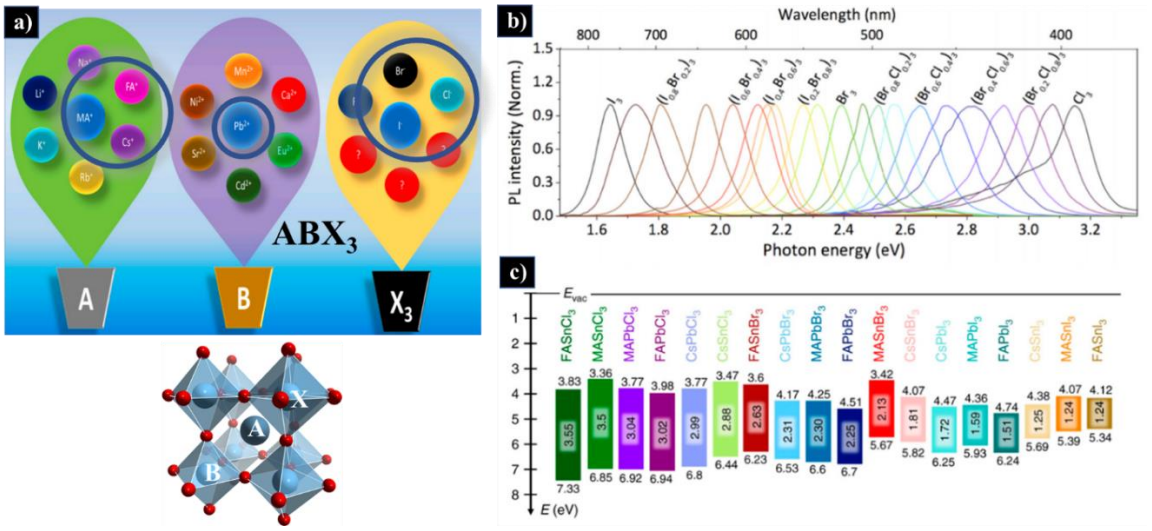

Figure 1.1. (a) Crystal structure of perovskite including various cations, metals, and anions. (b) PL spectra and (c) bandgap energies of various perovskites with different compositions [7,8].

1.2. Formamidinium Lead Iodide ($FAPbI_3$)

Among all organic-inorganic perovskites, $FAPbI_3$ is the most promising and efficient candidate to be used in optoelectronic applications. $FAPbI_3$ has a smaller bandgap energy (1.48-1.43 eV) than $MAPbI_3$, making it more favorable to be used as an active layer in solar cells. Additionally, many studies have shown that methylammonium iodide is thermodynamically unstable against light, heat, and moisture, either easily decomposes to initial precursors or transforms into a non-perovskite phase. In contrast, $FAPbI_3$ is more (less) stable than $MAPbI_3$ ($CsPbI_3$) in harsh conditions.

$FAPbI_3$ has two different crystal structures. As shown in Fig.1.2(b, c), the black or perovskite phase, named alpha phase (α-$FAPbI_3$), has a cubic structure with direct bandgap energy of 1.47 eV [12,13]. However, the yellow or non-perovskite phase, named delta (δ-$FAPbI_3$), has a hexagonal structure with a high bandgap energy of 2.43 eV and poor optical properties. The phase transformation temperature from delta to alpha is about 160 °C. In other words, while δ-$FAPbI_3$ is phase stable at room temperature, α-$FAPbI_3$ is stable at elevated temperatures. Therefore, to crystallize α-$FAPbI_3$, the spin-coated solution of perovskite precursors is heated up to above 160 °C, followed by cooling to room temperature. However, α-$FAPbI_3$ tends to revert to δ-$FAPbI_3$ by the passage of time. Moreover, harsh environmental conditions accelerate the phase transformation from alpha to delta phase at room temperature. For instance, half of α-$FAPbI_3$ was converted to δ-$FAPbI_3$ after exposure to an environment with a relative humidity of 85% for 15 h. Moreover, less than two days was sufficient to observe that above 90% of perovskite experienced alpha-to-delta transformation due to the water vapor [14].

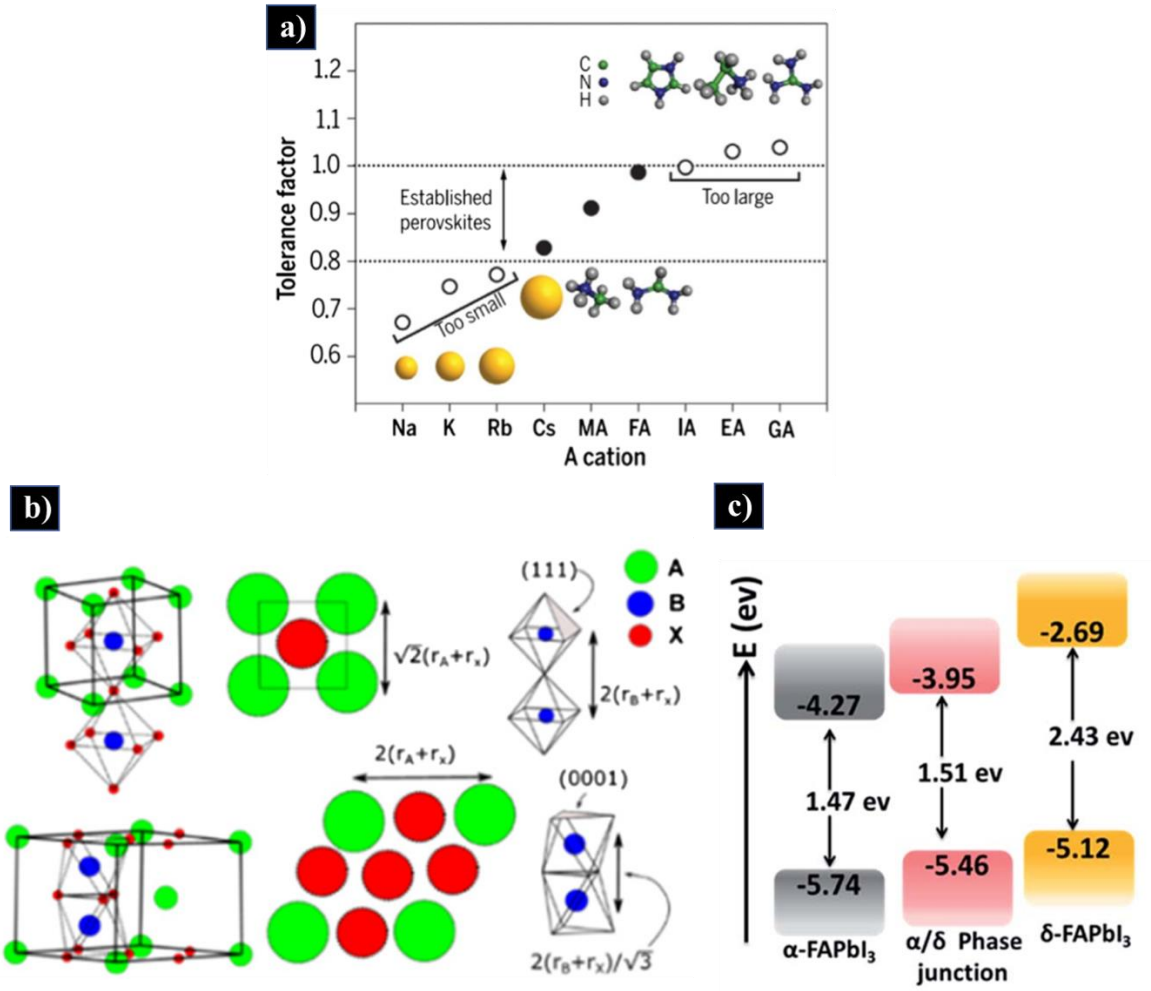

Figure 1.2. (a) The effect of type of cation on the tolerance factor of different perovskites. (b) Crystal structure and lattice parameters of the pseudocubic α- $FAPbI_3$ and δ-$FAPbI_3$ [12]. (c) Bandgap energies of α- $FAPbI_3$ and δ-$FAPbI_3$ [13].

To increase the phase stability of $FAPbI_3$, various methods have been employed. One of the effective ways is increasing the proportion of FAI/PbI_2 during the preparation of the solution of perovskites [13]. Another method is compositional engineering by adding inorganic or organic-inorganic elements. For instance, by adding methylammonium iodide, the tolerance factor can approach the ideal value [15]. However, these are not efficient ways

when perovskites are required to function in humid environments or at high temperatures. Recently, one of the unique methods that has received remarkable attention to stabilize the alpha phase in ambient conditions is the synthesis of $FAPbI_3$ nanocrystals. Considering copper sulfide (CuS), when the size of CuS nanoparticles was reduced to a few nm, the phase transition temperature was significantly reduced, and the favorable phase with excellent optical properties was stabilized at room temperature [16]. In terms of $FAPbI_3$, the critical phase transition temperature from delta to alpha phase could decrease to room temperature, enabling the stabilization of the alpha phase at ambient temperature [17]. Another advantage of replacing bulk and film samples with QDs is the improvement of stability against environmental moisture [17]. Additionally, due to the quantum confinement effect, not only excitons are strongly confined and the probability of radiative recombination increases, but also the bandgap can be tuned and engineered by altering the size of QDs.

1.3. Different Morphologies of Perovskite Nanocrystals

The golden age of nanomaterials began with the discovery of carbon nanotubes and graphene as one-dimensional (1D) and two-dimensional (2D) materials [18]. Although monolayer graphene is a zero-bandgap semimetal, reducing the lateral size of graphene to a few nm led to bandgap opening with a broad spectrum of emission wavelengths [19]. In addition to graphene, extensive studies were conducted on boron nitride [20]. Although boron nitride is a wide bandgap semiconductor, BN nanocrystals were capable of emitting bluish, greenish, and reddish emissions based on their edge and surface functional groups [21]. Regarding transition metal dichalcogenides (TMDs), a transition from multilayer to

monolayer MoS_2 induced indirect to direct bandgap change [22].

When the size of a semiconductor is smaller than the exciton Bohr radii, a strong confinement regime effect is observed. For instance, the exciton Bohr radii of $CsPbCl_3$, $CsPbBr_3$, $CsPbI_3$, and $FAPbBr_3$ perovskites were reported to be 5 nm, 7 nm, 12 nm, and 7.6 nm, respectively [15]. Regarding $FAPbI_3$, the exciton Bohr radius was calculated to be 11 nm. This means that NCs smaller than 22 nm benefit from QCE. In this case, excitons are strongly confined, resulting in a transition from continuous to discrete energy states. This significantly increases the probability of radiative recombination, improving the PLQY. In addition, NCs show size-dependent optical properties. In more detail, by decreasing the size of NCs, the absorption edge and emission peak of NCs are shifted to lower wavelengths. These characteristics open up a path for tuning the luminescence of semiconductors in LEDs.

The stability of perovskites is also influenced by size reduction from bulk to nanocrystals. For instance, perovskite quantum wells have shown the highest stability among all morphologies, due to the long passivating ammonium ligands as well as promoted phase stability, however, they failed to show impressive PLQY [22]. For instance, $FAPbI_3$ nanosheets showed a higher contact angle compared to the bulk perovskite sample, demonstrating their higher stability in humid environments [23]. Moreover, QDs benefit from strong QCE in three dimensions with high PLQY and higher stability than bulk perovskite [17].

1.4. Synthesis Methods of Two-Dimensional Perovskites

Perovskite nanosheets have great potential to be used in optoelectronic devices due to their

low defects, high surface quality, single-crystallinity, and large surface area [24]. One of the most commonly used methods for synthesizing 2D structures is the vapor phase deposition (VPD) method (Fig.1.3(a)). In this process, lead iodide is grown on a mica substrate from a vapor phase. The smooth surface of mica and the high lattice mismatch between lead iodide and mica increases the tendency for horizontal growth, resulting in the perovskite formation with a sheet-like shape. By inserting methylammonium halide into the PbI_2 layer, perovskite nanosheets are formed. Although the concentration of contamination is negligible in this process, the crystallinity of the final product is not high due to the partial accommodation of methylammonium halide in the lead iodide crystal structure [25]. Solution-based processes have also been used to synthesize perovskite nanosheets. For instance, Leo et al. [26] deposited lead iodide aqueous solution on a silicon oxide substrate using a hot casting method to form lead iodide nanosheets, followed by insertion of methylammonium halide to form perovskites. Due to the inherent layered structure of lead iodide, crystals tend to aggregate into platelets in the aqueous solution during the process.

Kovalenko et al. [27] introduced a mechanochemical method to prepare perovskites with 2D morphology. They milled a solution of formamidinium lead bromide, octylammonium bromide, and oleic acid in methyl isothiocyanate solvent using zirconia balls at a speed of 500 rpm for 30 min and 3 h. HRTEM images in (Fig.1.3(b)) show the formed mixture of nanosheets and QDs. PL spectra in (Fig.1.3(c)) indicate that by increasing the milling time, the blue emission peak is intensified while the green emission peak is weakened, due to the thickness reduction of nanosheets.

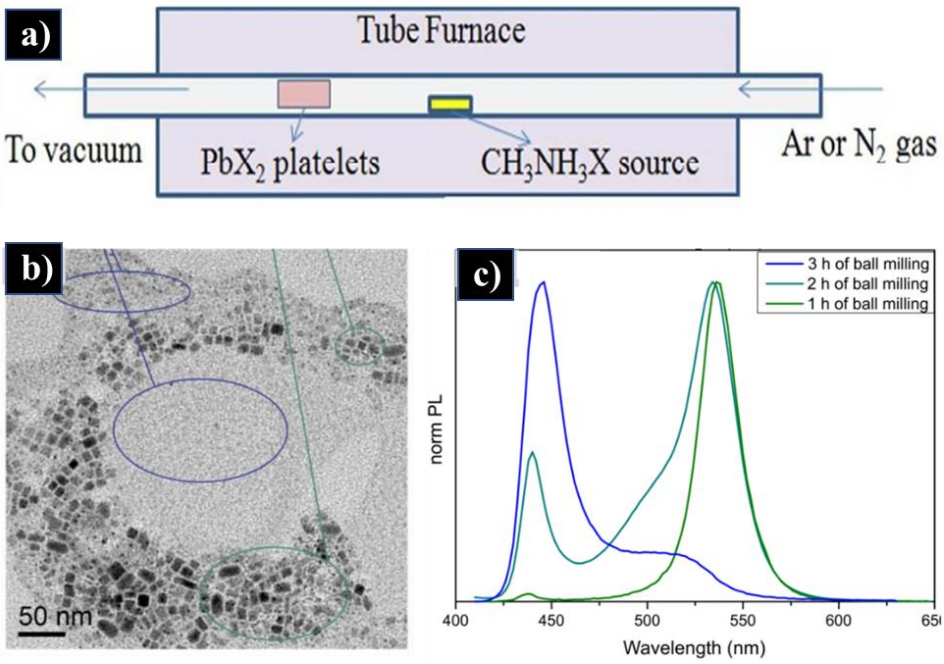

Figure 1.3. (a) Vapor phase deposition for the synthesis of perovskite nanosheets [25]. (b) TEM of perovskite nanosheets prepared by ball milling. (c) The effect of ball milling time on the PL spectra of nanocrystals [27].

One of the main methods for the synthesis of $FAPbI_3$ nanosheets is using long ammonium ligands such as butylammonium [28]. These ligands with ammonium functional groups can separate the layers of lead iodide apart. Then, nanosheets are prepared by injecting pre-dissolved precursors into a non-polar solvent. The TEM image in (Fig.1.4(a)) shows the synthesized 2D square-shaped nanostructures. Based on the XRD of $FAPbI_3$ perovskite nanoplates, the corresponding peaks are different from that of bulk $FAPbI_3$, confirming the change of chemical formula of perovskite nanoplates to $A_2FA_{(n-1)}Pb_nI_{3n+1}$, where A, FA, and n represent the long ligand, formamidinium, and the number of layers, respectively. Moreover, by reducing the number of layers from 2 to 1, the color changes from orange to yellow (Fig.1.4(b)). This was confirmed by another study as it was revealed that by

increasing the amount of ligand, the number of layers of nanosheets decreased and the PL wavelength was shifted to lower wavelengths (Fig.1.4(c)). Also, by increasing the number of layers to 5, the PLQY increased and reached the peak of about 11%, however, beyond n=5, the PLQY gradually decreased to values less than 5% due to the lack of QCE (Fig.1.4(d)) [29].

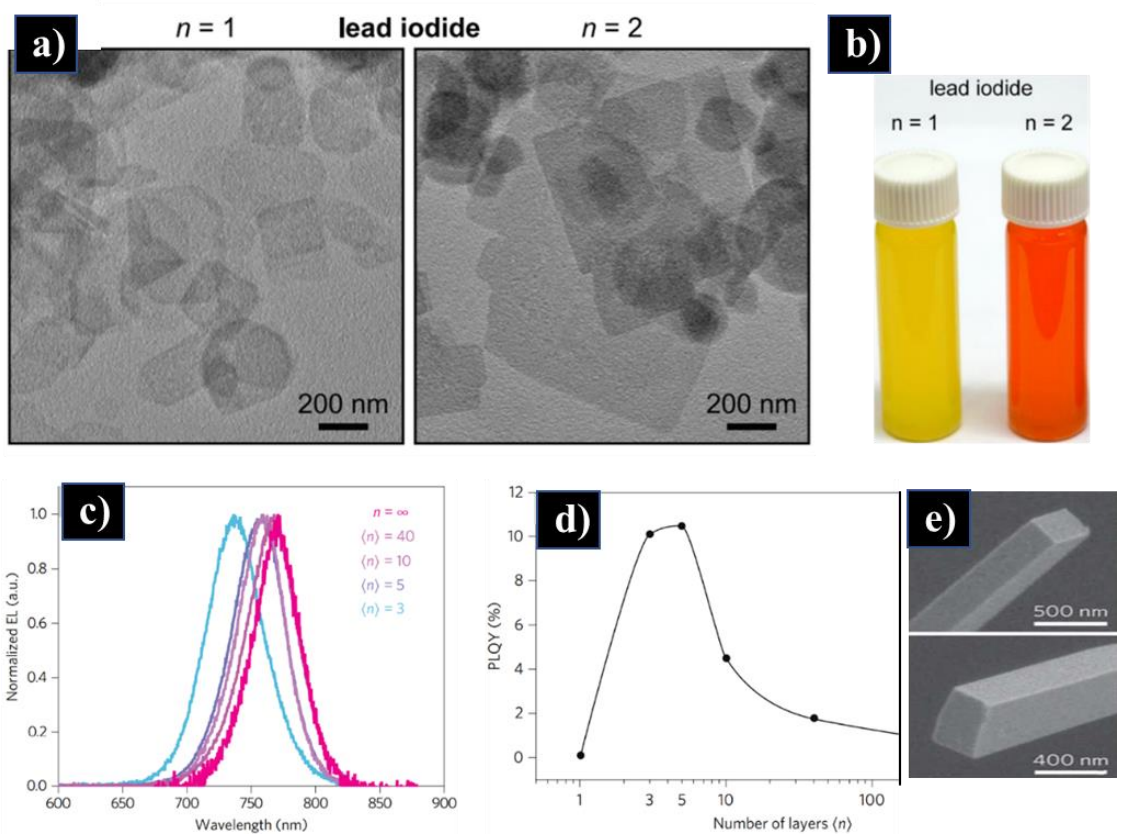

Figure 1.4. (a) TEM and (b) the photographs of $FAPbI_3$ nanosheets with different thicknesses [28]. The effect of the number of perovskite nanosheet layers on the (c) PL spectrum and (d) PLQY [29]. (e) SEM of $MAPbI_3$ nanowires [30].

1.5. Synthesis Methods of Perovskite Nanowires

Lead halide perovskite nanowires have been utilized for various optoelectronic devices

[31]. In recent decades, significant efforts have been made to synthesize nanowires via the VPD method. In this approach, thin layers of noble metals are used as catalysts to accelerate the crystal growth of perovskite in one dimension. In contrast to the above method, the solution process has the advantage of lower cost and simplicity [32]. In one of the studies, a solution process method with a surfactant for controlling the growth of all-inorganic halide perovskite $CsPbX_3$ nanowires was reported. For instance, by reacting cesium oleate with lead halide in the presence of oleic acid at temperatures between 150- 250 °C, nanowires were formed. Oleylamine was also used to induce preferential 1D growth to obtain nanostructured perovskites [33]. However, the production efficiency of these nanowires is not high compared to nanosheets and QDs.

Zhu et al. [30] proposed a surfactant-free method to synthesize nanowires. In this process, a thin solid layer of lead acetate was first deposited on a glass substrate using an aqueous solution of $PbAc_2 \cdot 3H_2O$. Then, the $PbAc_2$ film was immersed in a solution containing methylammonium iodide and isopropanol for more than 20 h. Fig.1.4(e) depicts the crystallized $MAPbI_3$ perovskite nanowires with a length and width of 20 μm and 100 nm, respectively.

1.6. Synthesis Methods of Perovskite QDs

1.6.1. Microemulsion

Fig.1.5(a) illustrates how perovskite QDs are formed via microemulsion method [34]. In this method, two immiscible polar and non-polar solvents, dimethylformamide (DMF) and hexane, are mixed using oleic acid. This is achieved by using specific weight percentages of each component, which can be determined by a ternary phase diagram. Then, by adding

butanol or acetone as a separator, perovskite QDs are formed. Via two-step centrifugation at 6000 rpm for 5 min, large particles are removed, and smaller particles are suspended in a non-polar solvent. Furthermore, butanol serves two roles as a separator and precipitator. In terms of the former, when two polar and nonpolar solvents are dissolved, butanol reduces the surface tension and consequently facilitates precipitation. Regarding the latter, butanol removes residual surfactants, polar solvents, and excess materials to prepare a relatively pure colloidal solution of spherical QDs (Fig.1.5(b)). These QDs had absorption and emission wavelengths of perovskite 512 nm and 521 nm, respectively, with a PLQY of 90%.

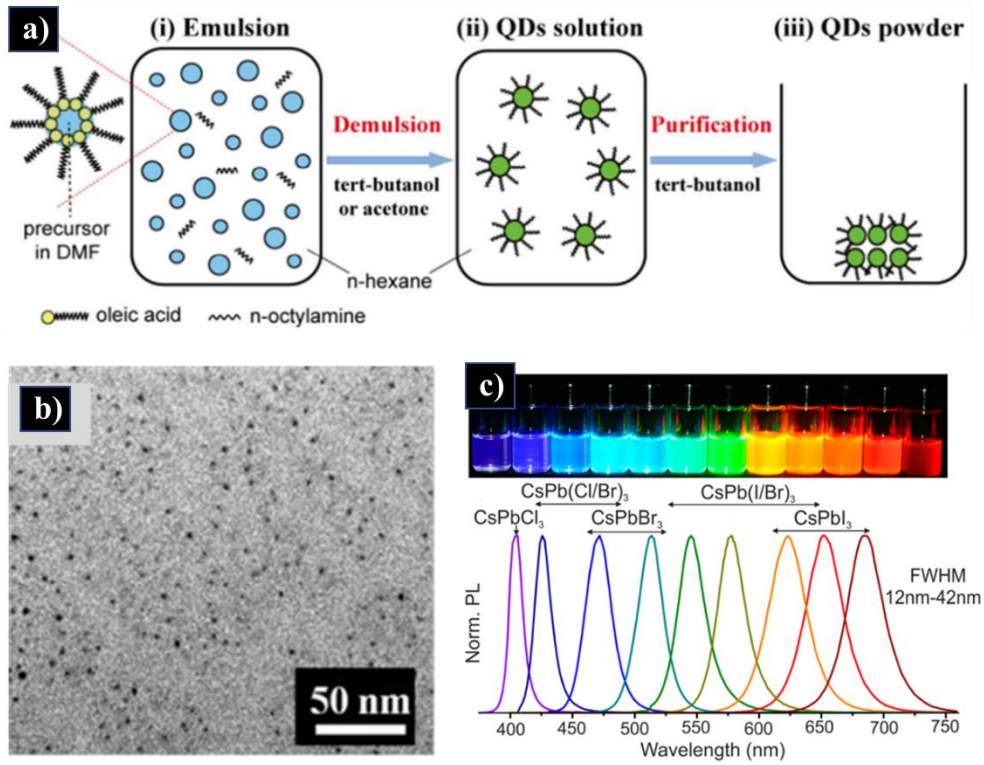

Figure 1.5. (a) Synthesis of perovskite QDs by microemulsion process. (b) TEM of perovskite QDs [34]. (c) Emission spectra and the photographs of colloidal solutions of QDs prepared by hot injection under UV illumination [35].

1.6.2. Hot Injection

One of the most effective methods for the synthesis of QDs is hot injection (HI). In this method, octadecene with high boiling temperature is used as a medium to dissolve all perovskite precursors, including lead bromide, oleic acid (OA), and oleylamine (OM). Then, perovskite QDs were obtained by injecting cesium oleate into the solution of perovskite precursors. As depicted in (Fig.1.5(c)), by taking advantage of composition engineering, various QDs (5-15 nm) with different emission spectra ranging from 410 to 700 nm were obtained [35]. The thermal driving force is the unique characteristic of HI, assisting the QDs to be perfectly crystallized. In addition, tuning the temperature is capable of altering not only the optical properties but also the morphology of nanocrystals.

In terms of $FAPbI_3$ QDs, Kovalenko et al. [35] were able to use HI to synthesize lead iodide perovskite nanocrystals. After pouring PbI_2, OA, OM, and octadecene into flux, the system was heated up to 120 °C. Once PbI_2 was completely dissolved, the temperature was lowered to 80 °C, and formamidinium oleate was added, followed by the centrifugation step at the speed of 13000 rpm and dispersion in a non-polar solvent. Fig.1.6(a) shows the cubic-shaped QDs with an average size of 15 nm. XRD also confirms that the alpha phase with desirable emission properties was formed without any delta phase (Fig.1.6(b)).

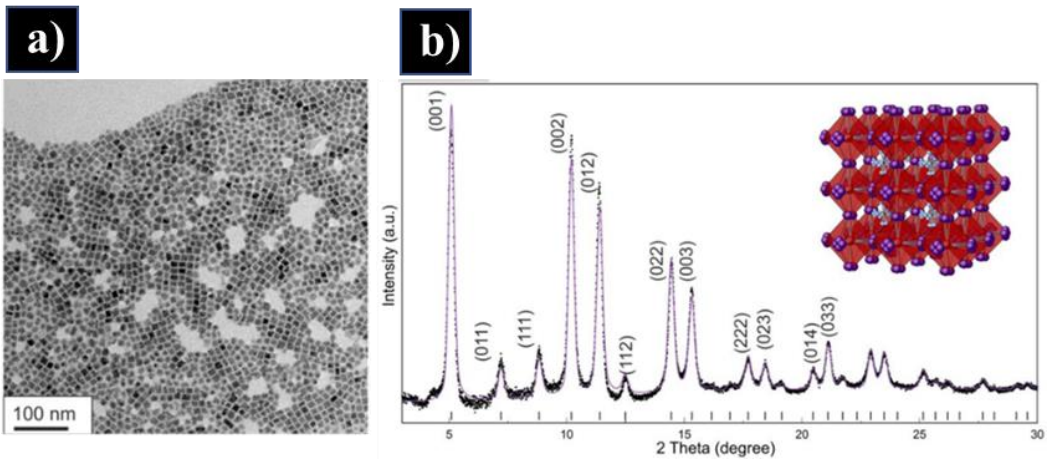

Figure 1.6. (a) TEM image and (b) XRD of $FAPbI_3$ QDs prepared by HI [35].

1.6.3. Core/Shell Method

Another effective method to synthesize perovskite QDs is employing silane ligands to form a core/shell structure. This process is slightly different from other silane-based methods. For instance, a mesoporous silica template is a ligand-free process in which the solution of precursors is injected into the prefabricated mesoporous silica, followed by heat treatment, inducing perovskite crystallization. However, this process is costly and needs many processing steps. Stirring the mixture of tetramethyl orthosilicate (TMOS) and the QDs in the air also makes the process uncontrollable. In the core-shell method, $MAPbBr_3$ QDs with an orthorhombic structure have been synthesized by replacing octylamine with (3-Aminopropyl)trimethoxysilane (APTES) [36,37]. In this case, amine groups not only control the size of QDs but also stabilize them by creating a shell around them. To achieve this, the solution of QDs is stirred in the air for 4 h, which induces the hydrolyzation and condensation of the alkoxysilane groups of trimethoxysilane to form a larger QD-SiO_2 core-shell structure. Fig.1.7(a) schematically illustrates the process of the silica shell

formation around the QDs. This process starts with the attachment of ligands to the quantum dot surface, followed by the formation of Si-OH, and then, Si-O-Si bonds. Although bromine-based perovskite QDs were successfully formed, it was found ineffective for the synthesis of $MAPbI_3$ QDs. In contrast, not only $CsPbBr_3$ but also $CsPbI_3$ QDs were synthesized using triethoxysilane ligands in another study. To achieve this, lead bromide and lead iodide with appropriate ligands were dissolved in octadecene solvent, followed by injection of cesium oleate into the precursors. In this study, to accomplish the hydrolysis process, the solution of QDs was heated up to 40 °C. TEM demonstrated that cesium lead bromide and lead iodide QDs could be embedded in a silica matrix, and Fourier-transform infrared (FTIR) spectroscopy confirmed the formation of Si-O-Si bonds.

1.6.4. Ligand-assisted reprecipitation method (LARP)

The ligand-assisted reprecipitation method is a facile, cost-effective, and room-temperature approach, being recently used for the synthesis of perovskite QDs. Similar to HI, ligands with amine and carboxyl groups are used to not only control the size of QDs but also stabilize them in the non-polar solvent. Without ligands, micron-sized particles are obtained with extremely low PLQY. Initially, lead bromide, methylammonium bromide, OA, and OAm are dissolved in a suitable solvent like DMF (Fig.1.7(b)) [38]. By adding a specific amount of solution of precursors to a stirring non-polar solvent like toluene, the nucleation and growth of QDs are performed. Subsequently, a brownish colloidal solution is formed, indicating the crystallization of QDs. To prepare the colloidal solution of QDs, the whole synthesis batch is centrifuged twice at a speed of 7000 rpm to remove larger particles and supernatant, and disperse the QDs in n-hexane. X-ray energy dispersive spectroscopy

revealed that while the ratio of bromine to lead for bulk perovskite is 3, this reached 3.5 for high surface-to-volume ratio QDs (Fig.1.7(c, d)). This indicates that the surface atoms of QDs deviate from stoichiometry law, being enriched with bromine.

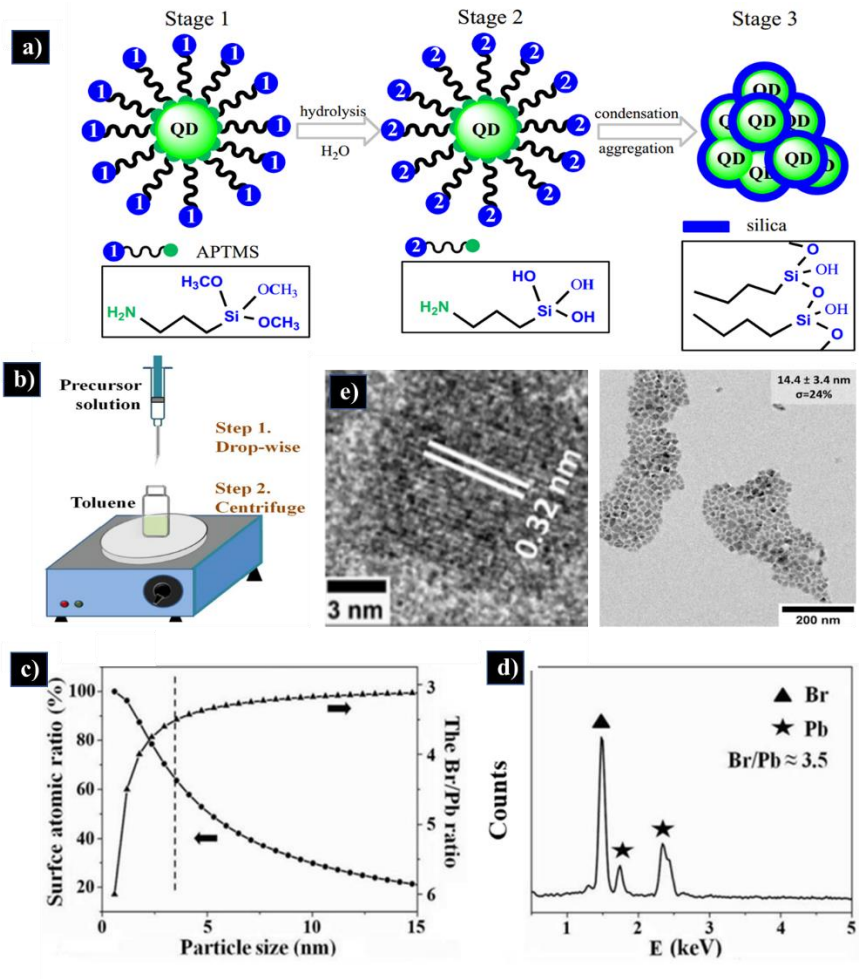

Figure 1.7. (a) The process of hydrolyzation and condensation of QDs in the core-shell method [36]. (b) Schematic diagram showing the LARP process. (c) HRTEM of $FAPbI_3$ QDs prepared by LARP process [39]. (d) The effect of the Br/Pb ratio on the particle size as well as (e) EDS result [38].

$FAPbI_3$ QDs were also synthesized by using the LARP method. Luvchuk et al. [39] used

DMF as the medium for dissolving lead iodide and organic ligands. Then, 50 µl of this solution was injected into the anti-solvent, resulting in the formation of $FAPbI_3$ QDs with an average size of 17.4 nm (Fig.1.7(e)). In this study, they replaced chloroform with toluene since only the former was successful in crystallizing the cubic phase, confirmed by measuring the interplanar spacing of 3.2 nm, assigned to the (002) plane of the alpha phase. In addition, instead of centrifugation at high speed, a combination of toluene and acetonitrile was used to settle the QDs on the bottom of a centrifuge tube. By taking advantage of this ligand purification step and further dispersion in toluene, the colloidal solution of QDs with a PLQY of 55% remained stable for at least one week in a glove box under nitrogen.

In the LARP and HI processes, there are several parameters, playing important roles in determining the final properties of QDs, which are listed as follows:

- **Concentration of Precursors**

Composition engineering is also an effective way to tune the size of QDs. When the amount of lead bromide remains constant in the synthesis of QDs, reducing the molar ratio of ammonium bromide to lead bromide leads to an increase in bromine ions on the surface of QDs [40]. As a result, a greater surface area is needed to accommodate these ions on the surface, leading to a decrease in the size reduction. Therefore, the size of QDs can be easily controlled by the difference in the molar ratios of methylammonium bromide to lead bromide.

- **Solvent of Precursors**

One of the most important issues is the interaction of various polar solvents such as DMF,

dimethyl sulfoxide (DMSO), tetrahydrofuran, gamma-butyrolactone (GBL), and acetonitrile (ACN) with perovskite precursors [41]. Fig.1.8(a) shows that PbI_2 has two characteristic absorption peaks at 325 and 370 nm. In solvents like ACN and GBL, the spectrum remained almost unchanged, indicating that the internal structure of PbI_2 is preserved. However, the peaks are slightly shifted in tetrahydrofuran while one and two peaks disappear in DMF and DMSO, respectively. Nuclear magnetic resonance (NMR) test also confirmed that the position of the PbI_2 peak in ACN solvent did not change, while this peak was significantly shifted in DMF and DMSO (Fig.1.8(b)). This demonstrates that the latter solvents are capable of forming different intermediate phases of PbI_2. The substitution of iodine atoms with oxygen in DMF forms Pb-O bonds, giving rise to intense coordination of the perovskite precursors by DMF and DMSO.

Therefore, the solvent-perovskite precursor interaction can be either coordinating or non-coordinating. When 1 ml of the precursor's solution in DMSO was poured into 10 ml of toluene, no perovskite phase was formed. Although white bulk precipitants were seen in the case of DMF, attributed to $CH_3NH_3PbI_3.H_2O$, deposits in tetrahydrofuran appeared yellow and orange. Only ACN and GBL were the solvents, capable of synthesizing the perovskite phase of methylammonium lead iodide QDs (Fig.1.8(c)). The main reason for non-perovskite phase formation in high-coordinating solvents is that the solvent might not be easily washed with the anti-solvent, forming abundant iodide vacancies on the surface of QDs, which contributes to ionic structure disintegration. However, ACN is a non-coordinating solvent, synthesizing a stable colloidal solution of $MAPbI_3$ QDs for 3 months (Fig.1.8(d)).

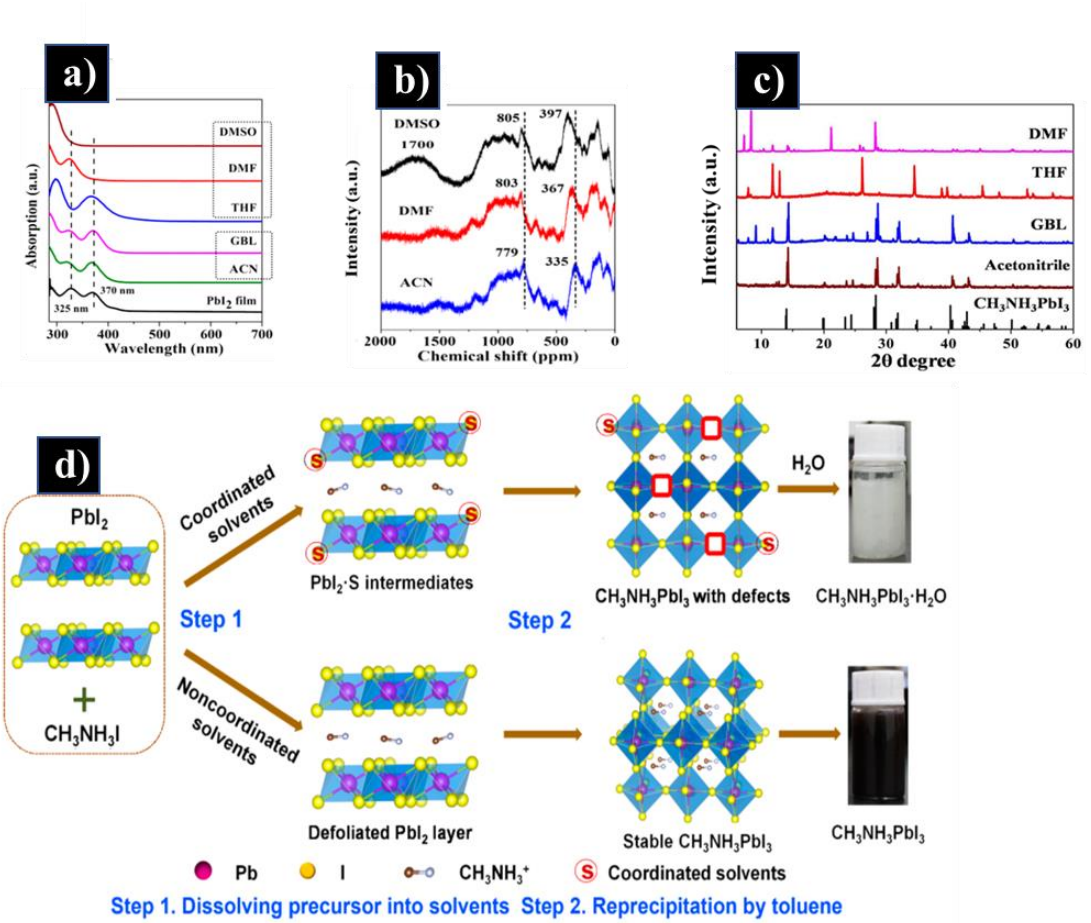

Figure 1.8. The effect of various precursors' solvents on (a) UV-vis and (b) NMR of lead iodide as well as (c) XRD of perovskite QDs. (d) The mechanism of crystallization of QDs prepared by LARP from various solvents [41].

- **Type and Length of Ligands**

In one of the studies, the effect of alkyl chain length was investigated. While MA cations are located in the center of the eight connected PbX_6, alkyl ammonium cations with longer chains are entangled around the octahedral sites. These ammonium ions act as surface ligands for QDs, limiting the growth of $MAPbBr_3$ QDs in three dimensions. To assess the effect of ligand length on the stability of QDs, long-chain octadecylammonium bromide

and short-chain OAm were used [37]. In addition, to find the optimized values, different molar ratios of octadecylammonium bromide to methylammonium bromide ($CH_3(CH_2)_{17}NH_3Br/CH_3NH_3Br$) (0.5/0.5, 0.6/0.4, and 0.3/0.7) were prepared [42]. To simplify the representation of these substances, the abbreviations PODA1, PODA2, and PODA3 were used, where P, ODA, and 1,2, and 3 stand for perovskite, octadecylammonium, and molar ratio, respectively. In all samples, by the injection of the solution of precursors into toluene, an orange solution of $MAPbI_3$ QDs was successfully formed. However, on one hand, both emission wavelength and bandwidth decreased from PODA1 to PODA3, and on the other hand, the 0.6/0.4 molar ratio showed the highest PL intensity. Comparing OAm and ODA, the former showed a more symmetrical and narrower bandwidth emission. Moreover, not only the fluorescence but also the composition uniformity and stability of POAm2 were remarkably higher than that of PODA2. As can be seen in Fig.1.9(a, b), while the appearance of both was the same before exposure to UV light, POAm2 had a more significant emission intensity than that of PODA2. In contrast, some papers indicated that using long-chain alkylamines such as dodecylamine, hexadecylamine, and hexylamine ensured the production of high-quality QDs through controlled crystallization processes. Additionally, different alkyl acids such as butyric acid and octanoic acid were found suitable for enhancing the stability of QDs.

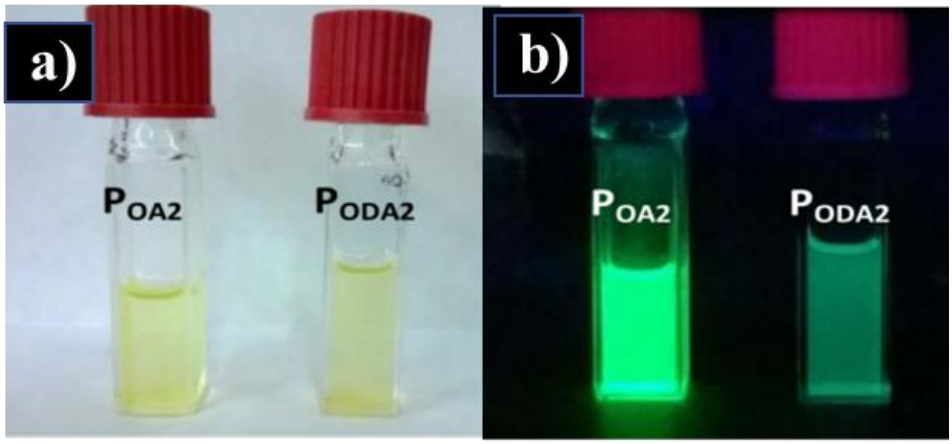

Figure 1.9. The photographs of perovskite QDs with different passivating ammonium ligands (a) without and (b) under UV illumination [42].

In another study, perovskite QDs, synthesized via HI, lost their emission after approximately 15 days. However, after adding 20 to 120 μL of tri-octyl phosphine (TOP), the emission of QDs was reborned and increased to 8.54% and 110%, respectively (Fig.1.10(a)) [43]. In addition, the lifetime results of photoluminescence also showed a significant increase in the stability of QDs with the addition of TOP. The long lifetime is due to the elimination of surface defects and complete surface coverage. Moreover, luminescence intensity in ethanol showed that the initial QDs in 400 μL lost their luminescence, while they remained stable using TOP under the same conditions. The type of phosphine is also important in terms of stability. For example, tri-butyl phosphine and tri-phenyl phosphine failed to provide as high stability as tri-octyl phosphine.

In another study, ligands with high melting points, such as stearic acid and octadecylamine were used to synthesize perovskite-based lead bromide in a stable environment [44]. The synthesized $FAPbX_3$ QDs with long ligands not only showed high PLQY of 88% but also

higher PL stability than that of QDs passivated with short ligands (Fig.1.10(b)).

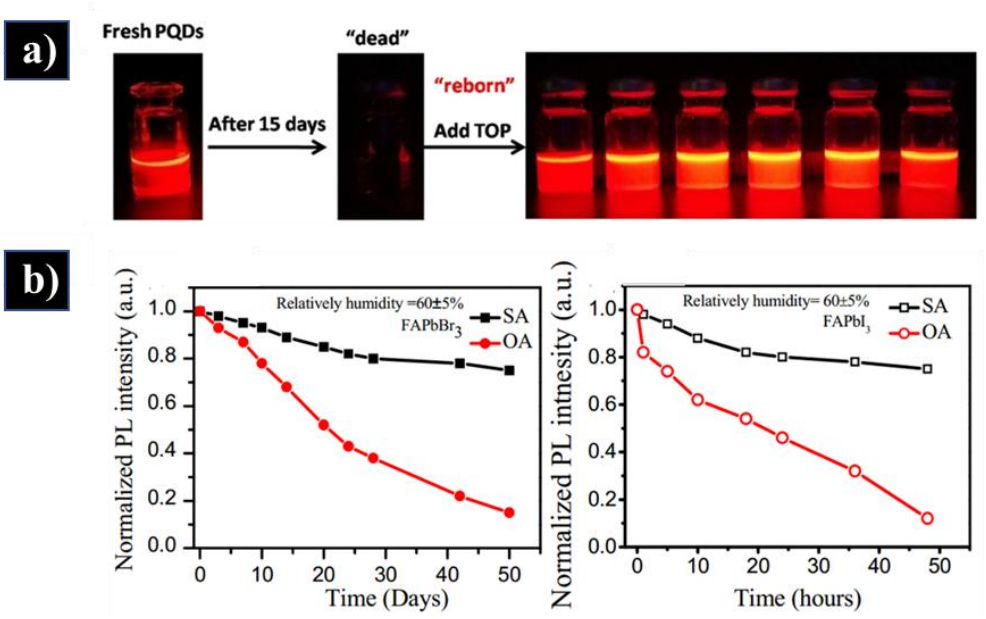

Figure 1.10. (a) Effect of TOP ligands on the luminescence of CsPbI3 QDs [43]. (b) Effect of long ligands replacement with short ligands on the luminescence of $FAPbI_3$ and $FAPbBr_3$ QDs [44].

1.7. Deposition Methods of Perovskite QDs

To prepare a film of QDs, various deposition methods have been used. One of the methods is drop casting. In this process, a specific amount of colloidal solution of QDs is dropped on the surface of the substrate, followed by solvent evaporation under a fume hood. This process is repeated multiple times to prepare a thick film of QDs. However, due to the presence of oleate and ammonium ligands on the surface of QDs, the thick film is not close-packed and uniform, hindering the use of QDs in optoelectronic applications. Spin coating is a commonly used method for the deposition of QDs [45]. By adjusting the speed, concentration of the solution of QDs, and time, the required thickness for the layer can be controlled. In this method, a specific amount of QDs is spin-coated on the surface of the

substrate at different speeds of 1000-2000 rpm. However, QDs are highly passivated with organic ligands, preventing the preparation of a thick film of QDs. Therefore, to reach a thick film of QDs, each deposited layer is washed with a specific solvent, such as pentanol, a pair of ACN and toluene, ethyl acetate, chloroform, methyl acetate, and ethyl acetate, enabling thickening of the QDs film [46]. Another way of increasing the thickness of the QDs layer is ligand exchange, reported mainly in lead sulfide (PbS) QDs. In this method, by designing a new system, long ligands of QDs, dispersed in nonpolar solvents, were replaced with short ligands, dispersed in polar solvents. Initially, OA-passivated PbS QDs in acetone/toluene are mixed with a mixture of mercaptopropionic acid ligand and DMF, followed by the formation of immiscible layers of polar and nonpolar solvents. At this point, the colloidal QDs moved from the nonpolar solvent toward the polar solvent. UV-vis and TEM results revealed the size remained unchanged and OAs were completely removed. The last process is centrifugation. To achieve this, a substrate was placed in a centrifuge tube, followed by the centrifuging process at a specific speed for a specific duration of time, determining the final thickness of the QDs layer [47]. Then, the substrate was dried at room temperature. However, it is evident that the repeatability of this method is not high, and the thickness obtained each time differs from the previous time.

1.8. Applications of Perovskite QDs

1.8.1. Light Emitting Diodes (LEDs)

Organic-inorganic perovskite materials have been introduced as one of the most fascinating materials for light-emitting diodes (LEDs) due to their ease of fabrication, low cost, high PLQY, and narrow emission peak [48]. Also, perovskites benefit from tunable bandgap

energy, covering a wide range of visible spectrum. Moreover, reducing the size of QDs to less than the Bohr radius confines the excitons inside the QDs, increasing the probability of radiative recombination. Kovalenko et al. [49] synthesized $FAPbI_3$ QDs using the HI method and fabricated an LED device (Fig.1.11(a)). Initially, a PEDOT:PSS layer with a thickness of 35 nm was deposited as a hole transport layer on top of an indium oxide substrate using spin-coating. Then, a 30 nm layer of QDs was deposited on the PEDOT:PSS layer as the emissive layer. In terms of the electron transport layer, TPBI was used. Finally, 1 nm and 100 nm of lithium fluoride and aluminum were deposited on the substrate. Fig.1.11(b, c) indicates that the onset voltage of the devices is greater than 4 volts, with a luminance of 54.1 $W \cdot sr^{-1} \cdot m^{-2}$ and external quantum efficiency (EQE) of 3.2% at a current density of 67.0 mA/cm^2. This value is not comparable due to the high concentration of ligands on the surface of QDs. One of the remedies to enhance the performance of the LED device is ligand purification at room temperature. However, this approach requires accurate optimization. For instance, if the washing process is performed excessively, it results in significant surface defects on the surface of QDs, leading to non-radiative recombination.

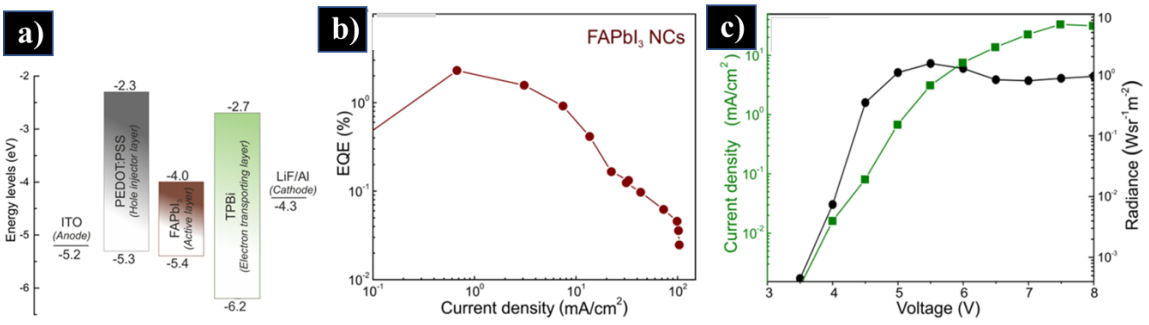

Figure 1.11. Schematic diagram showing the configuration of an LED fabricated based on $FAPbI_3$ QDs. (b) EQE and (c) current density of working LED [49].

1.8.2. Solar Cells

Perovskite QDs have shown great potential to be used in solar cells since they manifested higher stability and efficiency than bulk samples, due to multiple exciton generation and greater Shockley–Queisser limit [50]. There are two ways to fabricate QD solar cells.

Firstly, ligand purification of QDs is an effective way to prepare a thin film of QDs about 300 nm. In one of the studies, $FAPbI_3$ QDs were synthesized using the HI method, followed by employing a three-step ligand purification process [51]. Fig.1.12(a) shows that the spiro-OMeTAD and tin oxide act as the hole and electron transport layers, sandwiching an active layer of $FAPbI_3$ with 250 nm thickness. In the first run of the washing process, 2-pentanol solvent was used to remove a portion of ligands, but high efficiency was not achieved. In the second step of the washing process, efficiency increased due to the positive effect of the toluene/acetonitrile mixture in washing the ligands. The highest efficiency of 8.38% was achieved when ethyl acetate was used (Fig.1.12(b)). This group was also successful in improving the efficiency of QD solar cells to above 12% due to the modification of electron transfer (Fig.1.12(c)) [60]. In more detail, after the third solid-state washing process, ITIC was spin-coated as the modifier. Based on the energy diagram in Fig.1.12(d), the conduction band energy of QDs is 3.78 eV and the conduction band energy of ITIC is 3.83 eV. Therefore, electrons have a better transfer capability from QDs to ITIC.

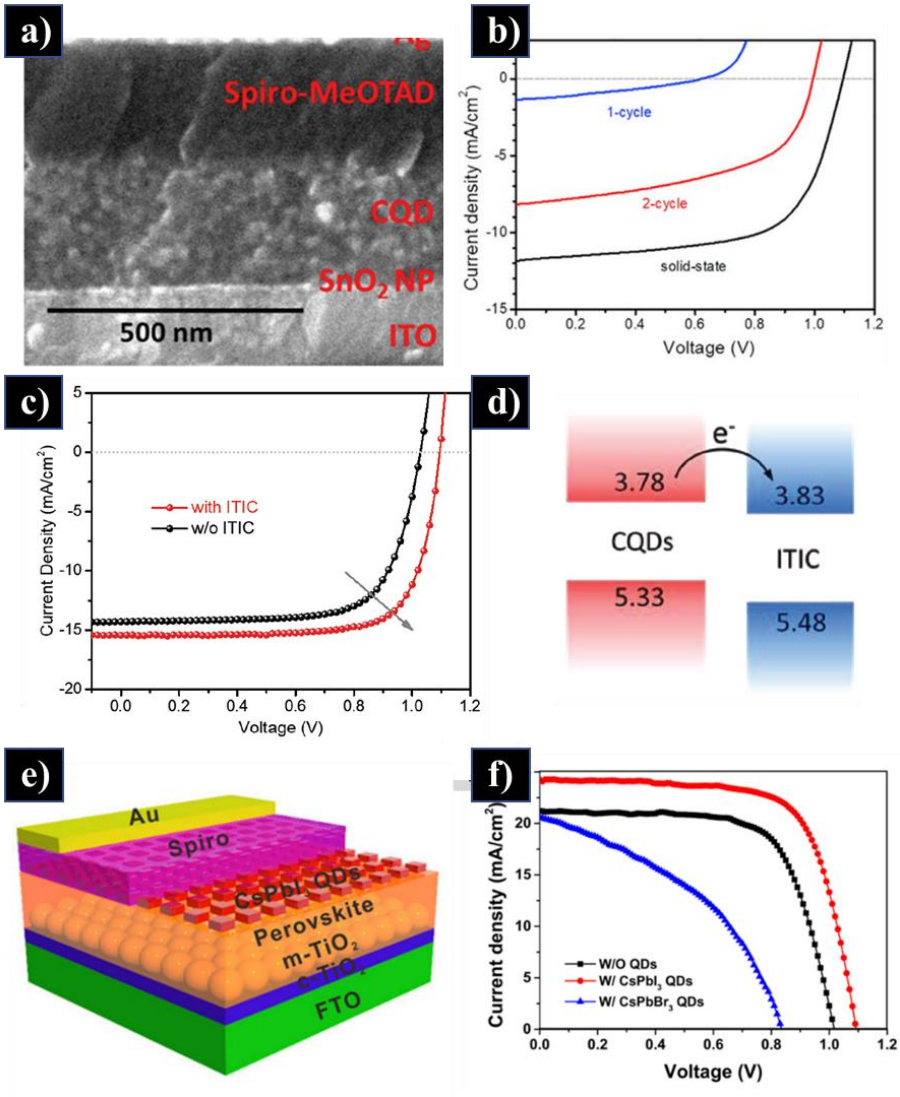

Figure 1.12. (a) SEM image showing the cross-section of the perovskite QDs solar cells. (b) I-V curve of perovskite solar cell QDs [51]. (c) I-V curve of perovskite solar cell QDs after electron transfer modification (d) Energy band diagram of PQDs and ITIC [52]. (e) Schematic diagram showing the configuration of the solar cell fabricated based on perovskite thin film/QD. (f) I-V curve of perovskite thin film/QD solar cell [53].

The second solution is to cast a thin layer of QDs on the bulk perovskite absorber layer to increase the efficiency. The PEDOT:PSS layer and TiO_2 were used as the hole and electron

transport layers, respectively. Methylammonium lead iodide and a mixture of formamidinium lead bromide and iodide with a ratio of 2 to 1 were used as the absorber layer. Although the QD-free bulk perovskite solar cell showed an efficiency of 4.72%%, introducing unpurified QDs between HTL and perovskite film resulted in the efficiency enhancement to 7.59%. It was revealed that the increase in current led to an increase in efficiency. In another study, Liu et al. [53] were able to synthesize $CsPbI_3$ QDs using the HI method. Ligand purification was also performed twice with ethyl acetate to remove the interfering ligands. As shown in Fig.1.12(e), to fabricate the solar cell, TiO_2 and spiro were employed as the electron and hole transporter layers. The bulk absorber layer was a combination of methylammonium and formamidinium lead iodide bromide, and $CsPbI_3$ QDs with a thickness of 30 nm. As shown in Fig.1.12(f), the efficiency of the film without QDs was 15.14%, while the efficiency reached 18.14% in the case of using QDs. However, when $CsPbBr_3$ QDs were spin-coated on the absorber layer, the efficiency decreased to 9%. The use of bromine instead of iodine not only reduces absorption and shifts the absorption edge to lower wavelengths but may also change the band energy structure acting as a barrier against carrier transferring. In contrast, by using $CsPbI_3$, all three parameters of current, voltage, and fill factor increased.

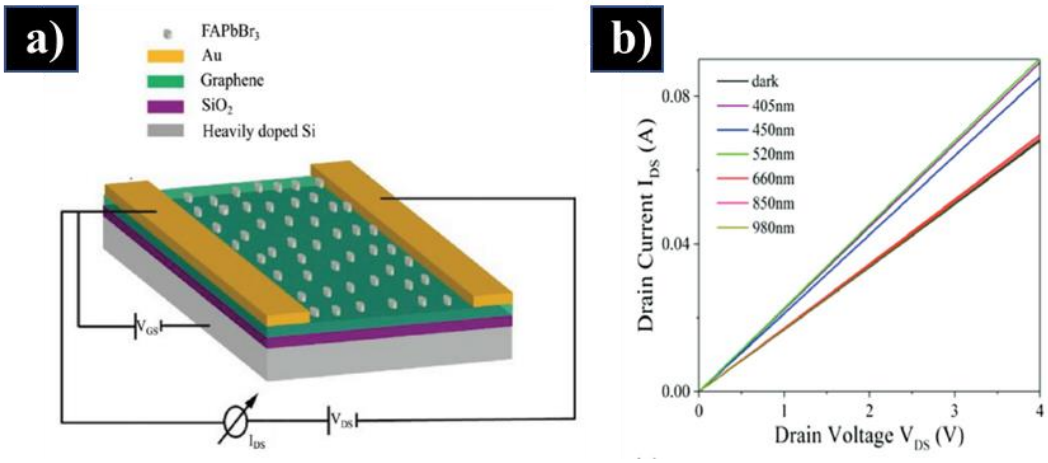

Figure 1.13. (a) Schematic diagram showing the configuration of the photodetectors fabricated based on graphene/perovskite QDs with the corresponding (b) I-V curves [54].

1.8.3. Photodetectors

Perovskite QDs have also indicated great power to be used in photodetectors and photodetectors. In one study, perovskite QDs were used to fabricate photodetectors [54]. As shown in Fig.1.13(a), a graphene layer was initially transferred onto a Si/SiO_2 substrate by using a poly(methyl methacrylate) (PMMA) method. Then, the PMMA was removed using acetone. Then, gold electrodes were then deposited onto the monolayer graphene using physical vapor deposition. Subsequently, QDs were spin-coated onto the substrate at 2000 rpm for 30 seconds. This photodetector exhibited optical responses under different illuminations. The responsivity was calculated at 1.15×10^5 at a bias voltage of 2 V under light power of 3 μW (Fig.1.13(b)). Table 1.1 lists photodetectors fabricated using perovskite materials, showing the great capability of graphene/perovskite QDs photodetectors [54].

Table 1.1. A list of photodetectors fabricated based on perovskites [54].

Active materials	**Substrate**	**Responsivity [A/W]**	**Light power**	**Bias voltage**
$MAPbBr_3$ /graphene	ODTS/SiO_2	180	1 μW	2 V
$MAPbI_{3-x}Cl_x$/CNTs	SiO_2	10^4	-	5 V
MoS_2/$MAPbI_3$	-	2.12×10^4	4.63 pW	-
WS_2/$MAPbI_3$	Sapphire	17	0.5 mW	-
Graphene/$MAPbBr_2$l	-	6×10^5	1.025 nW	-
WSe_2/$MAPbI_3$	Al_2O_3	110		2 V
$FAPbBr_3$ QDs/graphene	SiO_2	1.154×10^5		2V

2. Chapter 2: Materials & Methods & Characterization

In the previous chapter, an overview of the structure, characteristics, morphology, synthesis methods, and applications of perovskite QDs was presented. In this chapter, the materials, methods, and equipment used for the synthesis, characterization, and fabrication of QD-based devices are represented.

2.1. Research Objective

A general outline of the research objectives is provided in Fig.2.1. By taking advantage of the ligand-assisted reprecipitation process, $FAPbI_3$ QDs were synthesized. In this process, OA and OAm ligands were employed to not only assist ACN/GBL, as a low-coordinating solvent, in dissolving the precursors (PbI_2 and FAI) but also to control the size of QDs and passivate the surface of crystallized QDs after anti-solvent injection at room temperature. Then, the structural, morphological, and optical properties of QDs were investigated by XRD, FTIR, HRTEM, PL, and UV tests. Then, a SiO_2/Si wafer was diced and cleaned to be used as a substrate for the graphene/QD photodetector. First, graphene was transferred to Si/SiO_2 by PMMA method, followed by contamination removal using acetone and annealing treatments. This modification process was analyzed by Raman spectroscopy and Optical Microscopy. Then, Cr/Au electrodes were deposited on the surface of Si/SiO_2/Graphene with an interdigitated pattern using a shadow mask. In the next step, the channels between the source and drain (two electrodes) were filled with QDs using three different deposition methods, including drop-casting, spin coating, and centrifuge. Finally, the performance of graphene, QD, and graphene/QD photodetectors was tested by measuring I-V and I-t using a source meter.

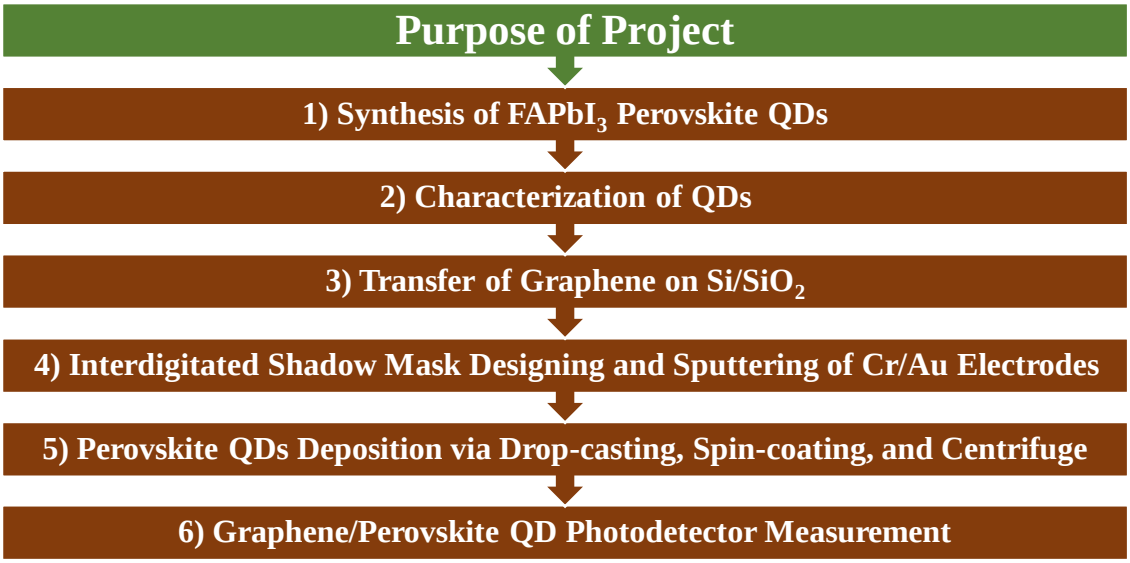

Figure 2.1. A general outline of research goals.

2.2. Materials

All the chemicals purchased and used for the synthesis of QDs and fabrication of photodetectors are listed in Table 2.1.

Table 2.1. A list of precursors used for the synthesis of QDs and the fabrication of photodetectors.

Precursors	**Molecular Formula**	**Role**	**Sigma Aldrich**
Lead Iodide	PbI_2 ($\geq$ 99.5%)	Precursors	Sigma Aldrich
Formamidinium iodide	$CH(NH_2)_2I$ ($\geq$ 99.5%)	Precursors	Sigma Aldrich
Oleic Acid	$C_{18}H_{34}O_2$ ($\geq$ 68-86%)	Ligand	Sigma Aldrich
Octylamine	$CH_3(CH_2)_7NH_2$ ($\geq$ 90%)	Ligand	Sigma Aldrich
Dimethylformamide	C_3H_7NO ($\geq$ 99.5%)	Solvent	Sigma Aldrich
Hexane	$CH_3(CH_2)_4CH_3$ ($\geq$ 95%)	Dispersant	Sigma Aldrich
Chloroform	$CHCl_3$ ($\geq$ 99.5%)	Antisolvent	Sigma Aldrich
Toluene	$C_6H_5CH_3$ ($\geq$ 99.5%)	Antisolvent	Sigma Aldrich
Acetonitrile	ACN ($\geq$ 99.8%)	Solvent	Sigma Aldrich
Chlorobenzene	C_6H_5Cl ($\geq$ 99.8%)	Antisolvent	Sigma Aldrich
Graphene on Cu	-	Conductive layer	Graphenea
Ammonium persulfate	$(NH_4)_2S_2O_8$	Etching agent	Sigma Aldrich
Si/SiO_2	-	Gate & Dielectric	Graphene Market
Au-Cr	-	Electrodes	Kert J. Leskar

2.3. Methods

2.3.1. Synthesis of $FAPbI_3$ QDs by LARP

As discussed before, to synthesize halide perovskite QDs, two general methods have been employed. Hot injection (HI) is the most commonly used process, comprised of two steps, starting with heating the precursors' solution, including a mixture of the metal acetates (FA acetate and Pb acetate), organic ligands (oleylamine (OM) and oleic acid (OA)), and a high boiling point solvent (1-octadecene), at above 100 °C in an N_2 filled flask. Then, the halide-based compound (FA iodide) is injected into the flask to induce the nucleation and growth of halide perovskite ($FAPbI_3$) NCs. Another facile, cost-effective, and room-temperature method is ligand-assisted reprecipitation (LARP). In this process, all of the compounds, including halide salts (FAI and PbI_2) and ligands are poured into a high coordinating solvent (DMF and DMSO), followed by injecting into the antisolvent (hexane), forming ($FAPbI_3$) QDs. These two processes have their advantages and disadvantages. In terms of crystallinity and morphology of the products, compared to the LARP process crystalizing NCs with irregular shapes, the HI method is capable of forming well-crystallized, narrow-sized, rectangular-shaped NCs [55]. Although HI can play an outstanding role in lowering the number of defects, leading to stronger radiative recombination, it has a complicated costly design. In contrast, LARP benefits from a facile structure, and inexpensive chemicals and instruments; however, it suffers from abundant defects inducing phase transformation and non-radiative recombination.

In this study, the LARP process was employed to synthesize $FAPbI_3$ QDs. The synthesis steps of $FAPbI_3$ QDs are depicted in Fig.2.2 and Fig.2.3.

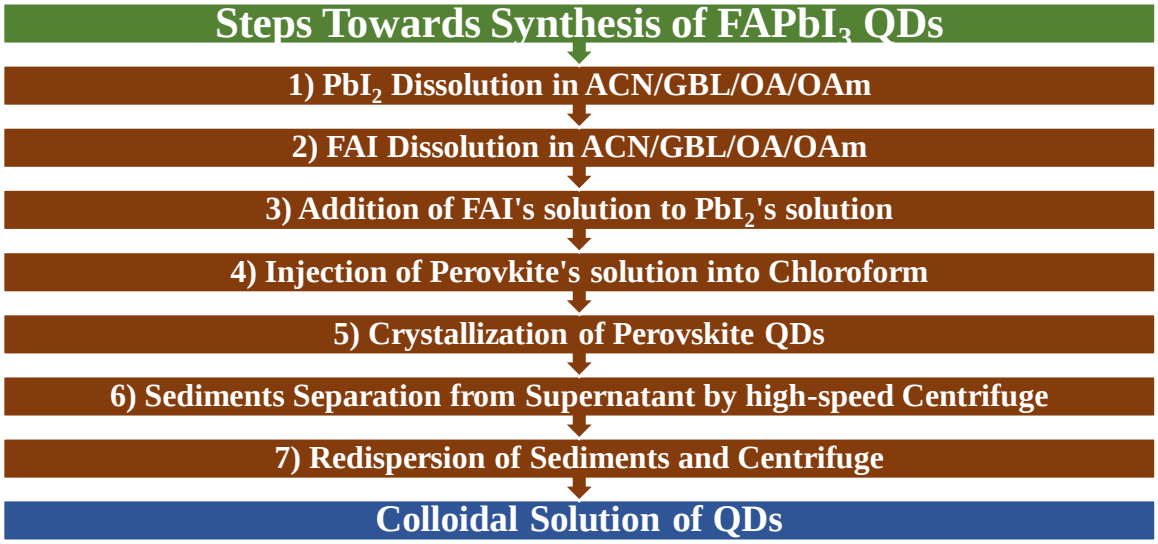

Figure 2.2. The graphic shows the main steps toward the synthesis of perovskite QDs and the fabrication of photodetectors.

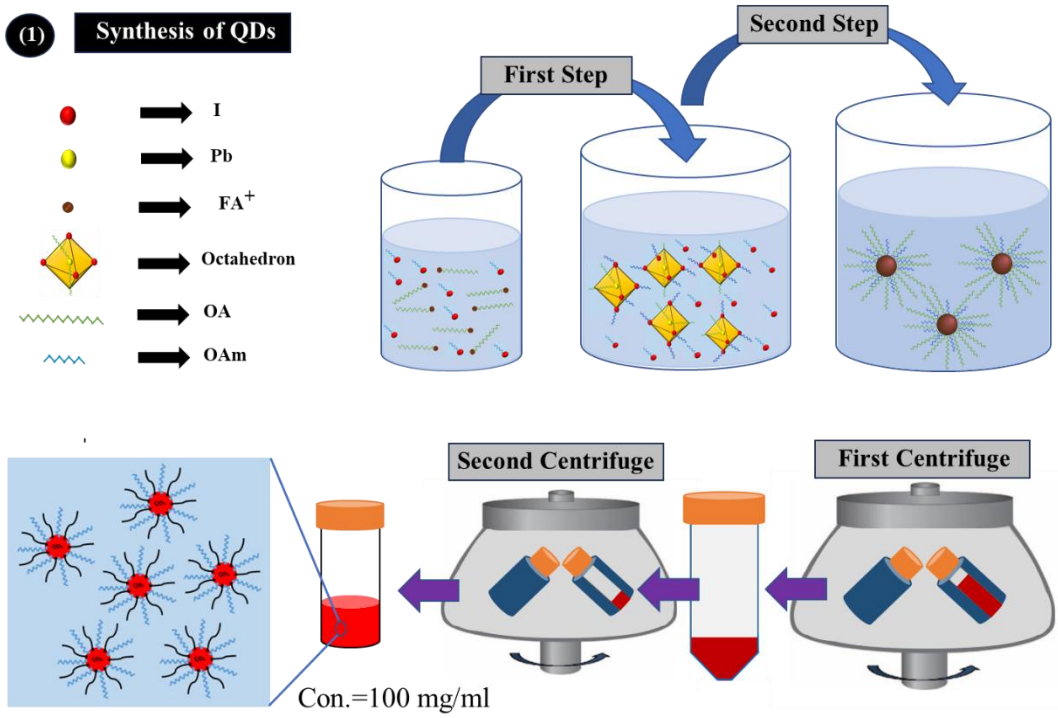

Figure 2.3. The schematic diagram shows how QDs are formed by the LARP and two-step centrifugation methods.

Due to the extreme solubility and coordination of PbI_2 in dimethylformamide (DMF) and dimethyl sulfoxide (DMSO) solvents with high polarity and dipole moment, they have been widely used in many research studies. However, when the solution of precursors is added to the antisolvent, the latter washes the former, inducing the crystallization of QDs. When the polarity index difference between solvent and antisolvent is high or the solvent is high-coordinating, the washing process becomes harder, leading to the formation of abundant ion vacancies. Based on the literature, although the UV–vis spectrum of PbI_2 depicts an absorption peak at 498 nm, related to the $[PbI_6]^{4-}$ octahedrons, DMF with high dipole moment (3.86 d) and high polarity index (6.4) shifts the peak to lower wavelengths at 370 nm, corresponded to the change of PbI_2 intrinsic structure by replacement of Pb–I with Pb–S (solvent) along with the formation of $[PbI_3S_3]^-$ octahedrons [56]. The formation of strong Pb–S bonds results in poor crystallization and creates abundant defects on the surfaces of QDs. These point defects located inside and on the surface of the synthesized QDs are prone to moisture, leading to non-radiative recombination and phase transformation from cubic to hexagonal.

To find the optimized volumes of ligands required to dissolve PbI_2 in ACN, several samples were provided (Table 2.2). The mechanism of PbI_2 decomposition and dissolution using OM and OA has been proposed in the literature [57]. Since ACN is incapable of deprotonating OA, octylamine assists in removing a proton (H^+) from OA. During this process, OA and OAm are transformed into oleate and octylammonium ligands, respectively **(**Equ.2.1 and Equ.2.2). This reaction was also experimentally observed when the transparent ACN/OA solution became milky after OAm injection. These two ligands

make a reaction to form an amino acid.

$$\text{-RCOOH+-RNH}_2 \rightarrow \text{-RCOO}^- + \text{-RNH}_3^+ \quad \text{(Equ.2.1)}$$

$$\text{-RNH}_3^+ + \text{-RCOO}^- \rightarrow \text{-RCOONH}_3 \quad \text{(Equ.2.2)}$$

While PbI_2 powders remained untouched in bare colorless ACN, the solvent became yellowish in the presence of oleate and ammonium ligands. The ammonium ligands disconnect the octahedrons and provide the oleates with enough space to react with the metal part (Equ.2.3).

$$\text{-RNH}_3^+ + \text{-RCOO}^- + PbI_2 \rightarrow \text{-COOPbI} + NH_3I \quad \text{(Equ.2.3)}$$

Table 2.2. PbI_2 dissolution in ACN with different concentrations of ligands.

	PbI_2 (mM)	**OA (µL)**	**OAm (µL)**	**OA/OAm**	**Result**	**ACN (mL)**
1	0.1	200	30	6.6	No	2
2	0.1	300	30	10	No	2
3	0.1	500	30	46.66	No	2
4	0.1	250	40	6.25	Yes	2
5	0.1	250	50	5	No	2

In the first step, PbI_2 (0.1 mMol or 0.0450 g), OA (200 µL), and OAm (20 µL) were poured in ACN (2 mL) and stirred for 5 min. However, after 20 minutes, a significant amount of PbI_2 was still undissolved. Although adding 300 and 500 µl of OA was found ineffective in dissolving PbI_2 and significantly increased the viscosity of the solution, adding octylamine increased the concentration of oleate ligands and enhanced PbI_2 dissolution. Exceeding octylamine above 50 µL either changed the morphology of perovskite from QDs to quantum wells or destroyed QDs. Therefore, 40 µL was selected as the minimum amount required to dissolve the major part of PbI_2 in 2 mL of ACN. In this case, the proportion of

OA/OAm is 6.25. To fully dissolve PbI_2, 300 µL of gamma-butyrolactone (GBL) was added to ACN. The smallest volume of GBL, with higher polarity than ACN and lower polarity than DMF, was used to fully dissolve the remaining powders since adding more ligands was found ineffective in solving the remaining precursors and increased the viscosity of the solution.

After preparing the PbI_2's solution, FAI powders were poured into the lead iodide solution. However, as seen in Fig.2.4(a), the solution turned red and eventually brown, indicating that perovskite was formed before the injection of the precursor's solution into the anti-solvent. Fig.2.4(b) shows that no emission under UV light is visible due to the unlimited growth of perovskite.

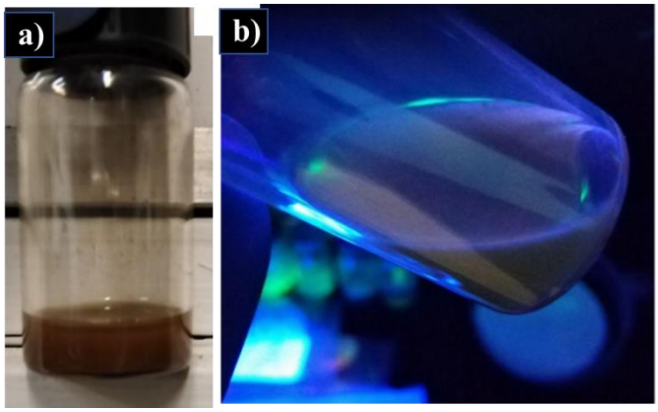

Figure 2.4. the solution of PbI_2 after adding FAI powders (a) without and (b) under UV light.

To solve this problem, FAI powders were also dissolved in another container. To achieve this, 0.0137 g of FAI was dissolved in a solution containing 0.5 mL of acetonitrile, 50 µL of OA, and 8 µ of octylamine. Similar to the PbI_2 solution, oleate and ammonium react with FAI, resulting in the formation of formamidinium oleate and ammonium iodide (Equ.2.4 and Equ.2.5). The optimized solutions of lead iodide and FAI can be observed in Fig.2.5(a,

b). Finally, the yellowish solution of FAI was injected into the PbI_2 solution while stirring and no unwanted particles were formed.

$$CH(NH_2)_2^+ + \text{-}COO^- \rightarrow COOCH(NH_2)_2 \quad \text{(Equ.2.4)}$$

$$I^- + \text{-}NH_3^+ \rightarrow NH_3I \quad \text{(Equ.2.5)}$$

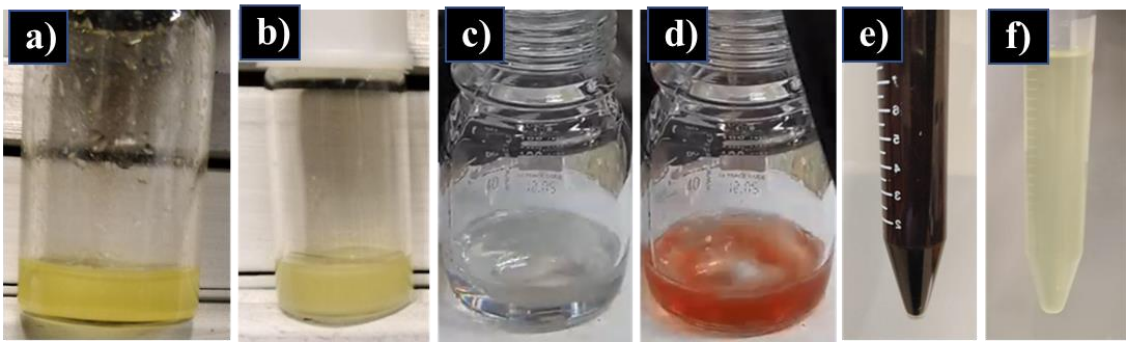

Figure 2.5. The solution of (a) PbI_2 and (b) FAI. Chloroform (c) before and (d) after injection of 100 μL, and (e) perovskite particles solution. (f) Non-perovskite phase formed after injection of perovskite precursors, dissolved in DMF, into chloroform.

Finally, by adding the first 100 μL of the precursor solution into 10 mL toluene, the solution turned red, as shown in Fig.2.5(c, d), indicating the formation of $FAPbI_3$ QDs (Fig.2.5(e) and Equ.2.6). The process continued until all precursors were injected, changing the color of the solution from red to brown. In the final solutions, the ligands are either attached to the surface of QDs or are free.

$$COOPbI + NH_3I + NH_3I + COOCH(NH_2)_2 \rightarrow CH(NH_2)_2PbI_3 + \text{Ligands} \quad \text{(Equ.2.6)}$$

As seen in Fig.2.5(f), when DMF was chosen as the solvent, it was observed that after 300 μL injection of the perovskite solution, the color of the antisolvent changed from red to yellow, indicating perovskite degradation.

In the final step, large particles and QDs were separated from the solution using a high-speed centrifuge at 12000 rpm for 30 min. After settling all the sediments at the bottom of the centrifuge tube, the supernatant was discarded, and all the sediments were dispersed in 1 mL hexane. Then, larger particles were separated from QDs by using another centrifugation at 5000 rpm for 5 min.

To measure the concentration of QDs, the colloidal solution of QDs was dropped on a glassy petri dish and the solvent was evaporated under the fume hood. The average concentration of the $FAPbI_3$ colloidal solution was determined to be 93 mg/mL based on the following equation:

$$C = \frac{W_2 - W_1}{1\ mL} \qquad \text{(Equ.2.7)}$$

Where C, W_2, and W_1 are the concentration of QDs, and weight of the petri dish with QDs and without QDs, respectively.

The reason behind using hexane as a medium for the suspension of QDs is that polar solvents break the ionic bond between ligands and QDs, accelerating either the agglomeration or degradation of QDs.

2.3.2. Wafer Dicing and Cleaning

Regarding the substrate, a 4-inch Si/SiO_2 wafer, purchased from “Graphene Market”, was diced into 62 pieces with a size of 1 cm×1cm via a dicing machine (Fig.2.6, step 2). Unexpectedly, there was a thin film of SiO_2 on the backside of Si that should be removed. Two different methods were used to remove the oxide layer. Firstly, a wet etching process in different etchants (KOH or HF (40%)) and designs (Kapton taping or a PTFE container) was employed (Fig.2.6, step 3). In terms of KOH, the etching rate of Si is higher than that

of SiO_2; however, HF only etches the oxide layer without any negative effect on Si. Although wet etching is an effective way to remove the oxide layer, however, HF is extremely toxic, and multiple washing steps are required to make sure HF is removed. Therefore, a dry etching process based on fine grinding and polishing was used. Finally, substrates were ultrasonically cleaned with DI water, acetone, and ethanol for 15 min, respectively, followed by UV Ozone treatment for 15 min to remove the surface contaminations (Fig.2.6, step 4).

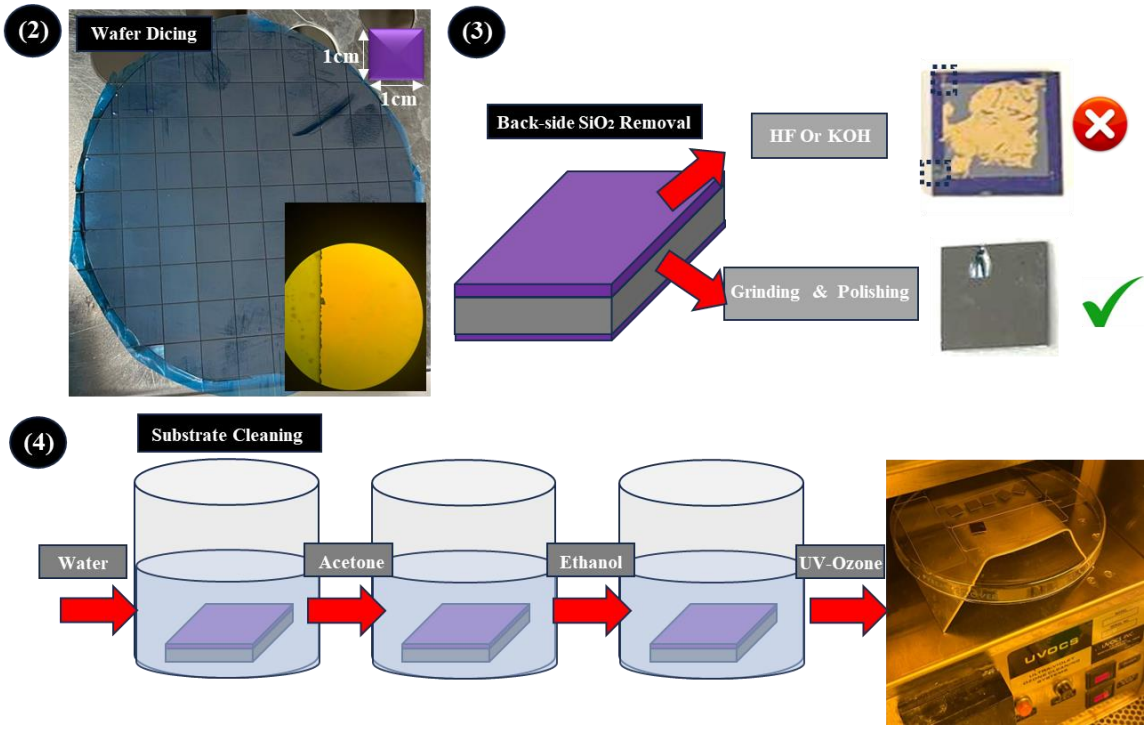

Figure 2.6. Substrate preparation: (2) wafer dicing (3) backside SiO_2 etching (4) substrate cleaning by water, acetone, ethanol, and UV-Ozone treatment.

2.3.3. Transfer of Graphene

Monolayer graphene has been widely grown on transition metals, as a catalyst, by the chemical vapor deposition (CVD) process. The metal substrate not only plays an

outstanding role in lowering the reaction energy barrier but also determines the mechanism of graphene growth. For instance, Ni and Fe with high carbon solubility dissolve abundant carbon atoms, followed by carbon segregation on the surface during cooling, leading to graphene sheet formation. In contrast, Cu with low carbon solubility induces the nucleation and lateral growth of decomposed carbon atoms to form graphene domains [58]. One of the most common ways to prepare a 1 cm graphene single crystal on Cu is to expose O_2 to the substrate (1×10^{-3} Torr), followed by annealing a mixture of CH_4/H_2 (1×10^{-3} Torr/0.1 Torr) at 1035 °C.

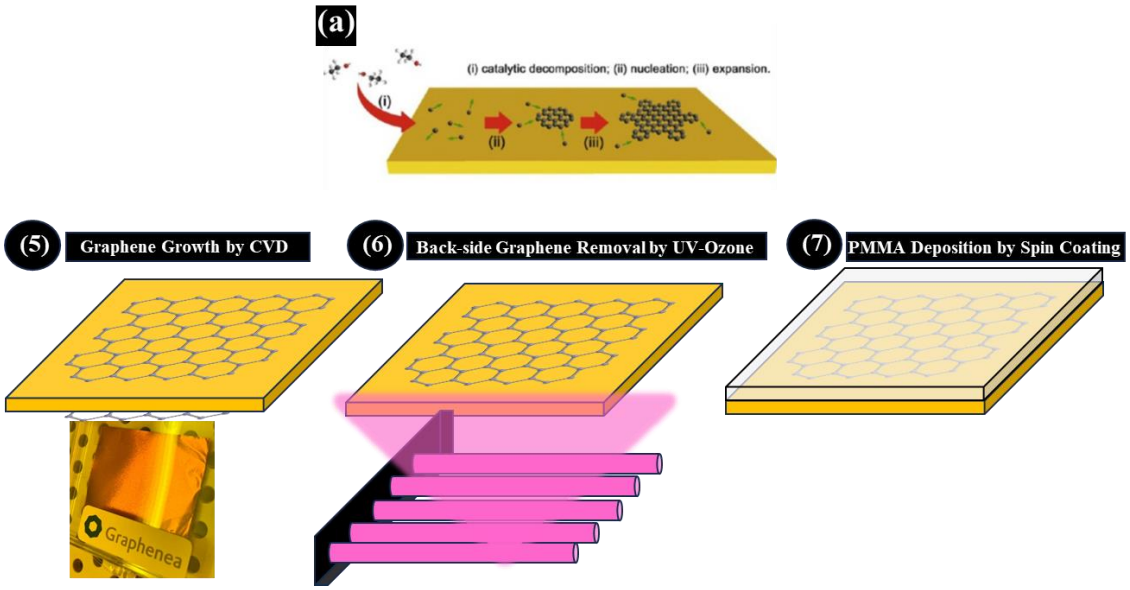

Figure 2.7. (a) Mechanism of graphene nucleation and growth by CVD process [58]. Graphen transfer: (5 and 6) backside graphene removal by UV-Ozone treatment (7) PMMA deposition.

CVD-grown large-area monolayer graphene purchased from “Graphenea” (Fig.2.7, step 5). Firstly, Cu/graphene was cut with a size of 6.5 mm×6.5 mm. During the CVD process, graphene is formed not only on the surface of copper but also on the backside of the

substrate. Failing to remove the backside-grown graphene results in conductivity reduction due to the layers' overlap during transfer. Therefore, in the next step, graphene on the backside of Cu foil is removed by UV-Ozone treatment for 5 min (Fig.2.7, step 6). Then, a 2% solution of PMMA in chlorobenzene is spin-coated at 3000 rpm for 30 s onto the substrate, followed by baking at 60 °C for 2 min (Fig.2.6, step 7).

The next step is Cu etching by floating the Cu/CV-grown graphene/PMMA-passivated foil on a 0.1 M Ammonium persulfate $(NH_4)_2S_2O_8$ (APS, Sigma-Aldrich) solution. As seen in Fig.2.8 step 8, some portions of Cu disappear, and after 3 h, no remarkable Cu was observed. It is interesting to note that APS exposure for less than 3 h failed to remove the whole Cu while treating for more than 12 h caused PMMA disintegration. The graphene/PMMA should be purified before transferring to the Si/SiO_2 substrate. Since graphene/PMMA is extremely flexible, a clean slide glass was used to scoop out and place it into a petri dish filled with fresh DI for ~12 h (Fig.2.8, step 9). This cleaning process was repeated twice to make sure the remaining Cu ions were removed.

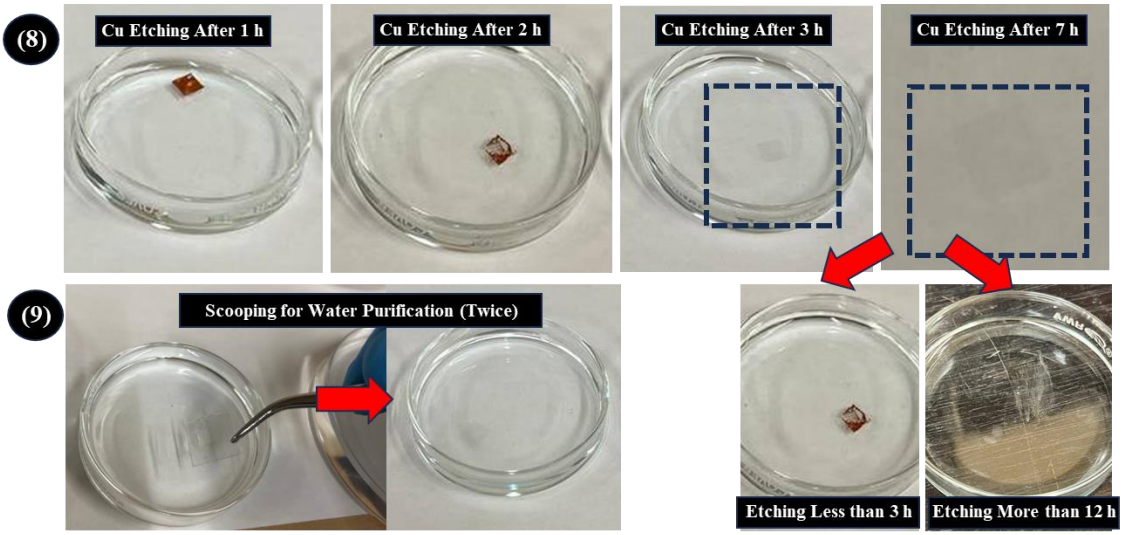

Figure 2.8. Copper etching: (8) Etching Cu/graphene/PMMA in APS solution for 1, 2, 3, 7, and 12 h. (9) Water purification of graphene/PMMA.

Finally, the PMMA/graphene layer was transferred to a Si (n^{++})/SiO_2 (285 nm) substrate (Fig.2.9, step 10). Then, by using the high-pressure N_2 gas graphene was firmly attached to the SiO_2 (Fig.2.9 step 11). After transferring the graphene/PMMA sheet, the sample is annealed at 85 °C for 5 min, 135 °C for 25 min, and 180 °C for 85 min to evaporate the trapped droplets of water, enhancing the attachement between the graphene and SiO_2 (Fig.2.9 step 12). This gradual increase in temperature is an effective deterrent against the uncontrollable evaporation of the remaining water that tears up the graphene. PMMA acts as a protecting role that should be removed since it's an insulating layer and greatly decreases the conductivity of carriers. Based on the polymers handbook, polar solvents are capable of dissolving polymers like PMMA. Firstly, the effect of dipping the substrate in an acetone bath at 65 °C for 1 h, followed by acetone treatment at room temperature overnight was investigated (Fig.2.9 step 13). Then, the impact of other polar solvents such

as DMF, DMSO, chloroform, and chlorobenzene was tested. Then, the substrate was placed in isopropanol at 65 °C for 30 min, followed by N_2 drying.

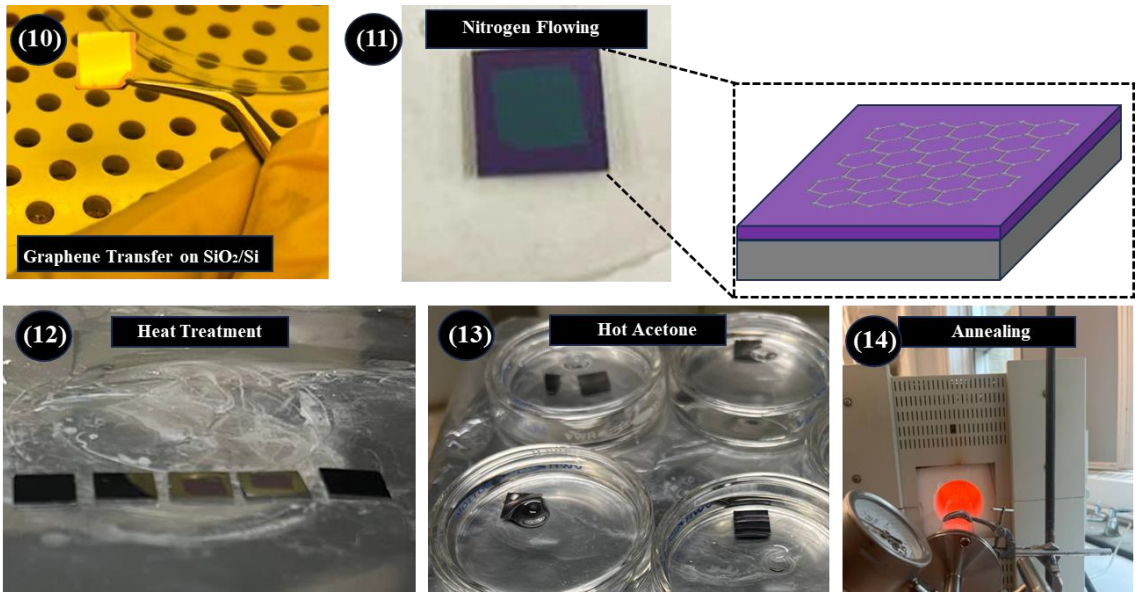

Figure 2.9. Graphene transfer: (10) Scooping the graphene on Si/SiO_2 substrate. (11) Nitrogen flowing. (12) Heat treatment. (13) Hot acetone treatment. (14) Annealing process at 850 °C for 14 h.

In the next step, the substrates were annealed at various temperatures (700, 750, 800, and 850 °C) for different temperatures (6, 9, and 12 h) in the presence of Ar gas (Fig.2.9 step 14). Graphene is highly sensitive to oxygen and high temperatures above 1000 °C, increasing the probability of graphene oxide formation or graphene decomposition, respectively. To make sure the sample was free of dust and contaminations, the substrates were cleaned with ethanol for 30 min.

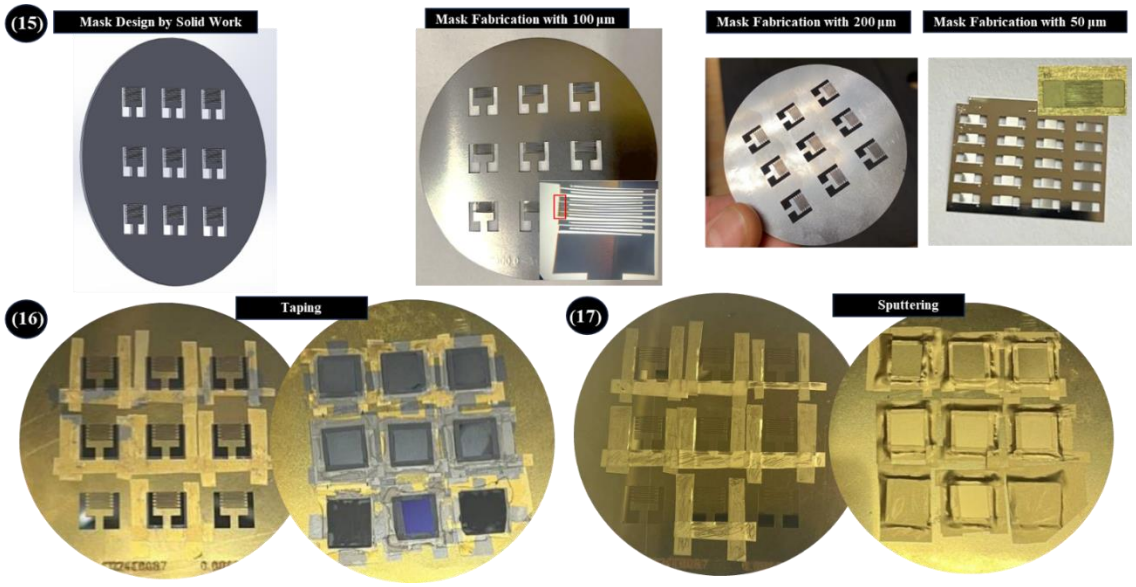

Figure 2.10. Shadow mask design and electrodes sputtering. (15) Designing two shadow masks with channel lengths of 200 µm and 50 µm. (16) Taping substrates to the shadow mask. (17) Sputtering Cr/Au electrodes on the substrate with thicknesses of 20 and 200 nm, respectively.

2.3.4. Mask Design & Mask Fabrication & Electrodes Deposition

To deposit the electrodes with different channel lengths on the surface and backside of the substrates, two shadow masks with an interdigitated pattern were employed. To design the first shadow mask, SOLIDWORK software was used (Fig.2.10 step 15). Then, the mask with a channel length of 200 µL was fabricated by Stencils company. Another shadow mask with a channel length of 50 µL was purchased from Ossila. The active areas of the masks are 0.08 and 0.01 cm^2, respectively.

Regarding electrode deposition, physical vapor deposition (PVD) has been widely used. Although thermal vacuum evaporation, in which the target is evaporated from a crucible and physically settled on the surface of a substrate, does not damage the transferred graphene during deposition, it decreases the gold adhesion to the graphene or substrate, on

one side, and was unavailable on campus, on the other side. Therefore, sputtering was used to deposit gold on the substrate. Before sputtering, the substrates were firmly taped to the shadow mask (a portion of the surface of the substrate is covered with the shadow mask, and the edges of the backside of the substrate are covered with tape) (Fig.2.10 step 16). Since gold is easily removed from the substrate by alligator clips during measurement, chromium was deposited before gold. To mitigate the negative impact of collisions between graphene and target atoms, the deposition rate was started at 0.3 A°/s, and after the thickness of 100 A°, it increased to 0.7 A°/s to reach thicknesses of 200 A° and 2000 A° for chromium and gold, respectively (Fig.2.10 step 17).

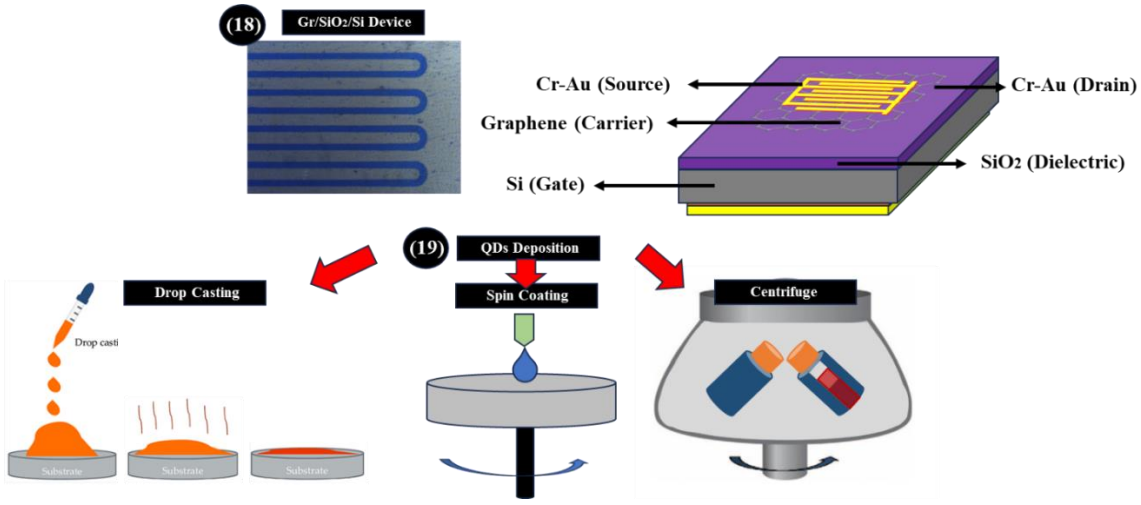

Figure 2.11. QDs deposition: (18) The image of Cr-Au/Si/SiO_2/Graphene/Cr-Au. (19) Deposition of QDs on the device via drop casting, spin coating, and centrifuge methods.

2.3.5. QDs Deposition on Si/SiO_2 Substrate

The schematic diagram (right-hand image) and the photograph of the substrate (left-side image) illustrate the graphene photodetector with a configuration of Cr-Au/Si/SiO_2/Graphene/Cr-Au (Fig.2.11 step 18). To fabricate a photodetector based on the

Gr/QD, QDs were deposited on the device by different methods. There are three deposition methods for casting QDs on the device, including drop-casting, spin-coating, and centrifuge (Fig.2.11 step 19). In the first method, 50 μL of colloidal solution of $FAPbI_3$ perovskite QDs was dropped on the device and n-hexane with a boiling point of ~ 68 °C was evaporated under a fume hood, followed by an annealing process at 60 °C for 5 min. Regarding spin-coating, the backside edges of the substrate were taped to the aluminum foil, that was firmly attached to the spin-coating holder. Then, 50 μL of colloidal solution of QDs was spin-coated on the device with a speed of 2000 rpm for 30 s, followed by an annealing process at 60 °C for 5 min. This process was repeated five times. Compared to the above processes, the centrifuge method was first introduced by Prof. Ted Sargent to fabricate a PbS-based solar cell device. To achieve the same goal for $FAPbI_3$ QD-based photodetectors, firstly, the volume of the QDs solution increased to 5 ml, and then, the substrate was placed into the centrifuge tube in a way that the surface faced the center of the centrifuge machine. Then, the substrate was centrifuged at 4000 rpm for 10 min, followed by an annealing process at 60 °C for 5 min.

2.4. Quantum Dot and Device Characterization

2.4.1. X-ray Diffraction

X-ray diffraction was used to determine the characteristic peaks and crystalline planes of perovskite and non-perovskite phases. To prepare the XRD sample of QDs, different methods were used. One of the methods was spin coating, however, ligands were strong obstacles against QD film thickening. To have a thicker layer of QDs, 2 mL of QDs solution was drop-casted on the silicon carbide substrate, followed by drying under the fume hood.

However, due to the presence of oleic acid on the surface of the QDs, complete drying was not achievable. To obtain a suitable layer, the centrifugation method was used. This process prepared not only a thick but also a fully dry layer of QDs due to the centrifugal force resulting in partial ligand detachment. This test was conducted using X-rays produced from a copper lamp with a wavelength of 1.5450 °A.

2.4.2. High-Resolution Transmission Electron Microscopy (HRTEM)

Using the image mode of high-resolution transmission electron microscopy (HRTEM), size distribution, morphology, and crystalline structure (by calculating the interplanar spacing (d) using Gatan software) were determined. OA and OAm passivating ligands are insulators and make the QDs unclear. Therefore, it is highly required to purify the QDs from ligands by using methyl acetate. To achieve this, methyl acetate was added to the fresh synthesized QDs before the first run of the centrifuge. After preparing the colloidal solution of QDs, it was diluted up to 100 times, ultrasonicated, and then poured onto a carbon grid. Equ.2.8 was utilized to determine the observed plane indices in high magnification.

$$n\lambda = 2d\sin\theta \qquad \text{(Equ.2.8)}$$

$$1\times0.15405(\text{nm}) = 2\times0.212(\text{nm})\times\sin\theta$$

$$\theta = \sin^{-1}\left(\frac{0.15405}{2\times0.212}\right)=21.3^{o}$$

$$2\theta = 42.6^{o}$$

$$\theta = \sin^{-1}\left(\frac{0.15405}{2\times0.364}\right)=12.21^{o}$$

$$2\theta = 24.4^{o}$$

2.4.3. Photoluminescence and UV-Visible Spectroscopy

To assess the optical properties, PL and UV-vis tests were carried out. To achieve this, one of the wells of a 96-well microplate was filled with 200 µl of QDs colloidal solution. In the PL test, QDs were excited using different light sources with wavelengths of 500, 550, 600, 650, 700, 750, and 800 nm. As a result of excitation, abundant electrons are excited to the conduction band and holes are generated in the valence band. Then, photogenerated carriers are radiatively recombined and the light is emitted and detected. For UV-visible spectroscopy, the absorbance of $FAPbI_3$ QDs was monitored at different wavelengths in the range of 300 nm to 1000 nm. To find the edge of absorbance, there are different ways. Some types of QDs have a peak in their absorbance spectrum. In another case, the intersection of two lines at a point where the curve suddenly rises is considered the absorption edge. In the last case, the wavelength that has the highest absorption value after the significant rise is regarded as the absorption edge.

2.4.4. Fourier Transform Infrared Spectroscopy (FTIR)

Fourier Transform Infrared Spectroscopy (FTIR) was used to investigate the type of chemical bonds present in ligand-passivated $FAPbI_3$ QDs.

2.4.5. Band Gap Calculation Energy Using Tauc Plot Method

The calculation of band gap energy was performed using a method called Tauc plot. To achieve this, the energy for various wavelengths was calculated using Equ.2.9, which forms the horizontal axis of the graph [59].

$$E(ev)=hv=\frac{hc}{\lambda}=\frac{1240}{\lambda(nm)} \qquad \text{(Equ.2.9)}$$

Then, using Equ.2.10, the vertical axis, which represents $(\alpha h\upsilon)^{1/r}$, was calculated. Since perovskites have a direct bandgap, r is equal to 0.5, the equation is simplified to $(\alpha h\upsilon)^2$. α represents the absorption coefficient, which is calculated as follows:

$$\alpha=\left[2.303(abs)\right] \quad \text{(Equ.2.10)}$$

In the above formula, abs is the absorption value obtained from UV-vis spectroscopy. After plotting the graph of $(\alpha h\upsilon)^2$ versus hν, the band gap energy is calculated by the extrapolation of a line touching the spectrum and intersecting with the horizontal axis, representing the bandgap energy of the $FAPbI_3$ QDs.

2.4.6. Raman Microscopy

μ-Raman spectroscopy was used to study the changes in graphene after transfer on the substrate. To achieve this, by using optical microscopy, the target position was recognized, and then, excited by a 532 nm laser with a power of 10%.

2.4.7. Device Measurement

After the characterization of QDs and fabrication of devices, the performance of photodetectors was assessed. Firstly, LEDs should be mounted and fixed on an object to make the measurement process more precise. Therefore, a model was designed and by using 3D printing, named fused deposition modeling (FDM), an object was printed (Fig.2.12 step 20). Then, an optical power meter was placed below the object and different LEDs, including UV, blue, green, yellow, and red LEDs were mounted on the object, facing the optical power meter at a fixed distance and the optical powers of LEDs were measured (Fig.2.12 step 21). In the absence of the gate voltage, only one source meter was used to sweep the voltage and measure the current between the source and drain. In the presence

of gate voltage, one source meter is added to sweep the voltage and measure the current between the gate and source. These measurements were carried out in the dark and under illumination with different optical powers (Fig.2.12 step 22).

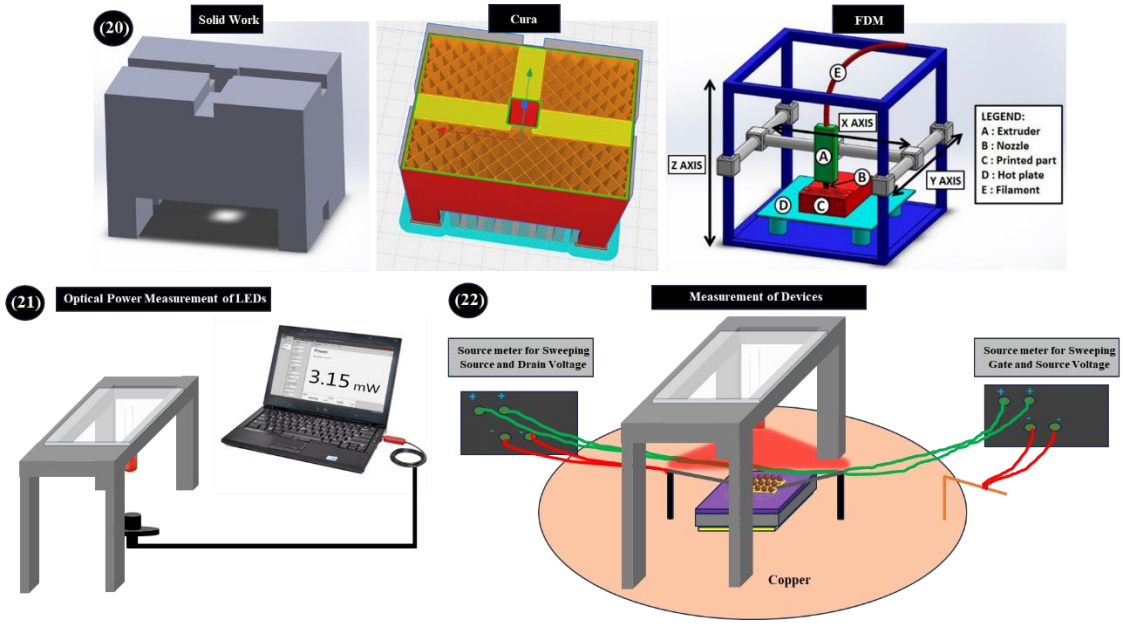

Figure 2.12. I-V measurements. (20) Modeling and printing a holder for LEDs via FDM. (21) Using an optical power meter to measure the optical power of LEDs. (22) Measuring the performance of photodetectors by using two source meters.

3. Chapter 3: Results and Discussion

In this section, the structural, morphological, and optical properties of $FAPbI_3$ QDs were investigated by XRD, HRTEM, FTIR, UV-vis, and PL. Raman spectroscopy and optical microscopy were used to assess the quality of graphene transfer on the substrate. Finally, the performance of Gr/QD photodetectors under different conditions was assessed.

3.1. HRTEM of $FAPbI_3$ QDs

To study the morphology, size distribution, and phase of $FAPbI_3$ QDs, HRTEM was employed. Fig.3.1(a) illustrates the unit cell of $FAPbI_3$ plotted using VESTA software. Regarding the $FAPbI_3$ unit cell crystal structure, the black lead atom is surrounded by six purple iodine atoms in an octahedron. The formamidinium cation occupies the center of eight connected PbX_6 octahedrons. Fig.3.1(b) shows that $FAPbI_3$ QDs have semi-spherical shapes with a narrow size distribution of 7.5 ± 1.4 nm (Fig.3.1(c)). Considering two different QDs in high magnifications (Fig.3.1(d)), the interplanar spacings (d) were calculated to be 0.212 nm and 0.364 nm, respectively. By applying the corresponding values to the equ.2.8, the diffraction angles (2θ°) were calculated to be 42.6 ° and 24.4 °, respectively. These diffraction angles correspond to the (300) and (111) planes of α-$FAPbI_3$, confirming the alpha phase was formed.

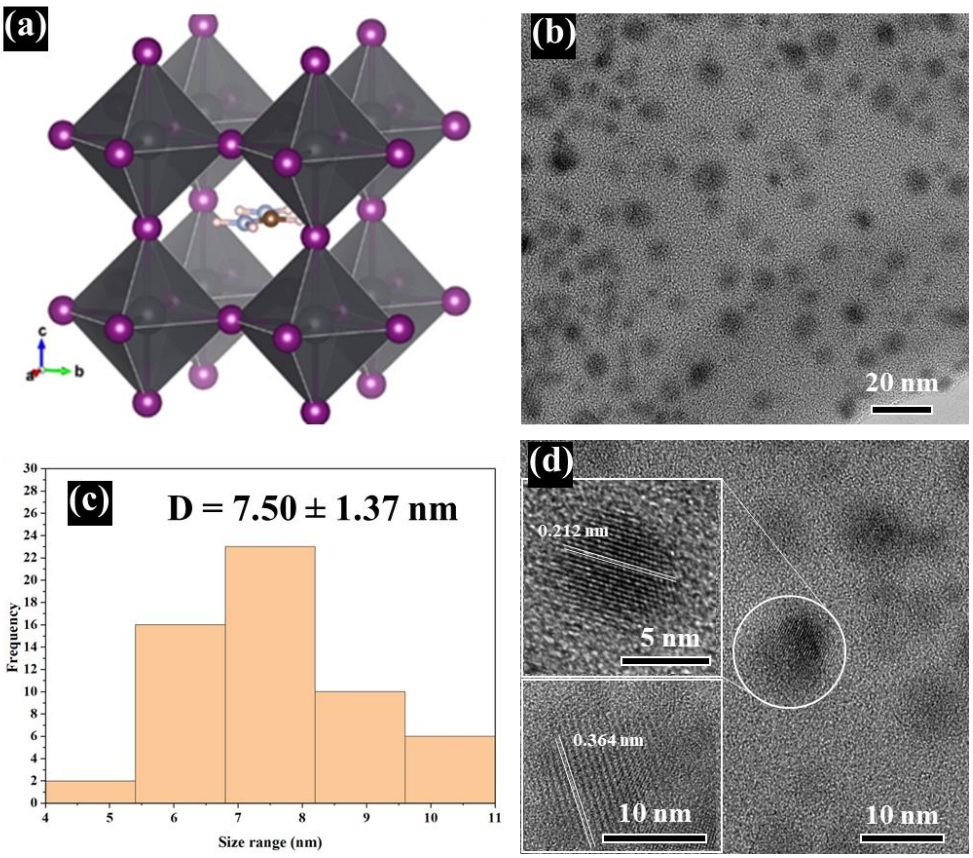

Figure 3.1. (a) Unit cell of $FAPbI_3$. (b, d) HRTEM and (c) size distribution of $FAPbI_3$ QDs.

3.2. XRD of $FAPbI_3$ QDs

As discussed, $FAPbI_3$ has two phases stable at different temperatures. The α- $FAPbI_3$ has a cubic crystal structure stable at temperatures above 160 °C. This phase with black color has desirable optical and electrical properties due to its direct bandgap energy of about 1.47 eV. In contrast, the non-perovskite yellow delta phase (δ- $FAPbI_3$) with a hexagonal structure has a large bandgap energy of 2.32 eV with poor optical properties stable at room temperature. Fig.3.2 depicts the XRD pattern of $FAPbI_3$ QDs as well as crystallographic information files (CIFs) of PbI_2, α- $FAPbI_3$, and δ- $FAPbI_3$. The preparation process of QDs on SiC was explained in more detail in the previous section. Then, corresponding peaks to

the SiC substrate were recognized via X'Pert software and removed. Fig.3.2 and Table 3.1 show that intense and broad peaks at diffraction angles (2θ°) of 13.91, 19.73, 24.22, 28.04, 28.43, 34.52, 40.08, 42.62, 45.05, 47.38, 49.63, 51.80 ° were attributed to (100), (011), (111), (200), (210), (211), (220), (300), (310), (311), (222), (320) planes of alpha phase of $FAPbI_3$ QDs, confirming that the alpha phase of $FAPbI_3$ was formed. The driving force behind the crystallization and stabilization of alpha-phase at room temperature is related to the size effect. In other words, significant size reduction not only influences the optical properties but also greatly reduces the phase transformation temperature, as reported for other semiconductor QDs [16]. Regarding peak broadening, $FAPbI_3$ QDs exhibit broader XRD peaks than bulk $FAPbI_3$ due to the size effect and structural distortions.

Moreover, some of the precursors might not have participated in the perovskite formation reaction or might have converted to the initial precursors due to the perovskite destruction. PbI_2 is one of the precursors that may be present in the QDs. Comparing the XRD pattern of $FAPbI_3$ QDs and CIF of PbI_2, no intense peak related to PbI_2 was observed. However, some weak peaks corresponding to δ-$FAPbI_3$ were detected. Perovskites are sensitive to severe conditions, especially moisture, inducing the phase transformation from alpha to delta. Since I did not have access to any glovebox, $FAPbI_3$ QDs were synthesized in ambient conditions. Therefore, although QDs were synthesized in an environment with a humidity percentage of 40%, almost the whole crystallized phase was alpha, which can be related to the outstanding effect of ACN/GBL.

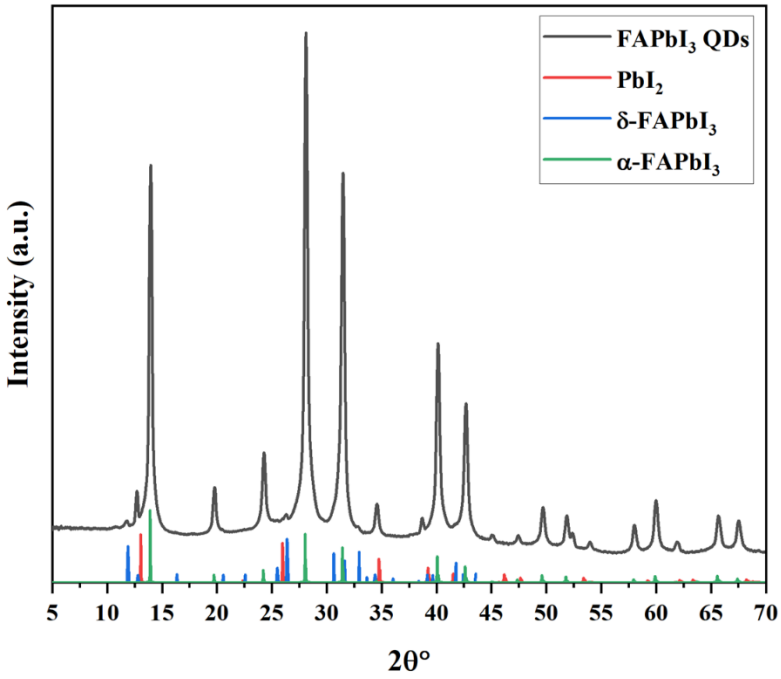

Figure 3.2. XRD pattern of $FAPbI_3$ QDs, and CIF files of PbI_2, α- $FAPbI_3$, and δ-$FAPbI_3$.

Table 3.1. Diffraction angle and corresponding planes of $FAPbI_3$ QDs.

2θ°	13.91	19.73	24.22	28.04	28.43	34.52	40.08	42.62	45.05	47.38	49.63
Plane	(100)	(011)	(111)	(200)	(210)	(211)	(220)	(300)	(310)	(311)	(222)

3.3. UV-vis and PL of $FAPbI_3$ QDs

UV-vis and PL were used to determine the absorption edge and emission peak of $FAPbI_3$ QDs. Regarding UV-vis in Fig.3.3(a), by increasing the wavelength from 900 nm to 780 nm, there is no significant change in the slope of the spectrum, showing the $FAPbI_3$ QDs have no absorption in this region. Increasing the source wavelength below 780 nm, the curve takes a rising upward trend reaching the highest absorption value at 682 nm,

considered as absorption edge. In terms of PL testing, different excitation sources with wavelengths of 600, 650, 700, 750, and 800 nm were used. As seen in Fig.3.3(b), the maximum intensity of the emission peak was observed at 751 nm when the QDs were excited by the light source with a wavelength of 660 nm. As can be seen in the inset of Fig.3.3(b), the brownish colloidal solution of $FAPbI_3$ QDs emits intense red emission under UV light (λ_{exc}=365 nm). These results also confirm that the alpha phase with fascinating optical properties was formed. The emission peak and absorption edge were significantly shifted to lower wavelengths compared to that of bulk $FAPbI_3$. In addition, by increasing the excitation wavelength the maximum PL intensity decreases, and the emission wavelength is shifted to higher wavelengths. Moreover, Stokes shift is one of the most important characteristics of QDs, defined as the difference between the emission peak and absorption edge, approaching almost zero in bulk samples. In the case of $FAPbI_3$ QDs, the difference between the emission peak and absorption edge is about 70 nm. All of these results confirm the presence of the quantum confinement effect [60]. In addition, the full width at half maximum (FWHM) of the emission peak was calculated to be 62 nm. Smaller values of FWHM are preferable, giving rise to performance enhancement of optoelectronic devices, including light-emitting diodes and photodetectors. In the case of the former, the broader emission peak decreases the purity of the emitted light. In terms of the latter, a random accommodation of QDs with large size differences, or high bandgap energy differences, induces carrier trapping. Moreover, among all perovskites (cation: methylammonium and cesium, and anion: bromine and chlorine), FA and I have the largest radius, leading to the largest FWHM.

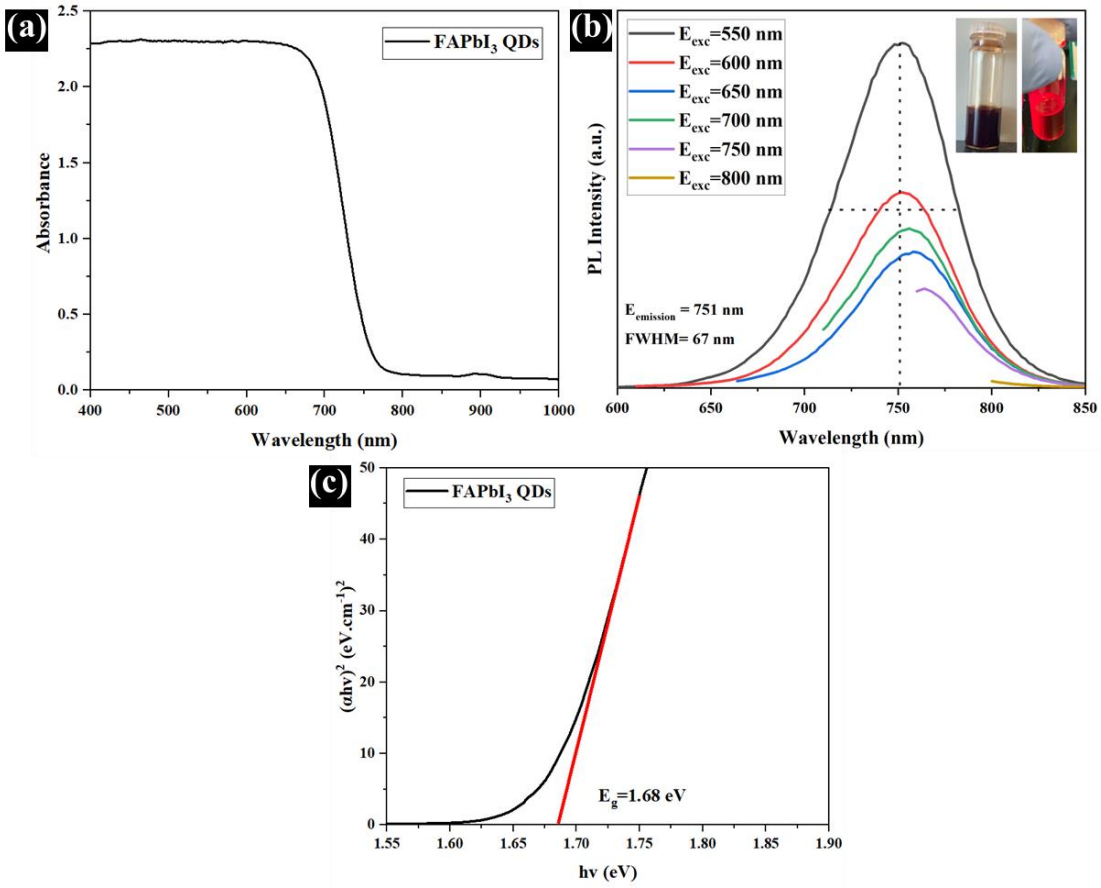

Figure 3.3. (a) UV-vis and (b) PL spectrum of $FAPbI_3$ QDs (inset shows the photographs of $FAPbI_3$ QDs colloidal solution in the absence and presence of UV illumination). (c) Bandgap energy calculation by Tauc Plot method.

For calculating the bandgap energy of $FAPbI_3$ QDs, the Tauc plot method was used. The results showed that the bandgap energy of $FAPbI_3$ QDs was 1.68, as shown in Fig.3.3(c). It is worth mentioning that not only the bandgap energy of $FAPbI_3$ is closer to the infrared range, compared to methylammonium and cesium lead iodide, making this perovskite the most preferred and promising candidate for photovoltaic devices, but also is more moisture-resistant and phase-stable.

3.4. FTIR of $FAPbI_3$ QDs

Fig.3.4 depicts the results of FTIR spectroscopy for pure OA, OAm, and $FAPbI_3$ QDs. Also, all the specific peaks with their corresponding bonds and chemicals are listed in Table 3.2. In pure OA, the peak at 1725 cm^{-1} corresponds to a carboxylic acid group (R-COOH). The spectrum of OAm has a specific peak at 3300 cm^{-1} related to the amine group. In addition to these specific groups, there are three other intense peaks at 2885, 2919, and 2984 cm^{-1}, ascribed to CH_2 symmetric, CH_2 asymmetric, and CH_3 symmetric of both OA and OAm ligands, respectively. The presence of these three symmetric and asymmetric peaks in the spectrum of $FAPbI_3$ QDs confirms the existence of ligands [61]. As previously discussed, OA and OAm are transformed into oleate and octylammonium ligands during the synthesis, passivating the surface of $FAPbI_3$ QDs. Therefore, when OA changes to oleate, the peak at 1710 cm^{-1}, related to R-COOH, is significantly reduced, and other peaks at 1409 and 1530 cm^{-1}, related to COO^- symmetric and COO^- asymmetric, respectively, appear. Regarding OAm, the peak at 3300 cm^{-1}, ascribed to the amine group, is remarkably reduced.

Moreover, there are two other peaks at 1710 and 3357 cm^{-1}, corresponding to υ(C=N) and C=N-H_2^+ of FAI in $FAPbI_3$. This peak has been widely considered as a confirmation for $FAPbI_3$ perovskite formation.

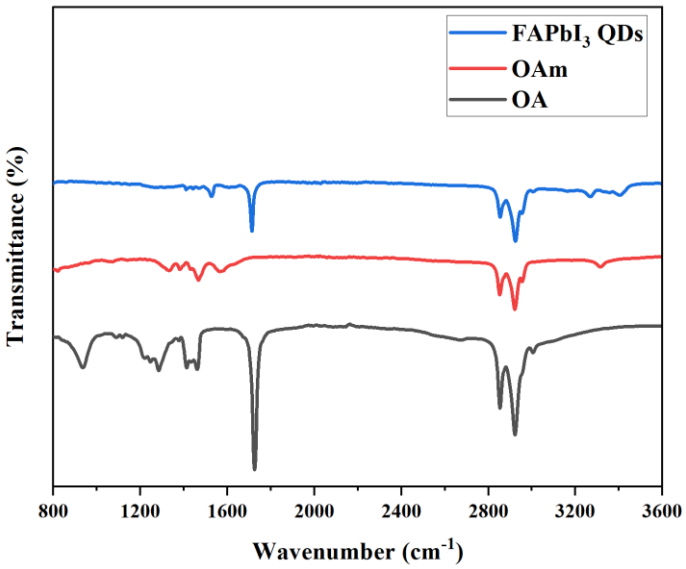

Figure 3.4. FTIR of pure OA, OAm, and $FAPbI_3$ QDs.

Table 3.2. The wavenumbers of intense FTIR peaks with their corresponding bonds.

Wavenumber (cm^{-1})	**Bond**	**Chemical**	**Pre. Or Abs.**
1409	R-COO^- symmetric	Oleate	Yes
1530	R-COO^- Asymmetric	Oleate	Yes
1717	υ(C=N)	FA^+ in $FAPbI_3$	Yes
1730	R-COOH	OA	Yes
2885	CH_2 Symmetric	OA, OAm	Yes
2984	CH_3 Symmetric	OA, OAm	Yes
2919	CH_2 Asymmetric	OA, OAm	Yes
3300	R-N-H	OAm	Yes
3170	N-H_3^+	FA^+	Close to this peak
3357	C=N-H_2^+	FAI	Yes
3500	R-N-H	FAI	Close to this peak

3.5. Optical Microscopy and Raman Spectroscopy of Transferred Graphene

In the next step, the CVD-grown graphene was transferred to the Si/SiO_2 substrate via the PMMA method. This process was fully described in the materials and methods section. Fig.3.5. shows the optical microscopy images and μ-Raman spectrum of the graphene transferred on the Si/SiO_2. According to the literature, the intensity and position of the graphene Raman peaks are highly dependent on defects and doping, impacting the surface phonon scattering of graphene and electronic properties. Graphene has three specific Raman peaks, including G, D, and 2D peaks. The G band at 1590 cm^{-1} corresponds to the high-frequency E_{2g} phonon at Γ point, representing a primary in-plane vibrational mode of the sp^2 hybridized lattice configuration. The peak located at 1350 cm^{-1} is named a D band, ascribed to the presence of asymmetry in the graphene lattice. The 2D peak located at 2680 cm^{-1} is also generated by a two-photon mode transition in the graphene lattice [62]. Although no peaks were detected when the laser was focused on the right side of the edge, showing the absence of the graphene, G and 2D peaks of graphene at 1350 and 2650 cm^{-1}, respectively, were detected when the laser was focused on the left side, confirming the presence of graphene. Regarding the crystallinity of the graphene, the intensity of the first-order D band is negligible, confirming the high crystal symmetry of graphene. To have a quantitative view of the defectivity level of the graphene, the proportion of the intensities of D to G bands (I_D/I_G) is calculated. The intensity of the D band is almost zero, showing the significantly low value of I_D/I_G, confirming the high crystallinity of monolayer graphene. Moreover, I_{2D}/I_G determines the number of graphene layers. In the case of

monolayer graphene, the I_{2D}/IG ratio is above 2. To calculate this parameter, either the ratio of intensities or the ratio of the area under the bands of 2D and G is considered. The calculated value was 2.8, confirming the presence of single-layer graphene. However, as seen in Fig.3.5(a, b), PMMA residuals (darker disconnected particles) are still on the surface even after acetone treatment.

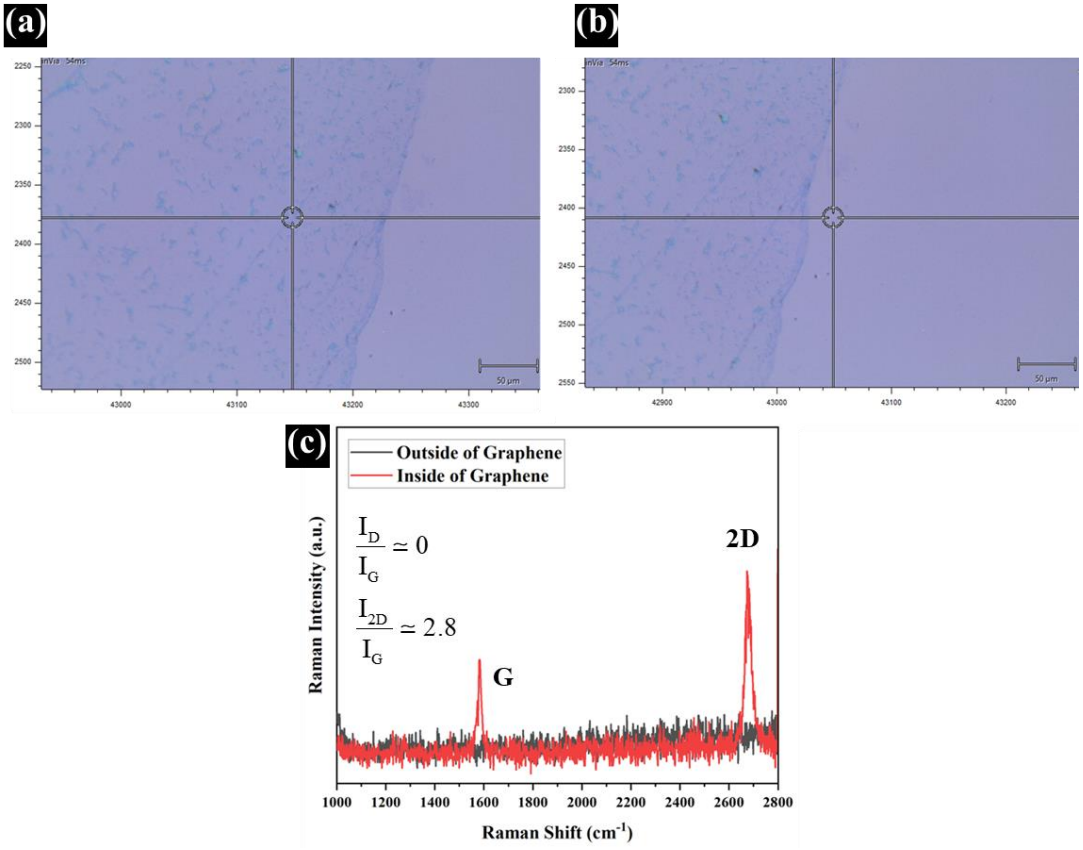

Figure 3.5. Optical microscopy of the (a) inside and (b) outside of graphene transferred on SiO_2 after acetone treatment with (c) corresponding Raman spectroscopy.

To reduce the concentration of the contaminations, various methods were used. It was revealed that after graphene transfer, annealing process, hot acetone, and overnight acetone treatment, some PMMA residuals remained untouched (Fig.3.6(a)). Therefore, various

polar solvents were tested with the same condition. Unexpectedly, none of them, including DMF, DMSO, chloroform, and chlorobenzene were found effective in the removal of contaminations. Regarding the last one with a high boiling point, the process was performed at 150 °C, however, no significant improvement was observed. The effect of UV light (287 nm and 365 nm) for 4 h as well as UV-ozone treatment for 30 min on contamination removal was also tested. Regarding the former, no remarkable change was observed, however, UV ozone treatment only removed the uncovered graphene, showing the incapability of these processes (Fig.3.6(b)). Surprisingly, the contamination played a protective role for the underneath graphene since the G band was detected and the D band was greatly intensified, indicating the adverse effect of UV-ozone treatment on the graphene.

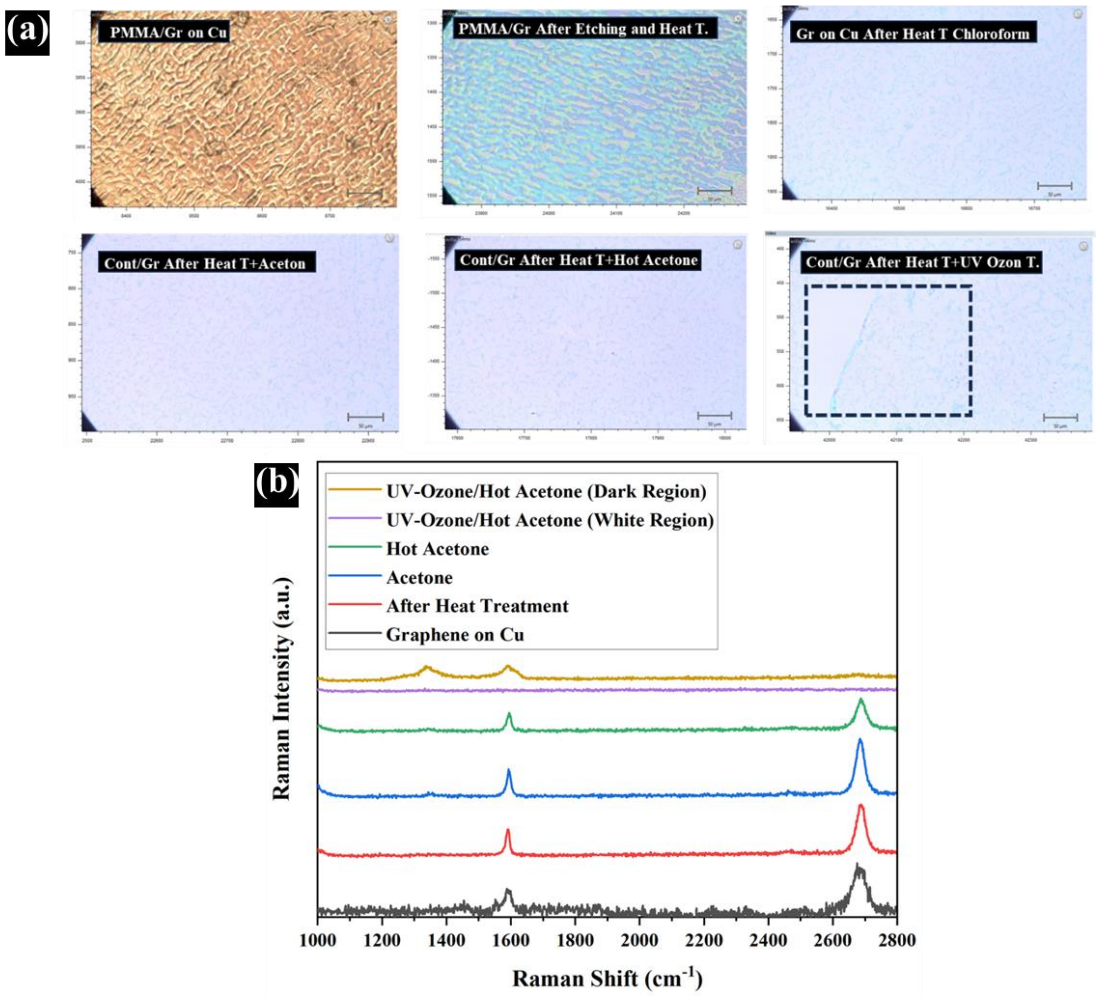

Figure 3.6. (a) Optical microscopy and (b) Raman spectroscopy of graphene transferred on SiO_2 via different modification methods.

One of the most effective ways to remove the PMMA residuals is heat treatment at high temperatures above 450 °C in the presence of H_2 or Ar gas. Using an inert gas mitigates the negative impact of O_2 on graphene oxidation or removal. Despite some articles [63], any temperature below 700 °C and above 950 °C was ineffective since the residuals remained intact and the graphene was fully removed, respectively. Finally, 850 °C was selected as the lowest and optimized temperature since the contaminations started to be removed.

Extending the annealing process from 6 to 14 h almost removed the surface contaminations on the surface of the graphene (Fig.3.7(a, b)). Based on the Raman spectrum in Fig.3.7(c), the intensity of the D band (or I_D/I_G) slightly increased, showing slight damage to the graphene crystal structure.

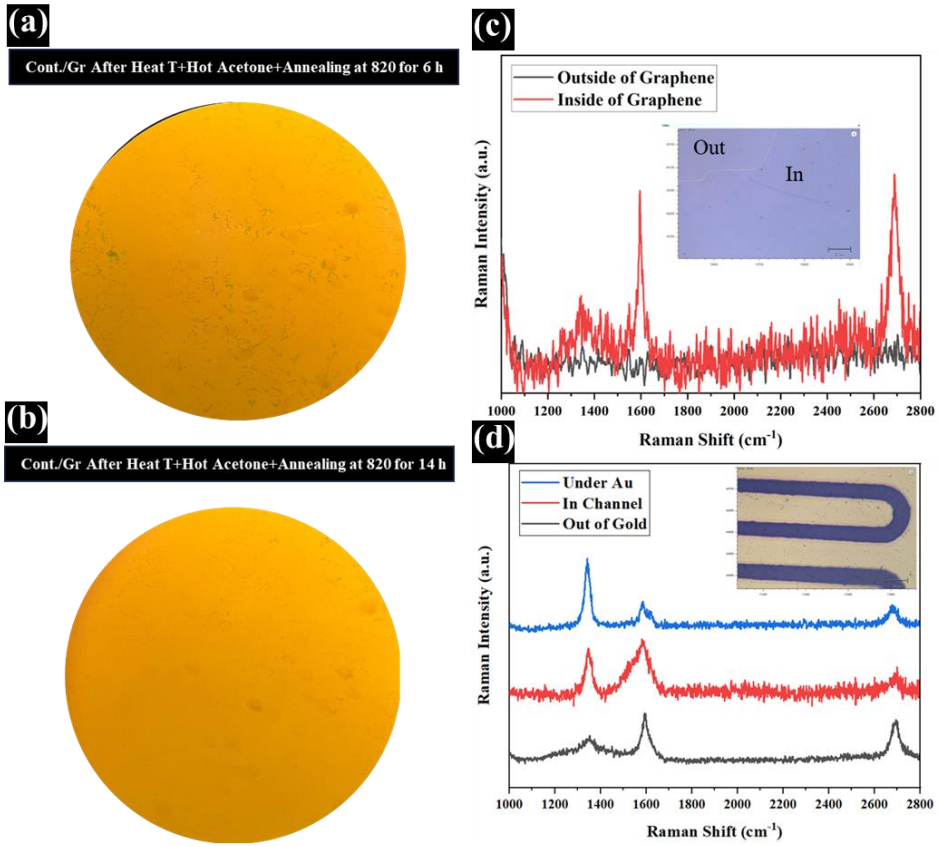

Figure 3.7. Optical microscopy of graphene transferred on SiO_2 after heat treatment at 850 °C for (a) 6 and (b) 14 h. (c) Raman spectroscopy of the process, carried out at 850 °C for 14 h. (d) Raman spectroscopy of graphene within the channel and under the gold electrodes.

As discussed before, to deposit the electrodes with the interdigitated structure on the surface of the Graphene/Si/SiO_2 substrate, sputtering was used. To mitigate the adverse effect of the collisions between graphene and target atoms, the deposition rate was set at 0.3 °A/s,

and after 200 °A, it increased to 0.7 °A/s. Despite deposition rate reduction, the I_D/I_G of in-channel graphene increased. This increment was more severe for the graphene located under gold electrodes (Fig.3.7(d)).

3.1. I-V Measurements

After the fabrication process, devices were measured in different conditions. To make sure there is no contact between the source and drain (the probability of short-circuit as a result of gold diffusion during sputtering), the voltage was swept between the source and drain of the $Si/SiO_2/Au$ device and the current was measured (Fig.3.8(a)). The source and drain are contactless since the current is in the range of nano ampere. By inserting graphene between the oxide layer and electrodes, the current between the source and drain linearly increased from -70 μA to ~70 μA by sweeping the V_{SD} between -0.01 V- 0.01 V (Fig.3.8(b)). To investigate the performance of graphene-based photodetectors, the I_{SD} of $Si/SiO_2/Graphene/Au$ device was measured in dark and blue light under V_{SD} between -0.01 V-0.01 V. Although some papers claimed that band bending between graphene and gold, due to the Fermi level difference, is capable of separating the photogenerated electron and holes in the vicinity of contact regions, no change between dark and light curves was observed in our study, demonstrating the incapability of graphene to be used as an active layer in photodetectors. The reason behind this observation is that graphene is zero bandgap semimetal, therefore, any photogenerated electrons and holes are swiftly recombined, failing to generate any current.

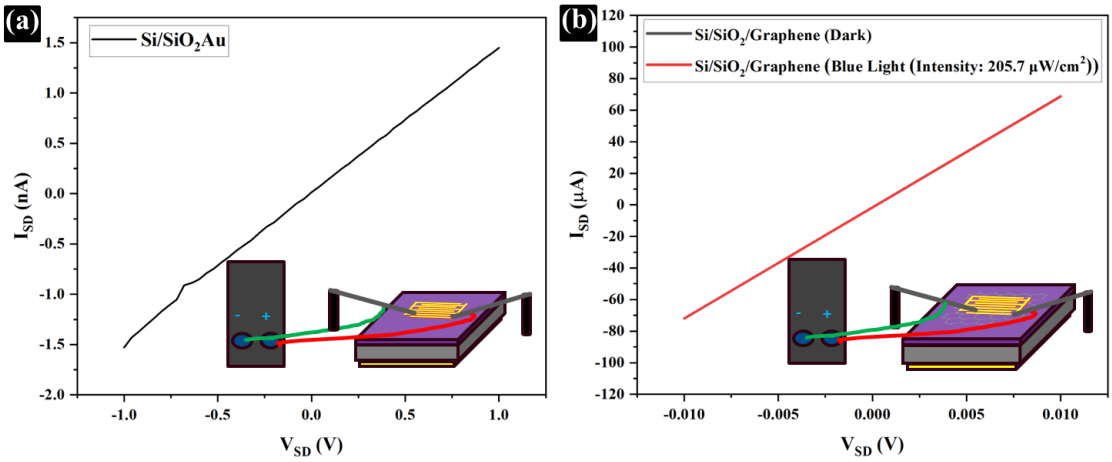

Figure 3.8. I-V curves of (a) Si/SiO_2/Cr-Au device and (b) Si/SiO_2/graphene/Cr-Au device in dark and under blue LED illumination.

3.1.1. Effect of QDs Deposition Method

To fabricate photodetectors, QDs were deposited on the interdigitated Si/SiO_2/Graphene/Cr-Au (with a channel length of 40 μm) via drop-casting, spin coating, and centrifugation. In the case of drop casting, the surface became brownish, showing a thick layer of QDs obtained, however, it remained greasy. Then, the corresponding device was measured in the absence and presence of a blue LED (Fig.3.9(a, b)). As seen in Fig.3.9(c), no significant difference between dark and blue light was observed. This is mainly because QDs are fully passivated with oleate and ammonium ligands that are insulators. Also, ligands increase the distance between the QDs, hindering the separation of photogenerated electrons and holes under illumination. In the case of spin coating, 50 μL of QD solution was dropped and spin-coated five times. However, the difference between dark and light currents was very small (Fig.3.9(d)). This might be related to the thin layer of QD, due to the presence of surface ligands which hinders further QD

deposition and charge separation, lessening the amount of photogenerated excitons.

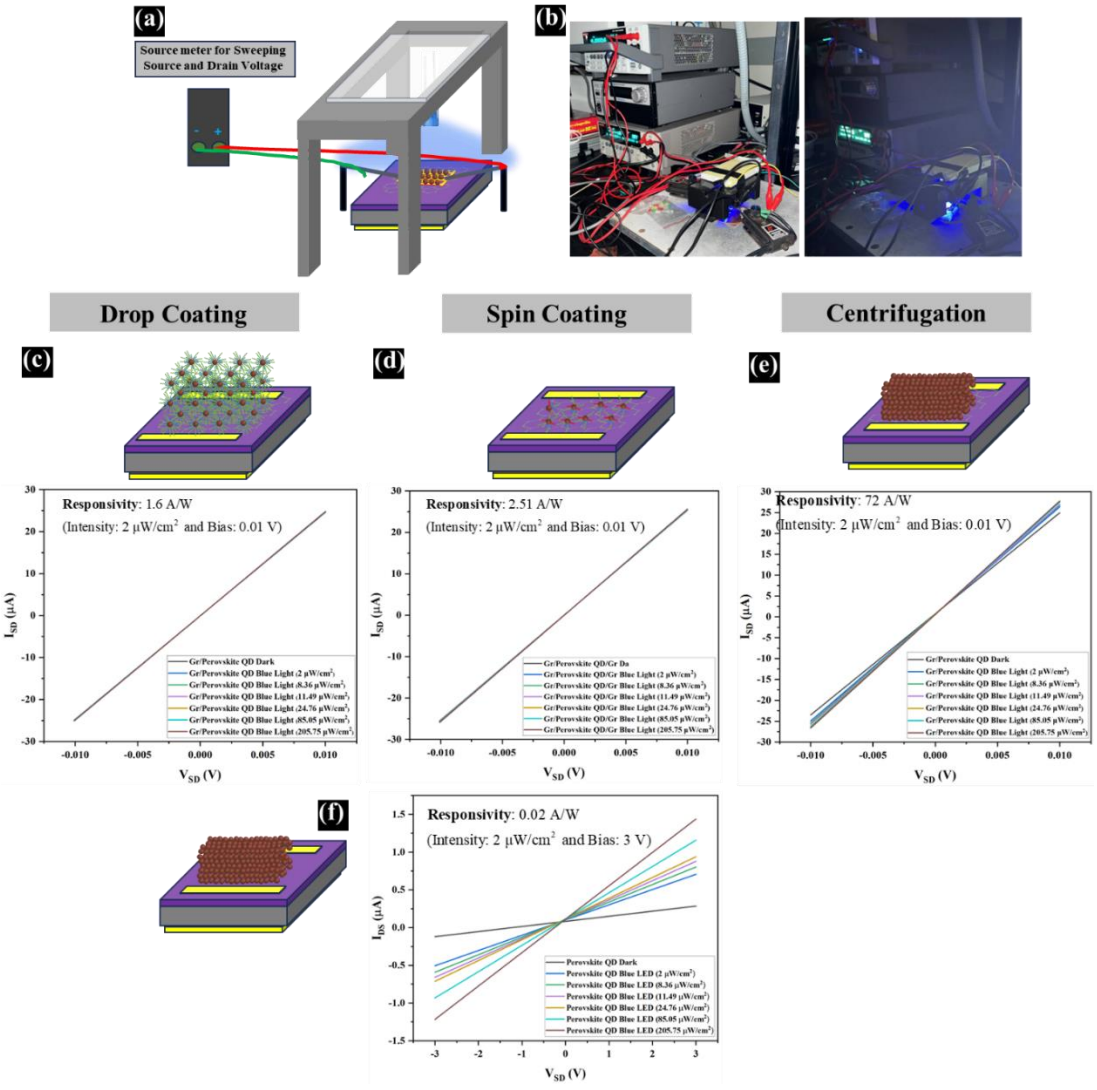

Figure 3.9. (a) Schematic diagram and (b) photographs of the configuration of blue LED, photodetector device, and source meter during measurement. Linear I-V curves of Si/SiO_2/graphene/QDs/Cr-Au prepared by (c) drop casting, (d) spin coating, and (e) centrifugation in dark and under blue LED illumination. (f) Linear I-V curves of Si/SiO_2/QDs/Cr-Au.

Compared to the abovementioned deposition methods, those devices prepared by

centrifugation showed the best results. As seen in Fig.3.9(e), there is a considerable difference between dark and photogenerated currents under V_{DS} between -0.01 V and 0.01 V. By increasing the intensity of the blue LED from 2 $\mu W/cm^2$ to 285.75 $\mu W/cm^2$, the photogenerated current enhanced. This device not only had a thicker layer than spin coating, but also a drier layer than drop casting. In the case of the QD devices without graphene, the dark current significantly decreased, however, by increasing the light intensity, the photogenerated current increased (Fig.3.9(f)). Without using graphene, photogenerated carriers are transferred from one QD to another QD, leading to conductivity reduction. Compared to all devices, this device had the lowest responsivity about 0.03 A/W, showing the great power of graphene in the performance enhancement of photodetectors.

3.1.2. Photoresponsivity

Photoresponsivity is one of the most important photodetector parameters, defined as follows:

$$R(\lambda)=\frac{J_{Ph}}{P_{Light}}(A/W) \qquad \text{(Equ.3.1)}$$

Where J_{Ph} and P_{Light} are photogenerated current density and input intensity of an LED.

It is obvious that the higher the current density, the higher the number of collected photogenerated carriers, showing higher responsivity. On one side, the photoresponsivity of QD devices fabricated by the centrifugation method (72 A/W) is remarkably higher than that of devices prepared by spin coating (2.51 A/W) and drop casting (1.6 A/W). This shows the great power of the centrifugation method in preparing not only a thicker but also a drier layer. Therefore, this process makes a more closed-packed film, resulting in the

performance enhancement of QD devices. On the other side, as seen in Fig.3.10(a), the responsivity of the device has a downward trend with the increment of light intensity, therefore, the maximum responsivity of the device was obtained at the light intensity of 2 $\mu W/cm^2$, related to the trapped carriers' lifetime in $FAPbI_3$ QDs. This trend in photoresponsivity can be explained as follows. The following equation shows the relation between $\tau_{lifetime}$ (carrier lifetime) under different light intensities:

$$\tau_{lifetime} = \frac{\Delta n}{\mu} = \frac{1}{\gamma(n_\circ + p_\circ + \Delta n)} \qquad \text{(Equ.3.2)}$$

Δn, μ, γ, n_0, and P_0 are the concentration of photoexcited carriers in QDs, the net recombination rate, the average values of probabilities of electron and hole recombination with different thermal velocities, dark electrons concentration, and dark hole concentration, respectively. When the incident light power is low, Equ.3.2 could be written as follows:

$$\tau_{lifetime} \approx \frac{1}{\gamma(n_\circ + p_\circ)} \qquad \text{(Equ.3.3)}$$

In contrast, when the incident light power is remarkably high, the equation is simplified as follows:

$$\tau_{lifetime} \approx \frac{1}{\gamma(\Delta n)} \qquad \text{(Equ.3.4)}$$

Regarding equ.3.3, the electron and hole concentrations in the dark are too low, and therefore, carrier lifetime is remarkable. In contrast, increasing the power of incident light leads to a higher photoexcited carrier concentration, which enhances the recombination rate of photoexcited carriers and shortens the lifetime of trapped holes. In other words, $\tau_{lifetime}$ is higher when the incident light power is lower due to the gradually filled trap states while

all the trap states are fully filled and the excess photogenerated carriers are no longer trapped at high optical powers, resulting in average carrier lifetime reduction [54]. Therefore, the photoresponsivity of photodetectors decreases with increasing the light intensity.

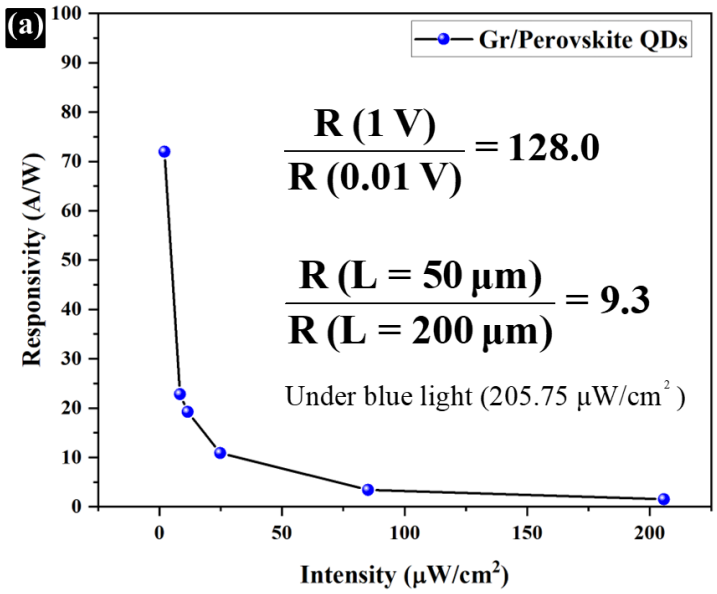

Figure 3.10. (a) Responsivity of Cr-Au/Si/SiO_2/graphene/QDs/Cr-Au device under blue light with different optical powers.

In addition, the carrier transit time ($\tau_{transit}$) is related to the length of the channel and source-drain voltage (V_{DS}):

$$\tau_{transit} = \frac{L}{\nu_{Drift}} = \frac{L}{\mu_{\circ} \times \varepsilon} = \frac{L^2}{\mu_{\circ} \times V_{DS}} \qquad \text{(Equ.3.5)}$$

Where υ_{Drift}, ε, L, and μ_0 are electron velocity, electric field, channel length, and graphene mobility, respectively. As seen in the inset of Fig.3.10(a), the photoresponsivity of the same device under blue LED (light intensity= 205.75 µW/cm^2) at V_{DS}= 1 V is 128 times higher than that of the sample with V_{DS} of 0.01 V. This corresponds to the $\tau_{transit}$ reduction as a

result of the increment of V_{DS}. In addition, by increasing the channel length from 50 μm to 200 μm, the responsivity is reduced from 1.52 A/W to 0.16 A/W due to the increase in transit time, inducing the recombination.

3.1.1. Response Time

To find the rising and falling response times as well as the current stability of the device, on/off cycles at V_{SD}=0.01 V under blue LED illumination (LED intensity: 257.57 μW) were applied for 250 s. The rising response time is defined as the interval during which the transient current density increases from 10% to 90% of its maximum value. In contrast, the falling response time is the interval during which the transient current density decreases from 90% to 10% of its maximum value. Fig.3.11(a, b, c) show I−t responses of the graphene/QD photodetector device. The device exhibits stable photoswitching responses during on-and-off cycles with no significant quenching of the photogenerated currents over a period of 250 seconds. The rising (t_{rising}) and falling ($t_{falling1}$ and $t_{falling2}$) response times of QDs are 530 ms and 5.65 s, respectively [67].

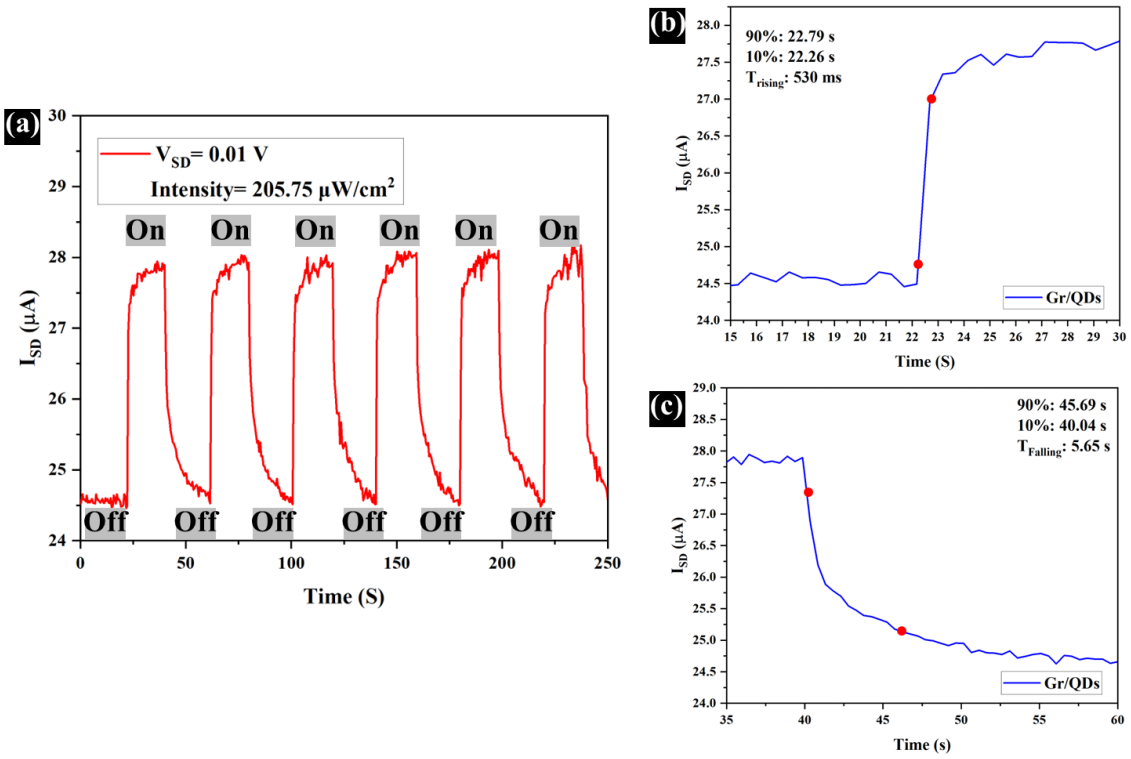

Figure 3.11. (a) I-t (or on-off) curves of Cr-Au/Si/SiO_2/graphene/QDs/Cr-Au device in dark and under red LED illumination. (b) Rising part of the I-t curve. (c) Falling part of the I-t curve.

3.1.2. Effect of LEDs

In the previous results, the bandgap energy (E_g) of $FAPbI_3$ QDs was calculated at 1.68 eV. In terms of theoretical concepts, $FAPbI_3$ QDs are capable of absorbing photons with energy (wavelength) higher than 1.68 eV (738 nm). Therefore, QDs can be used as a photodetector for UV-visible light. To find out the performance of graphene/QD photodetector devices under various LEDs, I-V curves and photoresponsivity of QD photodetectors under 700 nm, 580 nm, 520 nm, 470 nm, and 365 nm LEDs were measured.

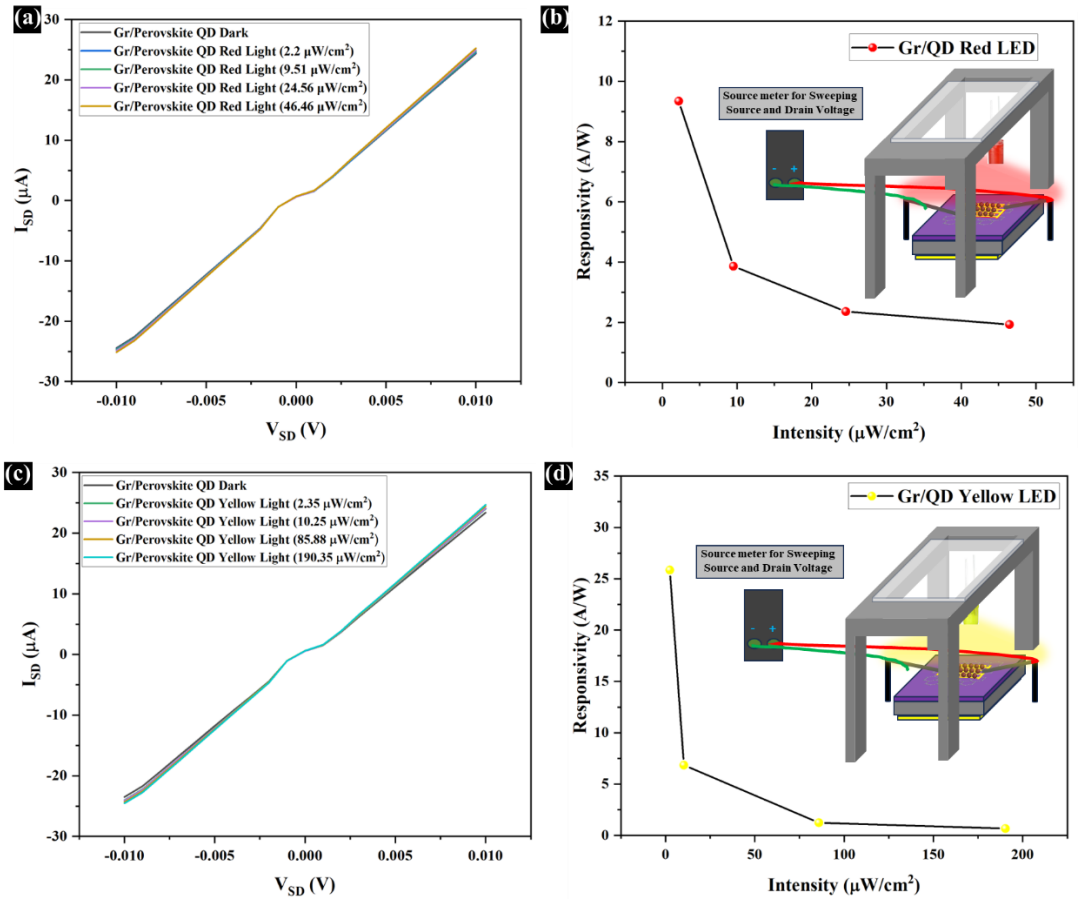

Figure 3.12. (a) I-V curves and (b) responsivity of Cr-Au/Si/SiO_2/graphene/QDs/Cr-Au device in dark and under (a, b) red and (c, d) yellow LED illumination (inset shows the schematic diagram of the configuration of red LED, photodetector device, and source meter during measurement).

As seen in Fig.3.12(a, b), by increasing the intensity of the red LED, the photocurrent increases while the responsivity decreases. At V_{DS}= 0.01 V and optical power of 2.2 μW/cm^2, the maximum responsivity was calculated to be 9.34 A/W. The reason behind this improvement is attributed to the higher energy of red photons (1.77 eV) than the E_g of QDs (1.68 eV), enabling the excitation of electrons [68]. Regarding the yellow LED in Fig.3.12(c, d), I-V curves and photoresponsivity show the same trend, however, the

responsivity at V_{SD}= 0.01 V was calculated at 25.84 A/W, which is higher than that of the red LED. This is related to the higher energy of the yellow LED (2.13 eV) than that of the red LED, increasing the number of photogenerated electrons and holes.

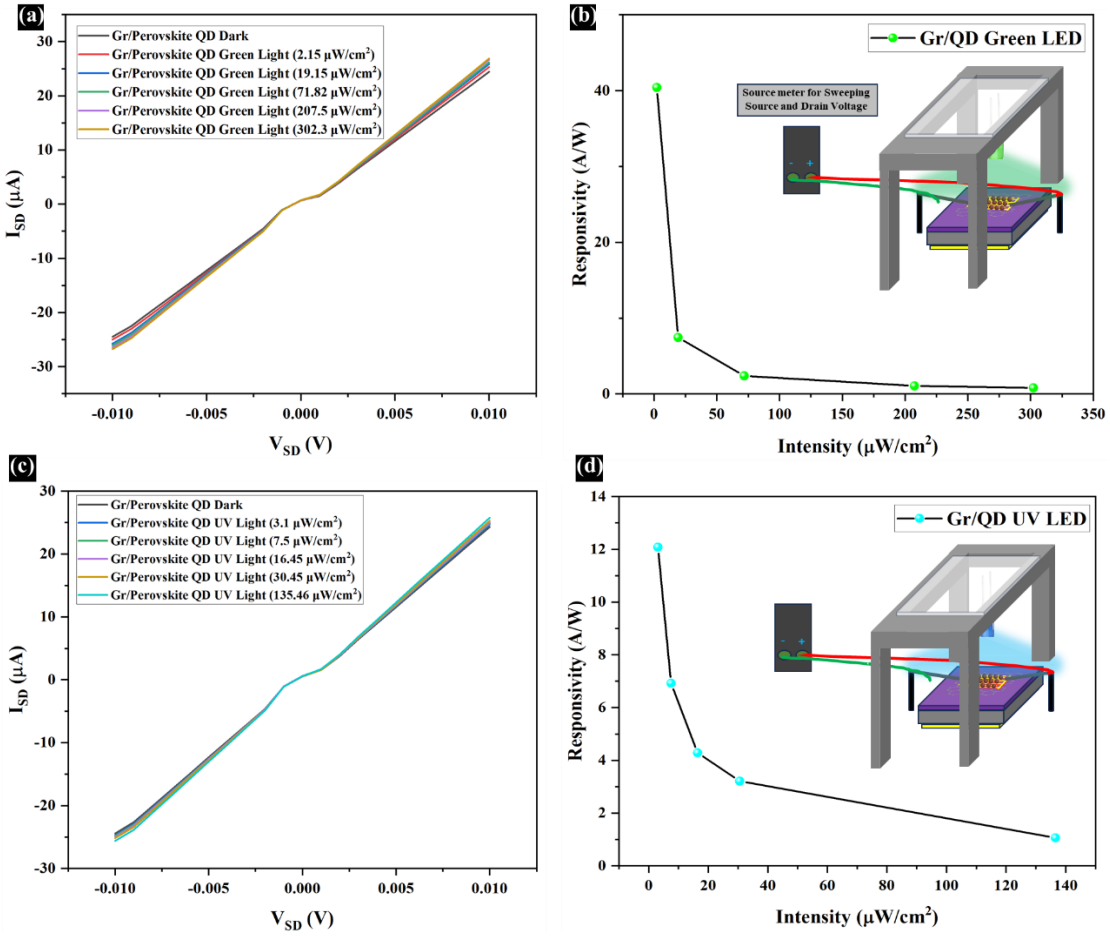

Figure 3.13. (a) I-V curves and (b) responsivity of Cr-Au/Si/SiO_2/graphene/QDs/Cr-Au device in dark and under (a, b) green and (c, d) UV LED illumination (inset shows the schematic diagram of the configuration of green LED, photodetector device, and source meter during measurement).

As seen in Fig.3.13(a,b), the I-V curves and photoresponsivity of the green LED showed the same trend as that of yellow and red LEDs. However, it exhibited a higher responsivity (40.41 A/W) at V_{DS}= 0.01 V than that of red and yellow LEDs due to the higher energy of

green LED (2.24 eV). As shown before, the highest responsivity was achieved by the blue LED at 72 A/W. However, as seen in Fig.3.13(c, d), the performance of the photodetector device decreases by using the UV LED. Although UV LED is capable of exciting more photogenerated carriers, a main part of the light energy is lost due to the thermalization of carriers.

3.1.3. Effect of Gate Voltage

Gate-dependent graphene transistors have engaged considerable attention [69]. These graphene transistors can be either back-gate or top-gate. Fig.3.14(a, b) shows how positive and negative gate/source voltage changes the source/drain current. In graphene, it is assumed that the conduction band and valence band meet each other at a point, called Dirac point, and the valence states are occupied with electrons and the conduction band is free of electrons in the absence of gate voltage. Therefore, the gate-free graphene transistor has the lowest current or highest resistivity at this point. Applying negative gate voltage induces positive charges to be piled up at the SiO_2 surface, making graphene p-doped. This leads to the enhancement of channel conductivity due to the presence of free carriers. In contrast, when the positive gate voltage is applied, the holes are piled up on the backside of SiO_2 and negative charges are accumulated at the SiO_2 surface, making the graphene n-type. This contributed to the improvement of channel conductivity due to the presence of free carriers. However, the transferred graphene is p-doped in most cases, meaning that there are many holes in the valence band at $V_{GS}=0$. Therefore, high values of positive gate voltages should be applied to reach the Dirac point.

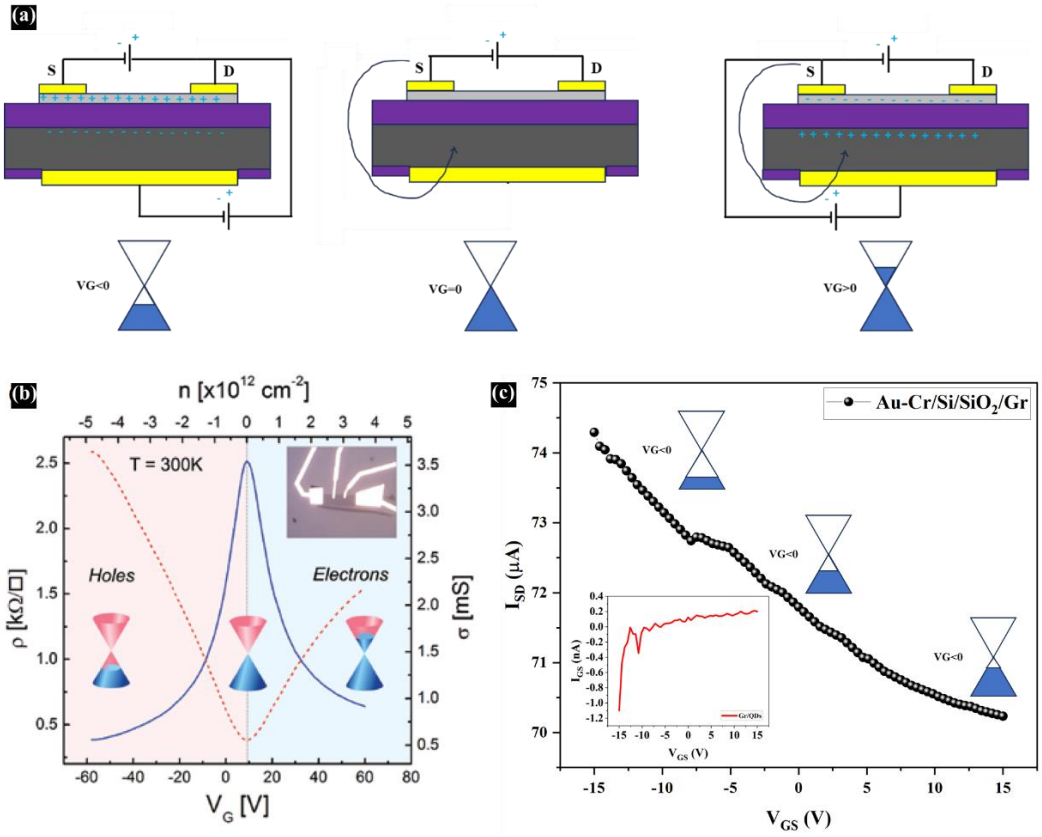

Figure 3.14. (a) The effect of gate voltage on the energy band diagram of graphene. (b) The relation between the conductivity of the device and back V_G [70]. (c) I_{DS} versus V_G for Cr-Au/Si/SiO_2/graphene/Cr-Au photodetector.

As seen in Fig.3.14(c), by sweeping the gate voltage between -15 V- 0 V at the constant V_{DS}=0.01 V, the I_{SD} decreased from 74.5 μA to 71.6 μA. In this V_{GS} interval, the current between the source and gate is in the range of pA or nA, demonstrating the oxide layer prevents current leakage. By further applying the gate voltage from 0 V to 15 V, the downward trend continued without reaching the Dirac point. This is common in some back-gate graphene photodetectors where the Dirac point appeared between 20-45 V, due to the presence of contaminations, making the graphene highly p-doped [71]. When the gate

voltage increased to 20 V, the sample was broken down which hindered applying higher voltages.

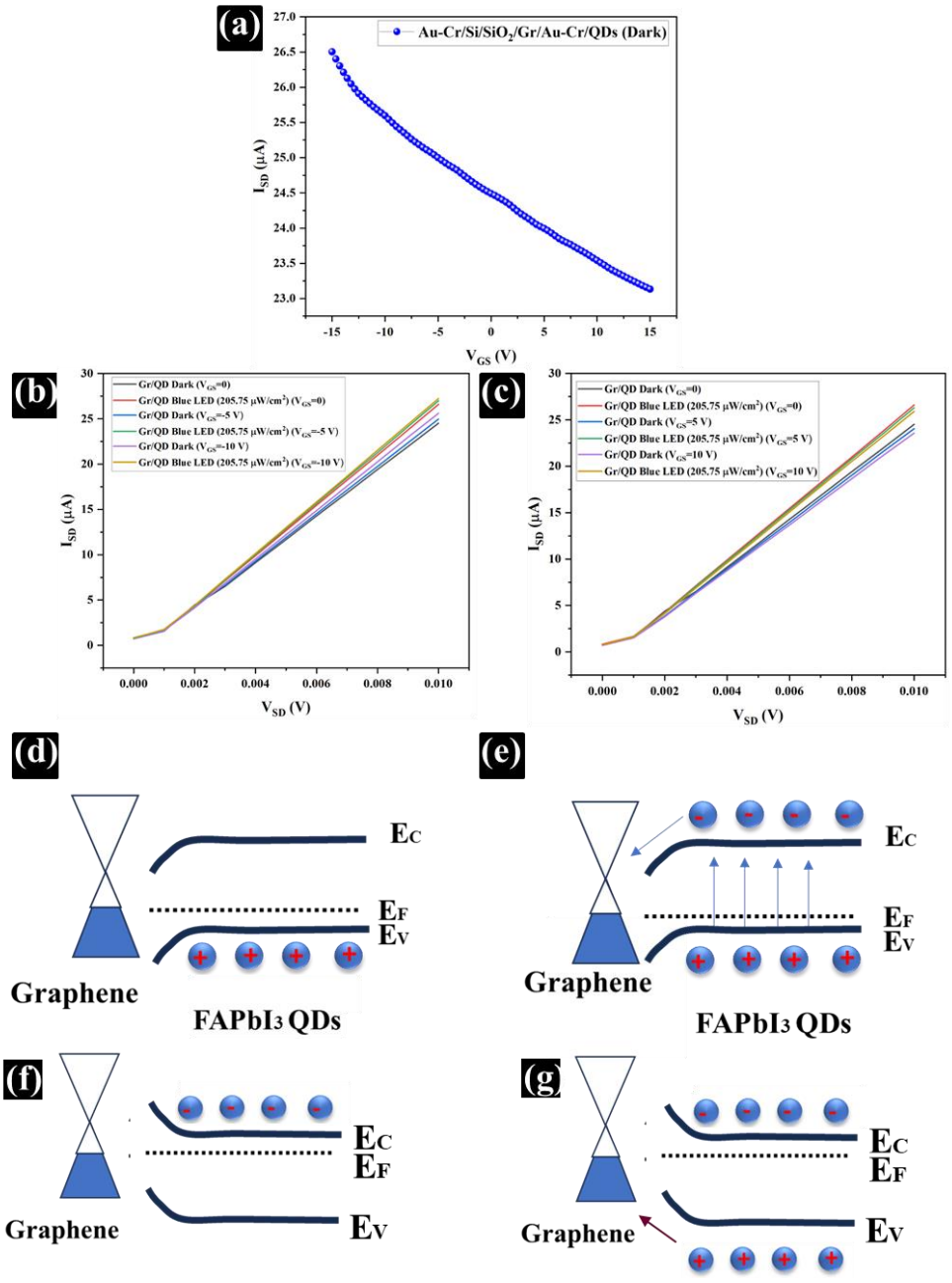

Figure 3.15. (a) I_{DS}-V_{GS} of Cr-Au/Si/SiO_2/graphene/QD/Cr-Au photodetector in dark condition. I-V curves of Cr-Au/Si/SiO_2/graphene/QD/Cr-Au photodetectors under (b) negative and (c) positive

gate voltages. Energy band diagram of graphene/QD in dark (d, f) and under light (e, g). Energy band diagrams of graphene/QD when the Dirac point is (d, e) higher or (f, g) lower than that of bare graphene.

After centrifuging the QDs on the surface of the device, the pattern remained the same but I_{DS} values decreased at the whole V_{GS} interval of -15 V- 15 V (Fig.3.15(a)). I_{DS} versus V_{DS} for different values of gate voltages was also sketched in (Fig.3.15(b, c)). The higher the negative gate voltage, the higher the dark and light I_{SD}. In contrast, the higher the positive gate voltage, the lower the dark and light I_{SD}. This corresponds to the fact that while the channel is p-doped in all gate voltages, the negative (positive) V_{GS} makes the channel more (less) p-doped, increasing (decreasing) the conductivity of the channel. Moreover, the Dirac point shift is one of the most important factors revealing band bending between QDs and graphene. As the Dirac point was not found in my measurements, it is hard to have a correct and precise interpretation, however, we can represent two scenarios.

Firstly, I calculated the slope of the curves between the gate voltage of -14 V- 15 V. Comparing the I_{SD}/V_{GS} curves of the graphene and graphene/QD in dark condition, the former has a lower slope than that of the latter. This may show that adding QDs is shifting the Dirac point to the higher gate voltages, making the graphene more p-doped, due to the transferring of holes from the QDs to the graphene. This leads to a downward bending of the QDs CB and VB, forming a barrier against the holes, and hindering further holes transferring (Fig.3.13(d)). As seen in Fig.3.13(e), photogenerated electrons are transferred to the graphene, and holes are trapped due to the barrier.

In the second scenario, since graphene is highly p-doped, it is assumed that electrons are

transferred from QDs to graphene, making graphene less p-doped and shifting the Dirac point to lower gate voltages. This leads to an upward bending of the QDs CB and VB, forming a barrier against the electrons, and hindering further holes transferring (Fig.3.13(f)). As seen in Fig.3.13(g), photogenerated holes are transferred to the graphene, and electrons are trapped due to the barrier.

All the results represented in this section show that graphene/$FAPbI_3$ QDs can be introduced as an efficient candidate for the next generation of UV-visible photodetectors.

4. Chapter 4: Conclusion and Future work

By taking advantage of graphene and perovskite $FAPbI_3$ QDs, an efficient photodetector was fabricated, responding to a wide spectrum of light from UV to red. In the case of the latter, the ligand-assisted reprecipitation process was used to synthesize QDs at room temperature by injecting the precursors' solution into an anti-solvent. OA and OAm were capable of solving the perovskite precursors in non-coordinating ACN/GBL solvent, controlling the size of QDs, and passivating the surface atoms of QDs. As a result, the alpha phase of $FAPbI_3$ QDs with impressive optical properties was formed, confirmed by detecting the characteristic XRD peaks and measuring d-spacing in HRTEM. The emission peak of QDs at 751 nm also verified the formation of the alpha phase and the strong confinement regime. In terms of the former, the graphene was successfully transferred to the Si/SiO_2 substrate by using the PMMA method. To remove a great volume of the contaminations without inducing considerable crystal disorder in graphene, annealing treatment was performed after heat treatment at 850 °C for 14 h. Following the electrode deposition with an interdigitated design, QDs were deposited onto the device using drop casting, spin coating, and centrifugation. Compared to the first two methods, the centrifugation method was capable of forming a more close-packed, thicker film, achieving the highest value of responsivity at 72 A/W, under blue LED illumination at a light intensity of ~2 $\mu W/cm^2$ and V_{SD} of 0.01 V. This responsivity is also significantly higher than that of the $FAPbI_3$ QD photodetector without graphene, which responded to a range of LEDs (UV, green, yellow, and red). While the former is attributed to the facilitation of carrier transferring by graphene, the latter is related to the low bandgap energy of QDs (1.68 eV),

absorbing whole wavelengths higher than 738 nm. In addition, the device exhibited rising (t_{rising}) and falling ($t_{falling}$) response times of 530 ms and 5.65 s, respectively. These outstanding results introduce the graphene/QD layers as a promising candidate for the next generation of photodetectors.

The research on 2D materials/QD photodetectors has been gaining remarkable attention. Since the dark current of semimetal graphene transistors is high, using other 2Ds like WS_2 and MoS_2 is more interesting due to the higher bandgap energy and lower dark current. Using the monolayer of WS_2 and MoS_2 can significantly decrease the dark current, however, provides the device with a path for improving the photogenerated carriers transferring. In addition to the above, utilizing bilayers and nanoribbons of graphene can also be an effective way to reduce the conductivity of the dark current.

QDs are also passivated with long insulating ligands. The effect of the long ligands is like a double-edged sword. On one side, these ligands are insulators, decreasing the conductivity of the QD layer and playing as a barrier against layer thickening. On the other side, they passivate the surface dangling bonds as non-radiative recombination centers, increasing the performance of the device. To solve this problem, short ligands should be replaced with long ligands to not only passivate the surface atoms but also reduce the distance between the QDs, leading to conductivity enhancement of the QD layer.

Using precise and accurate optical power meters, capable of detecting lower intensities of light in the range of nW and pW is highly recommended. The optical power used in this study was relatively inaccurate in lower light intensities. To decrease the channel length,

photolithography or electron beam lithography can also be used, enhancing the performance of the device.

5. References

[1] J. Dai, J. Xi, L. Li, J. Zhao, Y. Shi, W. Zhang, C. Ran, B. Jiao, X. Hou, X. Duan, Z. Wu, Charge Transport between Coupling Colloidal Perovskite Quantum Dots Assisted by Functional Conjugated Ligands, Angew. Chemie Int. Ed. 57 (2018) 5754–5758. https://doi.org/10.1002/anie.201801780.

[2] Z. Shi, Y. Li, Y. Zhang, Y. Chen, X. Li, D. Wu, T. Xu, C. Shan, G. Du, High-efficiency and air-stable perovskite quantum dots light-emitting diodes with an all-inorganic heterostructure, Nano Lett. 17 (2017) 313–321. https://doi.org/10.1021/acs.nanolett.6b04116.

[3] Q. Zhang, S.T. Ha, X. Liu, T.C. Sum, Q. Xiong, Room-Temperature Near-Infrared High-Q Perovskite Whispering-Gallery Planar Nanolasers, Nano Lett. 14 (2014) 5995–6001. https://doi.org/10.1021/nl503057g.

[4] W.L. Hong, Y.C. Huang, C.Y. Chang, Z.C. Zhang, H.R. Tsai, N.Y. Chang, Y.C. Chao, Efficient Low-Temperature Solution-Processed Lead-Free Perovskite Infrared Light-Emitting Diodes, Adv. Mater. 28 (2016) 8029–8036. https://doi.org/10.1002/adma.201601024.

[5] K. Wu, G. Liang, Q. Shang, Y. Ren, D. Kong, T. Lian, Ultrafast Interfacial Electron and Hole Transfer from CsPbBr 3 Perovskite Quantum Dots, J. Am. Chem. Soc. 137 (2015) 12792–12795. https://doi.org/10.1021/jacs.5b08520.

[6] S. Yakunin, L. Protesescu, F. Krieg, M.I. Bodnarchuk, G. Nedelcu, M. Humer, G. De Luca, M. Fiebig, W. Heiss, M. V. Kovalenko, Low-threshold amplified spontaneous emission and lasing from colloidal nanocrystals of caesium lead halide

perovskites, Nat. Commun. 6 (2015). https://doi.org/10.1038/ncomms9056.

[7] S. Rhee, K. An, K.T. Kang, Recent advances and challenges in halide perovskite crystals in optoelectronic devices from solar cells to other applications, Crystals. 11 (2021) 1–28. https://doi.org/10.3390/cryst11010039.

[8] S. Tao, I. Schmidt, G. Brocks, J. Jiang, I. Tranca, K. Meerholz, S. Olthof, Absolute energy level positions in tin- and lead-based halide perovskites, Nat. Commun. 10 (2019). https://doi.org/10.1038/s41467-019-10468-7.

[9] A. Kojima, K. Teshima, Y. Shirai, T. Miyasaka, Organometal halide perovskites as visible-light sensitizers for photovoltaic cells, J. Am. Chem. Soc. 131 (2009) 6050–6051. https://doi.org/10.1021/ja809598r.

[10] X. Luo, X. Liu, X. Lin, T. Wu, Y. Wang, Q. Han, Y. Wu, H. Segawa, L. Han, Recent Advances of Inverted Perovskite Solar Cells, ACS Energy Lett. 9 (2024) 1487–1506. https://doi.org/10.1021/acsenergylett.4c00140.

[11] L. Zhang, L. Mei, K. Wang, Y. Lv, S. Zhang, Y. Lian, X. Liu, Z. Ma, G. Xiao, Q. Liu, S. Zhai, S. Zhang, G. Liu, L. Yuan, B. Guo, Z. Chen, K. Wei, A. Liu, S. Yue, G. Niu, X. Pan, J. Sun, Y. Hua, W.Q. Wu, D. Di, B. Zhao, J. Tian, Z. Wang, Y. Yang, L. Chu, M. Yuan, H. Zeng, H.L. Yip, K. Yan, W. Xu, L. Zhu, W. Zhang, G. Xing, F. Gao, L. Ding, Advances in the Application of Perovskite Materials, Springer Nature Singapore, 2023. https://doi.org/10.1007/s40820-023-01140-3.

[12] Y. Fan, H. Meng, L. Wang, S. Pang, Review of Stability Enhancement for Formamidinium-Based Perovskites, Sol. RRL. 3 (2019) 1900215. https://doi.org/10.1002/solr.201900215.

[13] F. Ma, J. Li, W. Li, N. Lin, L. Wang, J. Qiao, Stable α/δ phase junction of formamidinium lead iodide perovskites for enhanced near-infrared emission, Chem. Sci. 8 (2016) 800–805. https://doi.org/10.1039/c6sc03542f.

[14] P. Raval, R.M. Kennard, E.S. Vasileiadou, C.J. Dahlman, I. Spanopoulos, M.L. Chabinyc, M. Kanatzidis, G.N. Manjunatha Reddy, Understanding Instability in Formamidinium Lead Halide Perovskites: Kinetics of Transformative Reactions at Grain and Subgrain Boundaries, ACS Energy Lett. 7 (2022) 1534–1543. https://doi.org/10.1021/acsenergylett.2c00140.

[15] O.J. Weber, B. Charles, M.T. Weller, Phase behaviour and composition in the formamidinium-methylammonium hybrid lead iodide perovskite solid solution, J. Mater. Chem. A. 4 (2016) 15375–15382. https://doi.org/10.1039/c6ta06607k.

[16] J.B. Rivest, L.-K. Fong, P.K. Jain, M.F. Toney, A.P. Alivisatos, Size Dependence of a Temperature-Induced Solid–Solid Phase Transition in Copper(I) Sulfide, J. Phys. Chem. Lett. 2 (2011) 2402–2406. https://doi.org/10.1021/jz2010144.

[17] J. Xue, J.W. Lee, Z. Dai, R. Wang, S. Nuryyeva, M.E. Liao, S.Y. Chang, L. Meng, D. Meng, P. Sun, O. Lin, M.S. Goorsky, Y. Yang, Surface Ligand Management for Stable FAPbI3 Perovskite Quantum Dot Solar Cells, Joule. 2 (2018) 1866–1878. https://doi.org/10.1016/j.joule.2018.07.018.

[18] X. Fan, W. Peng, Y. Li, X. Li, S. Wang, G. Zhang, F. Zhang, Deoxygenation of Exfoliated Graphite Oxide under Alkaline Conditions: A Green Route to Graphene Preparation, Adv. Mater. 20 (2008) 4490–4493. https://doi.org/10.1002/adma.200801306.

[19] B. Mahto, B. Mahanty, S. Hait, S. Hussain, A review of coal-based carbon and graphene quantum dots: synthesis, properties, and applications, Mater. Sci. Eng. B. 304 (2024) 117386. https://doi.org/10.1016/j.mseb.2024.117386.

[20] M.P. Levendorf, C. Kim, L. Brown, P.Y. Huang, R.W. Havener, D.A. Muller, J. Park, for Atomically Thin Circuitry, Nature. 488 (2012) 627–632. https://doi.org/10.1038/nature11408.

[21] Y. Ding, P. He, S. Li, B. Chang, S. Zhang, Z. Wang, J. Chen, J. Yu, S. Wu, H. Zeng, L. Tao, Efficient Full-Color Boron Nitride Quantum Dots for Thermostable Flexible Displays, ACS Nano. 15 (2021) 14610–14617. https://doi.org/10.1021/acsnano.1c04321.

[22] J. Zhou, J. Cui, S. Du, Z. Zhao, J. Guo, S. Li, W. Zhang, N. Liu, X. Li, Q. Bai, Y. Guo, S. Mi, Z. Cheng, L. He, J.C. Nie, Y. Yang, R. Dou, A natural indirect-to-direct band gap transition in artificially fabricated MoS2 and MoSe2 flowers, Nanoscale. 15 (2023) 7792–7802. https://doi.org/10.1039/d3nr00477e.

[23] J. V. Milić, J.H. Im, D.J. Kubicki, A. Ummadisingu, J.Y. Seo, Y. Li, M.A. Ruiz-Preciado, M.I. Dar, S.M. Zakeeruddin, L. Emsley, M. Grätzel, Supramolecular Engineering for Formamidinium-Based Layered 2D Perovskite Solar Cells: Structural Complexity and Dynamics Revealed by Solid-State NMR Spectroscopy, Adv. Energy Mater. 9 (2019) 1–12. https://doi.org/10.1002/aenm.201900284.

[24] H. Zheng, G. Liu, L. Zhu, J. Ye, X. Zhang, A. Alsaedi, T. Hayat, X. Pan, S. Dai, The Effect of Hydrophobicity of Ammonium Salts on Stability of Quasi-2D Perovskite Materials in Moist Condition, Adv. Energy Mater. 8 (2018) 1800051.

https://doi.org/10.1002/aenm.201800051.

[25] L.K. Ono, S. Wang, Y. Kato, S.R. Raga, Y. Qi, Fabrication of semi-transparent perovskite films with centimeter-scale superior uniformity by the hybrid deposition method, Energy Environ. Sci. 7 (2014) 3989–3993. https://doi.org/10.1039/c4ee02539c.

[26] F. Jiang, J. Xiong, W. Zhou, C. Liu, L. Wang, F. Zhao, H. Liu, J. Xu, Use of organic solvent-assisted exfoliated MoS2 for optimizing the thermoelectric performance of flexible PEDOT:PSS thin films, J. Mater. Chem. A. 4 (2016) 5265–5273. https://doi.org/10.1039/c6ta00305b.

[27] L. Protesescu, S. Yakunin, O. Nazarenko, D.N. Dirin, M. V. Kovalenko, Low-Cost Synthesis of Highly Luminescent Colloidal Lead Halide Perovskite Nanocrystals by Wet Ball Milling, ACS Appl. Nano Mater. 1 (2018) 1300–1308. https://doi.org/10.1021/acsanm.8b00038.

[28] M.C. Weidman, M. Seitz, S.D. Stranks, W.A. Tisdale, Highly Tunable Colloidal Perovskite Nanoplatelets through Variable Cation, Metal, and Halide Composition, ACS Nano. 10 (2016) 7830–7839. https://doi.org/10.1021/acsnano.6b03496.

[29] M. Yuan, L.N. Quan, R. Comin, G. Walters, R. Sabatini, O. Voznyy, S. Hoogland, Y. Zhao, E.M. Beauregard, P. Kanjanaboos, Z. Lu, D.H. Kim, E.H. Sargent, Perovskite energy funnels for efficient light-emitting diodes, Nat. Nanotechnol. 11 (2016) 872–877. https://doi.org/10.1038/nnano.2016.110.

[30] H. Zhu, Y. Fu, F. Meng, X. Wu, Z. Gong, Q. Ding, M. V. Gustafsson, M.T. Trinh, S. Jin, X.Y. Zhu, Lead halide perovskite nanowire lasers with low lasing thresholds

and high quality factors, Nat. Mater. 14 (2015) 636–642. https://doi.org/10.1038/nmat4271.

[31] Y. Fu, H. Zhu, A.W. Schrader, D. Liang, Q. Ding, P. Joshi, L. Hwang, X.-Y. Zhu, S. Jin, Nanowire Lasers of Formamidinium Lead Halide Perovskites and Their Stabilized Alloys with Improved Stability, Nano Lett. 16 (2016) 1000–1008. https://doi.org/10.1021/acs.nanolett.5b04053.

[32] G. Xing, N. Mathews, S.S. Lim, N. Yantara, X. Liu, D. Sabba, M. Grätzel, S. Mhaisalkar, T.C. Sum, Low-temperature solution-processed wavelength-tunable perovskites for lasing, Nat. Mater. 13 (2014) 476–480. https://doi.org/10.1038/nmat3911.

[33] D. Zhang, S.W. Eaton, Y. Yu, L. Dou, P. Yang, Solution-Phase Synthesis of Cesium Lead Halide Perovskite Nanowires, J. Am. Chem. Soc. 137 (2015) 9230–9233. https://doi.org/10.1021/jacs.5b05404.

[34] H. Huang, F. Zhao, L. Liu, F. Zhang, X.G. Wu, L. Shi, B. Zou, Q. Pei, H. Zhong, Emulsion Synthesis of Size-Tunable CH3NH3PbBr3 Quantum Dots: An Alternative Route toward Efficient Light-Emitting Diodes, ACS Appl. Mater. Interfaces. 7 (2015) 28128–28133. https://doi.org/10.1021/acsami.5b10373.

[35] G. Nedelcu, L. Protesescu, S. Yakunin, M.I. Bodnarchuk, M.J. Grotevent, M. V. Kovalenko, Fast Anion-Exchange in Highly Luminescent Nanocrystals of Cesium Lead Halide Perovskites (CsPbX 3 , X = Cl, Br, I), Nano Lett. 15 (2015) 5635–5640. https://doi.org/10.1021/acs.nanolett.5b02404.

[36] M. Yang, H. Peng, F. Zeng, F. Teng, Z. Qu, D. Yang, Y. Wang, G. Chen, D. Wang,

Journal of Colloid and Interface Science In situ silica coating-directed synthesis of orthorhombic methylammonium lead bromide perovskite quantum dots with high stability, J. Colloid Interface Sci. 509 (2018) 32–38. https://doi.org/10.1016/j.jcis.2017.08.094.

[37] C. Sun, Y. Zhang, C. Ruan, C. Yin, X. Wang, Y. Wang, W.W. Yu, Efficient and Stable White LEDs with Silica-Coated Inorganic Perovskite Quantum Dots, Adv. Mater. 28 (2016) 10088–10094. https://doi.org/10.1002/adma.201603081.

[38] F. Zhang, H. Zhong, C. Chen, X. Wu, X. Hu, H. Huang, Brightly Luminescent and Color- (X = Br , I , Cl) Quantum Dots : Potential Alternatives for Display Technology, 3 (2015) 4533–4542.

[39] H. Perovskite, F.X. Cl, I.C. Nanocrystals, I. Levchuk, A. Osvet, X. Tang, M. Brandl, J. Dar, F. Hoegl, G.J. Matt, R. Hock, M. Batentschuk, C.J. Brabec, Brightly Luminescent and Color-Tunable Formamidinium Lead Halide Perovskite FAPbX 3 (X = Cl, Br, I) Colloidal Nanocrystals, 3 (2017). https://doi.org/10.1021/acs.nanolett.6b04781.

[40] N. Synthesis, N.H. Pbbr, P. Nanoparticles, L.C. Schmidt, A. Pertega, S. Gonza, O. Malinkiewicz, S. Agouram, M. Guillermo, H.J. Bolink, R.E. Galian, J. Pe, Nontemplate Synthesis of CH 3 NH 3 PbBr 3 Perovskite Nanoparticles, (2014) 10–13.

[41] H. Zhong, Colloidal Synthesis of Air-Stable CH 3 NH 3 PbI 3 Quantum Dots by Gaining Chemical Insight into the Solvent E ff ects, (2017). https://doi.org/10.1021/acs.chemmater.7b01100.

[42] L. Peng, A. Tang, C. Yang, F. Teng, Size-controlled synthesis of highly luminescent organometal halide perovskite quantum dots, J. Alloys Compd. 687 (2016) 506–513. https://doi.org/10.1016/j.jallcom.2016.06.162.

[43] H. Wang, N. Sui, X. Bai, Y. Zhang, Q. Rice, F.J. Seo, Q. Zhang, V.L. Colvin, W.W. Yu, Emission Recovery and Stability Enhancement of Inorganic Perovskite Quantum Dots, J. Phys. Chem. Lett. 9 (2018) 4166–4173. https://doi.org/10.1021/acs.jpclett.8b01752.

[44] Q. Li, H. Li, H. Shen, F. Wang, F. Zhao, F. Li, X. Zhang, D. Li, X. Jin, W. Sun, Solid Ligand-Assisted Storage of Air-Stable Formamidinium Lead Halide Quantum Dots via Restraining the Highly Dynamic Surface toward Brightly Luminescent Light-Emitting Diodes, ACS Photonics. 4 (2017) 2504–2512. https://doi.org/10.1021/acsphotonics.7b00743.

[45] P. Liu, W. Chen, W. Wang, B. Xu, D. Wu, J. Hao, W. Cao, F. Fang, Y. Li, Y. Zeng, R. Pan, S. Chen, W. Cao, X.W. Sun, K. Wang, Halide-Rich Synthesized Cesium Lead Bromide Perovskite Nanocrystals for Light-Emitting Diodes with Improved Performance, Chem. Mater. 29 (2017) 5168–5173. https://doi.org/10.1021/acs.chemmater.7b00692.

[46] A. Manuscript, Materials Chemistry A, (2015). https://doi.org/10.1039/C5TA00658A.

[47] J.Y. Kim, V. Adinolfi, B.R. Sutherland, O. Voznyy, S.J. Kwon, T.W. Kim, J. Kim, H. Ihee, K. Kemp, M. Adachi, M. Yuan, I. Kramer, D. Zhitomirsky, S. Hoogland, E.H. Sargent, centrifugal colloidal casting of nanoparticle films, Nat. Commun.

(2015) 1–9. https://doi.org/10.1038/ncomms8772.

[48] D. Bin Kim, J.C. Yu, Y.S. Nam, D.W. Kim, E.D. Jung, S.Y. Lee, S. Lee, J.H. Park, A.-Y. Lee, B.R. Lee, D. Di Nuzzo, R.H. Friend, M.H. Song, Improved performance of perovskite light-emitting diodes using a PEDOT:PSS and MoO 3 composite layer, J. Mater. Chem. C. 4 (2016) 8161–8165. https://doi.org/10.1039/C6TC02099B.

[49] L. Protesescu, S. Yakunin, S. Kumar, J. Ba, N. Masciocchi, A. Guagliardi, M. Grotevent, I. Shorubalko, M.I. Bodnarchuk, C. Shih, M. V Kovalenko, Dismantling the " Red Wall " of Colloidal Perovskites: Highly Luminescent Formamidinium and Formamidinium − Cesium Lead Iodide Nanocrystals, (2017). https://doi.org/10.1021/acsnano.7b00116.

[50] L. Liu, A. Najar, K. Wang, M. Du, S. Liu, Perovskite Quantum Dots in Solar Cells, Adv. Sci. 9 (2022) 1–20. https://doi.org/10.1002/advs.202104577.

[51] J. Xue, J. Lee, Z. Dai, R. Wang, S. Nuryyeva, M.E. Liao, S. Chang, L. Meng, D. Meng, P. Sun, O. Lin, M.S. Goorsky, Y. Yang, Surface Ligand Management for Stable FAPbI3 Perovskite Quantum Dot Solar Cells, Joule. 2 (2018) 1866–1878. https://doi.org/10.1016/j.joule.2018.07.018.

[52] J. Xue, R. Wang, L. Chen, S. Nuryyeva, T. Han, T. Huang, S. Tan, J. Zhu, M. Wang, Z. Wang, C. Zhang, J. Lee, Y. Yang, A Small-Molecule "Charge Driver" enables Perovskite Quantum Dot Solar Cells with Efficiency Approaching 13%, Adv. Mater. 31 (2019) 1900111. https://doi.org/10.1002/adma.201900111.

[53] C. Liu, M. Hu, X. Zhou, J. Wu, L. Zhang, W. Kong, X. Li, X. Zhao, S. Dai, B. Xu, C. Cheng, Ef fi ciency and stability enhancement of perovskite solar cells by

introducing CsPbI 3 quantum dots as an interface engineering layer, NPG Asia Mater. (2018) 552–561. https://doi.org/10.1038/s41427-018-0055-0.

[54] R. Pan, H. Li, J. Wang, X. Jin, Q. Li, Z. Wu, J. Gou, Y. Jiang, Y. Song, High-Responsivity Photodetectors Based on Formamidinium Lead Halide Perovskite Quantum Dot-Graphene Hybrid, Part. Part. Syst. Charact. 35 (2018) 1700304. https://doi.org/10.1002/ppsc.201700304.

[55] J. Zou, M. Li, X. Zhang, W. Zheng, Perovskite quantum dots: Synthesis, applications, prospects, and challenges, (2022). https://doi.org/10.1063/5.0126496.

[56] M. Hasanzadeh Azar, M. Mohammadi, N.T. Rezaei, S. Aynehband, L. Shooshtari, R. Mohammadpour, A. Simchi, Stable Photodetectors Based on Formamidinium Lead Iodide Quantum Well Perovskite Nanoparticles Fabricated with Excess Organic Cations, ACS Appl. Nano Mater. 4 (2021) 7788–7799. https://doi.org/10.1021/acsanm.1c01093.

[57] J. De Roo, M. Ibáñez, P. Geiregat, G. Nedelcu, W. Walravens, J. Maes, J.C. Martins, I. Van Driessche, M. V. Kovalenko, Z. Hens, Highly Dynamic Ligand Binding and Light Absorption Coefficient of Cesium Lead Bromide Perovskite Nanocrystals, ACS Nano. 10 (2016) 2071–2081. https://doi.org/10.1021/acsnano.5b06295.

[58] X. Chen, L. Zhang, S. Chen, Large area CVD growth of graphene, Synth. Met. 210 (2015) 95–108. https://doi.org/10.1016/j.synthmet.2015.07.005.

[59] V. Mursyalaat, V.I. Variani, W.O.S. Arsyad, M.Z. Firihu, The development of program for calculating the band gap energy of semiconductor material based on UV-Vis spectrum using delphi 7.0, J. Phys. Conf. Ser. 2498 (2023) 0–5.

https://doi.org/10.1088/1742-6596/2498/1/012042.

[60] J.H. Simmons, size and semiconductor volume fraction effects on the intensity, line width and position of photoluminescence (PL) peaks from CdTe nanocrystallites have been, 98 (1996).

[61] J. Kim, S. Han, G. Lee, J. Choi, M. Jae Ko, Y. Kim, Single-step-fabricated perovskite quantum dot photovoltaic absorbers enabled by surface ligand manipulation, Chem. Eng. J. 448 (2022) 137672. https://doi.org/10.1016/j.cej.2022.137672.

[62] S. Angizi, P.R. Selvaganapathy, P. Kruse, Graphene-silicon Schottky devices for operation in aqueous environments: Device performance and sensing application, Carbon N. Y. 194 (2022) 140–153. https://doi.org/10.1016/j.carbon.2022.03.052.

[63] B. Zhuang, S. Li, S. Li, J. Yin, Ways to eliminate PMMA residues on graphene — — superclean graphene, Carbon N. Y. 173 (2021) 609–636. https://doi.org/10.1016/j.carbon.2020.11.047.

[64] H. Zhang, Z. Chen, Y. Li, J. Yao, D. Liu, W. Zeng, P. Gui, Z. Huang, A high-performance self-powered photodetector based on a concentric annular α-FAPbI3/MAPbI3 single crystal lateral heterojunction with broadband detectivity, J. Mater. Chem. C. 10 (2022) 11903–11913. https://doi.org/10.1039/d2tc02686d.

[65] A. Dutta, A. Medda, R. Bera, K. Sarkar, S. Sain, P. Kumar, A. Patra, Hybrid Nanostructures of 2D CdSe Nanoplatelets for High-Performance Photodetector Using Charge Transfer Process, ACS Appl. Nano Mater. 3 (2020) 4717–4727. https://doi.org/10.1021/acsanm.0c00728.

[66] Z. Liu, Z. Zhang, X. Zhang, X. Li, Z. Liu, G. Liao, Y. Shen, M. Wang, Achieving

High Responsivity and Detectivity in a Quantum-Dot-in-Perovskite Photodetector, Nano Lett. 23 (2023) 1181–1188. https://doi.org/10.1021/acs.nanolett.2c04144.

[67] C. Zou, Q. Liu, K. Chen, F. Chen, Z. Zhao, Y. Cao, C. Deng, X. Wang, X. Li, S. Zhan, F. Gao, S. Li, A high-performance polarization-sensitive and stable self-powered UV photodetector based on a dendritic crystal lead-free metal-halide CsCu2I3/GaN heterostructure, Mater. Horizons. (2022) 1479–1488. https://doi.org/10.1039/d1mh02073k.

[68] D.H. Kang, S.R. Pae, J. Shim, G. Yoo, J. Jeon, J.W. Leem, J.S. Yu, S. Lee, B. Shin, J.H. Park, An Ultrahigh-Performance Photodetector based on a Perovskite–Transition-Metal-Dichalcogenide Hybrid Structure, Adv. Mater. 28 (2016) 7799–7806. https://doi.org/10.1002/adma.201600992.

[69] S.H. Cheng, T.M. Weng, M.L. Lu, W.C. Tan, J.Y. Chen, Y.F. Chen, All carbon-based photodetectors: An eminent integration of graphite quantum dots and two dimensional graphene, Sci. Rep. 3 (2013). https://doi.org/10.1038/srep02694.

[70] G.W. Flynn, Perspective: The dawning of the age of graphene, J. Chem. Phys. 135 (2011). https://doi.org/10.1063/1.3615063.

[71] A.R. Jang, E.K. Jeon, D. Kang, G. Kim, B.S. Kim, D.J. Kang, H.S. Shin, Reversibly light-modulated Dirac point of graphene functionalized with spiropyran, ACS Nano. 6 (2012) 9207–9213. https://doi.org/10.1021/nn303539y.